Molecular Imaging of Radiation-Induced Lung Injury

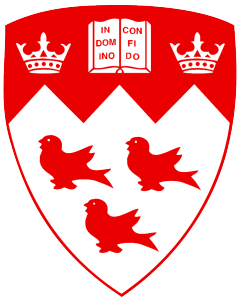

Jessica Rika Perez

Department of Biomedical Engineering
McGill University

A thesis submitted to McGill University in partial fulfillment of the requirements of the degree of
Doctor of Philosophy

 October 2017

I would like to dedicate this thesis to Edith Tueta (Grand-Mami). I miss you.

Acknowledgements

I would like to thank my supervisor Professor Issam El Naqa for giving me the great opportunity to come do my PhD at McGill University. His trust gave me the independence to explore many research directions and allowed me to grow as a researcher and a person.

I would also like to acknowledge Professor Jan Seuntjens for his supervision since Issam left. Jan provided a grounded environment for me to pursue my goals and made possible the completion of my PhD.

I thank my co-supervisor Professor Jay Nadeau for welcoming me in her lab and for supporting me during the definition of my PhD proposal.

I would like to thank Professor Norma Ybarra for the uncountable hours she spent helping me in the lab during my PhD. She provided valuable expertise in biology and lab techniques as well as her continuous participation in lengthy experiments.

During my PhD, I was fortunate enough to develop a strong collaboration with Professor Olivier Lesur from Sherbrooke University. I would like to thank Olivier for providing his clinical expertise and allowing me to become familiar with endomicroscopy in the context of my PhD work. I should also mention Frederic Chagnon, who was so helpful with all the endomicroscopy procedures.

I thank my PhD committee, Issam, Jay, Jan and Professor Peter Siegel as well as Professor Louis Collins for providing ongoing guidance and support throughout all the milestones of my PhD.

I would like to thank my co-authors on one or more papers that I have not mentioned before for their contributions: Dr. Sangkyu Lee, Dr. Ola Maria, Monica Serban, Asha (Krishinima) Jeyaseelan, Li Ming Wang (Tony) and Gabriel Paré.

I would like to acknowledge Dr. Bernier and Mr. Noverraz, who helped contribute to funding the early stages of my PhD through FARO (Foundation for Advancement of Radiation Oncology) and Fondation Juchum.

I would like to thank Margery Knewstubb and Tatjana Nisic from the Medical Physics Unit as well as Pina Sorrini and Daniel Caron from the Biomedical Engineering Department for their administrative support.

I would like to thank Professor Magdalena Bazalova for recommending me to do my PhD at McGill.

I thank all my amazing friends from the McGill Medical Physics Unit for making my Montreal adventure so great and for your support during tough times, in particular: Ali Toltz, Susannah Hickling, Tanner Connell, Joel Mullins, Martin Vallieres, Asha Jeyaseelan, Pete Watson, Yana Zlateva, Marc-Andre Renaud, Kyu Lee, Pavlos Papaconstadopoulos, Piotr Pater, Daniel Markel, James Renaud, Gabriel Famulari, Andre Diamant, Robert Maglieri, Amanda and Ron Dyess.

I would like to thank my Biomedical Engineering friends, particularly Yuhan Ma. I met Yuhan my first week at McGill and we have supported each other on the PhD journey ever since.

Many thanks to my close friend Laura Sasportas Amsallem who gave me valuable advice and constant support throughout my PhD. I could not have done it without her.

I would also like to thank my friends back in Switzerland for keeping in touch despite the long distance and for your ongoing encouragements.

I was lucky enough to meet cousins here in Montreal, Jacky and Claire Perez, thanks for being my family during my time here.

I would like to thank my great-aunt Rina Perez for her positivity as well as my uncle Ellis Tueta, and my cousins Pablo Tueta and Alix Hoffman, and Victor, Fabienne, Laurent and Stephane Mustaki for their support.

Many thanks to my brother Yoel Perez, who was always supportive and reminded me how to stay strong. He is always there for me.

Lastly, my warmest thanks go to my loving parents, Sylvia and Jack Perez for making everything possible and supported my career choices even if it brought me miles away from them. I cannot thank them enough for their support and for always believing in me.

Abstract

Imaging allows the visualization of biological processes at the anatomical, cellular and molecular level inside a living organism. Using a variety of imaging techniques, it is possible to diagnose and monitor disease evolution and response to therapy.

Radiation-induced lung injury (RILI) occurs in up to 30% of thoracic radiation therapy (RT) for lung or breast cancer and remains a major limiting factor to dose escalation and more efficient treatments. The underlying molecular mechanisms of RILI development remain an area of active research and limited treatment options are available to mitigate this debilitating side effect. Stem cell therapy and in particular mesenchymal stem cells (MSCs) have shown promise for potential RILI treatment. However, the use of stem cell therapy has been hindered by our lack of understanding regarding their behavior once administered in the body.

In this thesis, we proposed, developed and validated a pre-clinical imaging platform to image and quantify the evolution of RILI and study MSCs behavior in a rat model of RILI using *in vivo* fluorescence endomicroscopy (FE) imaging and computed tomography (CT). We first demonstrated the feasibility of tracking fluorescently labeled-MSCs in the lung with FE imaging in a rat model of RILI. Next, following successful MSCs tracking, we used longitudinal CT imaging to monitor the evolution of RILI and assess MSCs' potential in mitigating it. Finally, since CT imaging is restricted to anatomical macroscopic imaging, we developed a fibrosis targeted fluorescent probe coupled with FE imaging to detect RILI at the molecular level *in vivo*. In order to relate microscopic FE images to their location in the lung, we used x-ray fluoroscopy guidance to detect the position of the endoscope at the time of imaging and map it back to its corresponding location on the CT image.

The imaging tools developed here provide valuable information into disease state and progression as well as the assessment of new therapies such as MSCs-based stem cell therapy for RILI. The applications of those tools can be expanded to other diseases, cell types or biological processes of interest, paving the way to clinical implementation for improved patient care.

Résumé

L'imagerie permet la visualisation de processus biologiques au niveau anatomique, cellulaire et moléculaire à l'intérieur d'un organisme vivant. En utilisant différentes techniques d'imagerie, il est possible de diagnostiquer et suivre l'évolution d'une maladie et la réponse au traitement.

Les blessures pulmonaires radio-induites (BPRI) se manifestent jusqu'à 30% des radiothérapies (RT) thoraciques pour le cancer du poumon ou du sein et demeurent une limitation majeure à l'escalade de la dose ou d'autres traitements plus efficaces. Les méchanismes moléculaires sous-jacents du développement des BPRI demeurent un domaine de recherche actif et les options de traitements pour atténuer ces effets secondaires débilitants sont limitées. La thérapie par cellules souches et en particulier, les cellules souches mésenchymateuse (CSMs) se sont démontrée prometteuse pour le traitement potentiel des BPRI. Toutefois, l'utilisation de la thérapie par cellules souches a été entravée par notre manque de compréhension en ce qui concerne leur comportement une fois administé dans le corps.

Dans cette thèse, nous avons proposé, développé et validé une plate-forme d'imagerie préclinique pour imager et quantifier l'évolution des BPRI et étudier le comportement des CSMs dans un modèle de rat des BPRI *in vivo* en utilisant l'endomicroscopie à fluorescence (EF) et l'imagerie par tomodensitométrie (TD). Nous avons premièrement démontré la faisabilité du suivi des CSMs marquées par fluorescence dans le poumon avec l'imagerie EF dans un modèle de rat des BPRI. Suite au succès du suivi des CSMs, nous avons utilisé l'imagerie par TD longitudinale pour surveiller l'évolution des BPRI et évaluer le potentiel des CSMs à les atténuer. Enfin, comme l'imagerie par TD est restreinte à l'imagerie macroscopique anatomique, nous avons développé une sonde fluorescent ciblée pour la fibrose couplée à l'imagerie EF pour détecter la FPRI au niveau moléculaire *in vivo*. Afin d'établir un rapport entre les images EF microscopiques et leurs emplacements dans le poumon, nous avons utilisé le guidage par fluoroscopie à rayons-x pour détecter la position de l'endoscope au moment de l'imagerie et de retracer l'emplacement correspondant sur l'image de TD.

Les outils d'imagerie développer ici fournissent des informations de valeurs sur l'état d'une maladie, sa progression ainsi que l'évaluation de nouvelles thérapie comme la thérapie par cellules souches avec CSMs pour traiter les BPRI. Les applications pour ces outils peuvent s'étendre à d'autres maladies, types de cellules ou processus biologiques d'intérêts, ouvrant la voie à une mise en oeuvre clinique pour améliorer les soins aux patients.

Contents

List of Figures

List of Tables

List of Abbreviations

RT	Radiation Therapy
SBRT	Stereotactic Body Radiation Therapy
RILI or RILD	Radiation-Induced Lung Injury or Damage/Disease
RIPF	Radiation-Induced Pulmonary Fibrosis
MSCs	Mesenchymal Stem Cells or Marrow Stromal Cells
SCT	Stem Cell Therapy
CT	Computed Tomography
MRI	Magnetic Resonance Imaging
PET	Positron Emission Tomography
FE	Fluorescence Endomicroscopy
FP-CLE	Fluorescent Probe Confocal Laser Endomicroscopy
IV	Intravascular
ET	Endotracheal
HU	Hounsfield Units

Preface and Contribution of Authors

This thesis consists of three manuscripts, two published (chapter 4 and chapter 5) and one submitted under review (chapter 6). All manuscripts were authored by me, but required the assistance and contribution of various co-authors.

I conceived and carried out all the experiments and wrote the manuscripts. Prof. Norma Ybarra provided assistance in the lab throughout all experiments including cell culture and animal handling for all three articles (chapters 4, 5 and 6). Frederic Chagnon carried out surgical procedures for fluorescence endomicroscopy imaging in chapter 4 and 6. Monica Serban and Dr. Sangkyu Lee showed me and helped me carry out radiotherapy treatment planning and delivery for our rat model in all experiments (chapters 4, 5 and 6) as well as CT imaging in chapter 5. Dr. Ola Maria started the stem cells study and carried out this part of the experiments in chapter 5. Krishinima Jeyaseelan helped with the animal handling in chapter 5. Li Ming Wang contributed to histopathology image analysis in chapter 5. Gabriel Pare helped with the logistics and harvesting lung tissue following imaging in chapter 6. Prof. Olivier Lesur gave us access to his fluorescence endomicroscopy system and carried out the imaging in chapter 4 and 6. Prof. Jan Seuntjens and Prof. Issam El Naqa provided guidance in developing all the experiments and edited the manuscripts. All co-authors reviewed the manuscripts.

Also part of this thesis, I wrote one book chapter (chapter 2) and I am a co-author on another book chapter. Only the section of the book chapter that I wrote is included in this thesis (chapter 3).

Chapter 1

Introduction

1.1 Overview

Among cancer patients receiving radiation therapy (RT), some will develop side effects that can lead to severe complications and limit the use of more aggressive treatment methods. In thoracic irradiations, the concern arises in developing radiation-induced lung injury (RILI). It starts with an inflammatory phase and is followed by a fibrotic phase, both causing patients respiratory distress due to poor lung function. Limited treatment options are available to mitigate those debilitating effects. Stem cell therapy has been proposed for their potential in reducing inflammation, has shown promise in other organs and is under investigation for the lungs. Stem cells' mechanism of action remains poorly understood and a major obstacle to bringing stem cell therapy to the clinic. Medical imaging provides the opportunity to visualize anatomical changes due to diseases non-invasively and longitudinally *in vivo*. With the advent of molecular imaging, it is possible to follow stem cells and monitor their potential beneficial effect at the molecular level. In this thesis, we proposed, developed and validated molecular imaging tools to monitor the onset of RILI, track stem cells, and evaluate their mitigation potential in a pre-clinical setting.

1.2 Background

1.2.1 Radiation Oncology

Cancer is one of the leading cause of mortality worldwide with about 14 million new cases in 2012 and 8.8 million deaths in 2015 (according to the World Health Organization) [1]. Based on the Canadian Cancer Society statistics, it is estimated that 1 in 2 Canadians will develop cancer during their lifetime. The most common cancers are lung, breast, colorectal and prostate cancer, and they account for 50% of all new cancer cases. Lung cancer alone accounts for 14% of new cancer cases in Canada. On average, 565 Canadians will be diagnosed with cancer and 221 Canadians will die from cancer every day [2].

Common cancer treatments include surgery, chemotherapy and radiation therapy (RT), alone or in combination. Surgery allows to resect the tumor or part of the tumor locally. Chemotherapy aims to treat cancer systemically by injection of cytotoxic drugs. RT uses ionizing radiation to damage cancer cells locally, most commonly using external beam radiotherapy, where photons or charged particles are targeted to the tumor volume from outside the patient. In this approach, the ionizing radiation beam (photons or electrons) is produced within a linear accelerator.

When patients are diagnosed and RT treatment is decided, they undergo a computed tomography (CT) simulation scan to identify the size and location of the tumor to be treated. The tumor volume is contoured on the image as well as a safety margin around it to account for microscopic cancer spread. In addition to the tumor, surrounding normal tissue or organs at risk (OAR) are also contoured. Then, a treatment plan is designed based on those contours and the RT prescription. The plans can be very complex with RT beams coming from multiple directions and angles to maximize the dose to the tumor and limit the dose to the surrounding OARs. Dose limits for specific organs have been established and the plan is accepted based on experience from radiation oncologists. When RT is delivered, energy is deposited in the tissue, causing cell kill through direct DNA breaks or indirectly through the formation of free radicals, which themselves create DNA strand breaks. Ionizing radiation and free radicals also affect other cell components such as mitochondria (also containing DNA) or lipids for example. The dose of radiation, in Gray (Gy), is defined as the amount of energy absorbed per unit mass of medium (J/kg). RT prescription dose and delivery schedule vary according to many factors such as type of tumor, stage, location or patient's age and is prescribed by the radiation oncologist.

More than half of all cancer patients receive RT for curative and palliative purposes and it is an essential option for inoperable locally advanced cases. Among these patients undergoing radiation therapy, some will develop side effects, which could seriously impact their quality of

life and lead to complications and even death [3]. The main objective of radiation therapy is to consider a balance between treating the tumor and sparing normal tissue [4]. RT outcomes can be characterized by the tumor control probability (TCP), i.e., how well the tumor is responding to treatment locally, and the risk of complications associated with the surrounding normal tissue: the normal tissue complication probability (NTCP). These probabilities can be represented by two sigmoid curves on a graph where the y-axis is the response probability and the x-axis is the damage metric used [4]. With increased damage to the tissue, the higher the TCP, but also the higher the risk of complications. The space between the TCP and the NTCP curves is called the therapeutic window. Giving higher doses would achieve better tumor control and overall outcomes but it is limited by side effects to surrounding normal tissues, in order to remain in the therapeutic window.

1.2.2 Radiation-Induced Lung Injury

Despite great progress in modern RT delivery methods, normal lung tissue exposure to irradiation can invariably occur during the treatment of variety of cancers such as lung, esophageal, breast, and various childhood malignancies leading to increased risk of radiation-induced lung injury (RILI) or disease/damage (RILD). RILI or RILD is used interchangeably in the following chapters of this thesis. RILD manifests in up to 30% of thoracic irradiations in two phases: an early acute inflammatory phase, which occurs days or weeks following RT, which is referred to as radiation pneumonitis. Following improper healing of the inflammation, a later more permanent chronic fibrotic phase develops with the accumulation of scar tissue and this phase is termed radiation-induced pulmonary fibrosis (RIPF) [5]. By analogy, one can think of a small cut or a scratch on the skin. First, the tissue swells and becomes red as the immune cells are recruited to the site of injury to start the cleaning and repair. This is the inflammatory phase. Following inflammation, the skin starts to heal by forming scar tissue which is composed of extra-cellular matrix components such as collagen. This is the fibrosis phase. The scar tissue at the injury site is never going to be the same as before the injury as the skin then becomes stiff, and missing essential functional elements like pores or hair follicles. The same phenomenon occurs in RILD, causing the lung to stiffen and therefore seriously impacting lung function with reduced gas exchange capabilities and causing dyspnea (difficulty breathing).

RILI is a major limiting factor to treatment success and an obstacle to the application of advanced and promising dose escalation modalities such as stereotactic body radiotherapy (SBRT) to patients at advanced stage disease [6]. Studies using SBRT in inoperable early stage

lung cancer have shown significant improvement in local control and overall survival rates. However, its potential to treat more advanced stages with larger tumor targets is severely limited by RILD. Despite significant efforts to develop different strategies to mitigate RILD, limited success has been achieved for clinical practice. The only available options currently are steroids treatment to reduce inflammation and/or oxygen inhalation. There is an imperative need to develop new strategies to mitigate this debilitating effect [7].

1.2.3 Stem Cell Therapy

Stem cells are undifferentiated cells capable of giving rise to different cell types. Resident stem cells have been identified in the lungs that act to maintain tissue homeostasis (tissue regeneration throughout life) in normal conditions. A common model for tissue regeneration is that stem cells first give rise to progenitor cells, which are committed stem cells able to give rise to a limited number of cell types, which themselves divide (amplification) into specialized functional cells. In the lungs resident progenitor cells have been identified mostly in the context of response to injury, namely clara cells and type II pneumocytes in the bronchiolar and alveolar epithelium, respectively [8].

In the event of organ injury arising from chronic disease or response to insult, if the damage is too great, a significant portion of resident stem cells and progenitor cells are most probably lost and/or are not sufficient for rescuing the injured organ. In recent years stem cell therapy has shown great promise in regenerative medicine. Embryonic stem cells (ESCs) that are capable of giving rise to all cell types in the body are the most obvious choice for organ regeneration but their use remains limited due to availability as they are collected from embryos and to safety concerns as they were shown to create teratomas. In that manner, adult stem cells are more easily available and are of less concern with respect to tumor formation [9]. In particular bone marrow derived stem cells, mesenchymal stem cells or marrow stromal cells (MSCs) have demonstrated great promise in regenerative medicine for multiple organs including the lungs [8]. To define a MSCs, it has to fulfill a minimum of three criteria: (1) MSCs are plastic adherent cells in culture, (2) they express specific markers (CD105, CD73, CD90) and don't express other markers (CD45, CD34, CD14, CD116, CD79, CD19, or HLA-DR surface molecules), and (3) they are able to differentiate into adipocytes, osteocytes and chondrocytes *in vitro* [9].

Upon injury, MSCs are attracted to the site of injury and tend to localize there preferentially. This phenomenon, known as homing, involves the secretion of several factors by the insulted tissue, the sensing of those factors by MSCs, and their subsequent recruitment to the site [9].

Stem cell therapy aims to repair or regenerate damaged organs and it is a potential mitigating strategy that is currently being actively investigated in RILI as well as other related lung diseases such as idiopathic pulmonary fibrosis. Although MSCs therapy showed beneficial effects in the treatment of injured tissue, their mechanism of action is still being investigated. In particular, rather than MSCs engrafting in the tissue and differentiating into lung tissue for repair, it appears now that this may be a fairly rare event and that the beneficial effects of MSCs lie in their paracrine immunomodulatory capacity [10, 11]. Indeed, MSCs can modulate the immune system through inhibition of activation of dendritic cells and T lymphocytes and inflammatory cytokines secretion (TNF-alpha, IFN-gamma) as well as increase release of anti-inflammatory cytokines (IL-10, IL-4) [9]. Clinical trials are currently under way using MSCs for the treatment of inflammatory diseases, including chronic obstructive pulmonary disease (COPD), which relies only on anti-inflammatory properties of MSCs to improve lung function [10]. RILD is also an inflammatory process, with the combination of damage to parenchymal cells as well as vascular endothelium and connective tissue, and including the release of cytokines and growth factors. MSCs immunomodulatory effects could be of interest to mitigate those effects. Stem cell therapy is currently under pre-clinical investigation for the treatment of radiation pneumonitis at the time of injury (inflammation) and later on for fibrosis to regenerate injured tissue [12]. This approach has shown promise for the treatment of radiation induced injury in other organs such as salivary glands [13] and is now pursued for the lungs [14].

Despite great efforts to bring stem cell therapy to the clinic, its use has been hindered by the lack of understanding of their behavior once administered. Questions such as, where do they go following injection or how long do they survive and do they interact with the damaged tissue remain unanswered. Labeling stem cells and tracking them with imaging holds the promise to gain a better understanding of their behavior and can help determining their efficacy and optimizing their use for improved results.

1.2.4 Medical and Molecular Imaging

Medical imaging uses different techniques to visualize the inside of the body for clinical diagnosis and disease monitoring. It can be used to assess the extent of RILI at the anatomical level. The most common imaging method for clinical RILI assessment is a chest x-ray (2-dimensional) or computed tomography (CT) scan (3-dimensional) [15]. It provides information of anatomical changes associated with damaged lung tissue and the development of fibrosis. However, it is limited to macroscopic anatomical imaging and therefore lacks molecular

information on the mechanisms of RILI. Molecular imaging is defined as the visualization and quantification of biological processes at the molecular level in a living organism [16]. It has shown great potential in the recent years and is a field in constant evolution. It involves the use of targeted imaging agents capable of detecting the process of interest *in vivo* and report back for quantification. In the case of RILI, molecular imaging can be used to detect inflammation and the accumulation of scar tissue in the later stages of RIPF. Both anatomical and molecular imaging can serve as end-points and assess the potential of new therapies such as stem cell therapy with MSCs.

Medical imaging is not limited to imaging from outside the body, endoscopy is an optical imaging method that allows the visualization of accessible organs such as the lungs overcoming limitations related to limited light penetration and achieving sufficient contrast and increased resolution compared to external imaging modalities. Bronchoscopy is a valuable tool for the physician as it is directly amenable to patient bedside and provides information on the tissue state of injury itself. Recent developments in endoscopy allows to literally have a microscope at the tip of the endoscope capable of optical biopsies [17]. Furthermore, it is now available with fluorescence microscopy properties both clinically and pre-clinically. Fluorescence is a form of luminescence that occurs when a specific substance (with specific light absorbance and emission properties) absorbs light at a certain excitation wavelength and consequently emits light that is shifted towards longer wavelengths relative to the excitation (facilitating differentiation of the emitted light from that used to produce it). This light emission at a specific emission wavelength can be detected, therefore providing an image of where the fluorescent substance is. The fluorescent substance can be combined to a specific target of interest to image different biological processes. This method is used in fluorescence microscopy and the same is applicable in fluorescence endomicroscopy (FE) imaging, where the microscope is inserted in the tissue of interest. An FE system is composed of a laser scanning unit providing excitation lasers [18]. The excitation light travels through a bundle of optical fibers to the tip of the endoscope in contact with the tissue where the fluorescent target is located. The fluorescent probe absorbs the light and emits it back. The emitted light is collected by the optical fibers, travels back to form an image of the collected fluorescence. FE is a versatile, minimally-invasive imaging tool that is able to both monitor RIPF when used in combination with a collagen-targeted fluorescent imaging probe and track fluorescently labeled cells *in vivo* [19].

1.3 Objectives

The underlying molecular mechanism of RILI and its potential mitigation with MSC therapy remain unknown and an area of active research.

Imaging has evolved greatly in the recent years and is now a valuable tool to answer such open research questions and a platform for translation as many imaging techniques are clinically applicable.

In this work, we aimed to develop a pre-clinical imaging platform to gain a better understanding of the mechanism behind RILI development and to monitor MSCs-based therapy with the following objectives:

1. To develop an imaging method to track MSCs in the lung
2. To establish imaging tools to monitor the evolution of RILI
   (a) To be used as an end-point for MSCs therapy efficacy assessment
   (b) To visualize RILI development at the anatomical and molecular level

1.4 Thesis Outline and Scientific Contributions

This thesis is composed of three manuscripts, two published, and one submitted (under review), a protocol article (accepted), as well as one book chapter (in production) and one section of a book chapter (published).

Chapter 1 introduces radiation therapy in oncology and RT's side effects in radiation-induced lung injury (RILI). It is followed by the potential of stem cell therapy for RILI and describes medical and molecular imaging concepts at the basis of this thesis. This leads to the objectives of the thesis as mentioned above, namely the development of a molecular imaging platform to gain insight into RILI and potential mitigation with stem cell therapy.

Chapters 2 and 3 constitute the detailed background of this thesis on imaging in both RILI and stem cell therapy, respectively. Chapter 2 provides background into RILI development, reviews the use of imaging in RILI currently and highlights new developments in the field. This chapter was submitted as a book chapter. Chapter 3 is a section of a published book chapter [18] that describes new developments in endomicroscopy imaging. This section includes a review of stem cell therapy imaging and highlights the use of fluorescence endomicroscopy (FE) imaging for stem cell tracking in RILI.

Chapter 4 is a published article in Scientific Reports proposing and validating the use of fluorescence endomicroscopy imaging to track stem cells in the lung in a rat model of RILI. [20]. This publication led to a submitted protocol article in Current Protocols in Stem Cell Biology detailing MSCs tracking in the lung with FE imaging as described in Chapter 4 (Appendix A).

Following the successful *in vivo* tracking of MSCs in the lung, the next step was to assess their potential in mitigating RILI. This was assessed with external imaging in Chapter 5, an article published in Scientific Reports [21] comparing two methods: computed tomography (CT) imaging and histopathology to evaluate the extent of RILI over time in a rat model and to assess the potential of MSCs in mitigating it.

CT imaging is restricted to anatomical macroscopic changes in the lung and histopathology lacks temporal and local resolution information. These limitations in the current methods to assess RILI prompted us to develop a fluorescence endomicroscopy molecular imaging method to image RILI at the molecular level. One of the major limitations in FE imaging is the lack of localization of the endoscope probe at the time of imaging. We therefore, implemented image-guided FE imaging to locate the endoscope probe and relate FE images to their corresponding position in the lung on CT images. This is described in Chapter 6, a submitted manuscript developing and validating image-guided fluorescence endomicroscopy for macro- to micro-imaging of RIPF.

Chapter 7 summarizes and concludes the thesis, addresses limitations of the current work and includes clinical prospects, challenges and future research directions.

Chapter 2

Radiation-Induced Lung Injury Imaging: Current status and new developments

Jessica R. Perez

Book Chapter in: *Emerging Developments and Practices in Oncology*

2.1 Preface

This chapter aims to provide background into RILI and RILI imaging. It includes an overview of the molecular mechanisms of RILI onset, describes the current medical imaging methods to assess it and highlights interesting new developments in RILI imaging.

2.2 Abstract

Radiation-induced lung injury (RILI) occurs in up to 30% of thoracic radiotherapy (RT) cases and is a major limiting factor of dose escalation to achieve tumor control and improve survival. RILI can be separated into two phases: an early inflammatory phase and a late fibrotic phase. Imaging has the potential to provide a helpful understanding of RILI for diagnosis, monitoring and treatment. Current clinical imaging methods rely on anatomical imaging and occasionally incorporate functional imaging. With the advent of molecular imaging, specific targeted probes can be designed to image RILI at every stage of the process. Molecular imaging is still in its infancy and most new RILI imaging techniques are still under development. This chapter

summarizes the different imaging methods used clinically for RILI imaging and explores new developments for the future of RILI management.

2.3 Introduction

Lung cancer 5-year survival rates remain very low (15%) and is the leading cause of cancer deaths in the world. During the course of treatment, about 50% of cancer patients will undergo radiation therapy (RT) [7]. RT uses ionizing radiation to kill tumor cells via DNA and cellular damage and treat cancer. RT dose escalation would improve tumor control but is limited by normal tissue toxicity. Like all cancer therapies, radiotherapy involves the risk of developing side effects that could impair the quality of life of patients and lead to severe complications. However, unlike chemotherapy, the side effects of radiotherapy are localized in the organs or tissues that have been irradiated. There is a fine balance, or therapeutic window, between achieving cure or tumor control and reducing adverse effects or toxicities associated with radiotherapy. Radiation-induced lung injury (RILI) occurs in up to 30% of patients who received thoracic irradiation. This primarily includes patients treated for lung cancer, but also includes breast, esophageal cancer or lymphoma patients [7, 5].

The dose delivered to treat the tumor is limited by side effects, acute and late, to surrounding normal tissue. Imaging has the potential to monitor such effects to allow for potential prevention or mitigation strategies in a patient specific manner [15]. Imaging can be used to diagnose patients that are at risk of developing side effects early in the course of treatment when it is still possible to change or adapt treatment or add drugs to mitigate those. Having an imaging tool to detect adverse effects allows for monitoring the response of the patient to mitigating agents or validating newly developed treatment options.

Current clinical practice focuses on anatomical imaging for diagnosis and monitoring of RILI. RILI is a complex process comprising of a myriad of molecular players acting over time to develop functional lung impairments and radiological evidence of disease. Functional lung tests are used to assess the overall lung capacity but lack spatial resolution. Functional imaging techniques can also be used to map lung function for RT avoidance or treatment monitoring. With the advent of molecular imaging and the development of targeted imaging probes, it becomes possible to gain insight into RILI at the molecular level. Most molecular imaging methods for RILI imaging, although promising, are currently being developed and are not yet routinely implemented in the clinic.

This chapter aims to review the current status of RILI imaging and highlight future developments with the potential to improve the diagnosis, monitoring and management of RILI clinically.

2.4 Radiation-Induced Lung Injury (RILI)

Radiation-Induced Lung Injury (RILI) is the damage sustained by normal tissue in the lungs following radiation exposure. The response of normal tissue to irradiation is complex, starting with an inflammatory phase, a proliferative phase and a tissue remodeling phase, each involving a cascade of cytokines and immune cells (Figure 2.1). RILI consists of (1) an early inflammatory phase (reversible) that occurs within weeks of radiotherapy that includes: normal tissue damage, cytokine induction, hypoxia, macrophage accumulation and activation; and (2) a late fibrotic phase (irreversible) appearing months or years following treatment that involves tissue remodeling and fibrosis [7, 22]. The early inflammatory phase is called radiation pneumonitis (RP) and the late phase with scar tissue formation is referred to as fibrosis or radiation-induced lung fibrosis (RILF). The risk factors behind the development of RP are still unclear. It involves a combination of factors such as radiation dosimetric parameters, tumor size and location, concurrent chemotherapy and patient specific factors including age or comorbidities [5]. Limiting RILI risk is a major step towards dose escalation and the application of promising hypofractionated regimens in the lung.

The most common symptom of RILI is dyspnea (difficulty breathing), which can range from mild to severe. Dyspnea is often accompanied with a non-productive cough and rarely fever. Late RILI symptoms can include pulmonary insufficiency that can become chronic [23].

Clinical symptoms associated with RILI are evaluated and graded by the physician following RT. Scoring of RILI can be done using several grading systems that are slightly different. The Radiation Therapy Oncology Group (RTOG) defines a grading system for early and late effects as shown in Table 2.1 [5].

The lungs' response to RT is thought to follow the steps of an abnormal wound healing mechanism: injury, inflammation and repair. Reactive oxygen species (ROS) are produced upon tissue irradiation creating DNA and cellular damage, leading to cell death. Consequently, the epithelial cells lining the lungs (pneumocytes type I and II) undergo apoptosis. Cell depletion induces the secretion of growth factors and the recruitment of inflammatory cells to the injury location. The loss of endothelial cells and small vessels reduces lung perfusion and increases hypoxia. Following the wound healing process, inflammatory cells (leukocytes) are recruited to

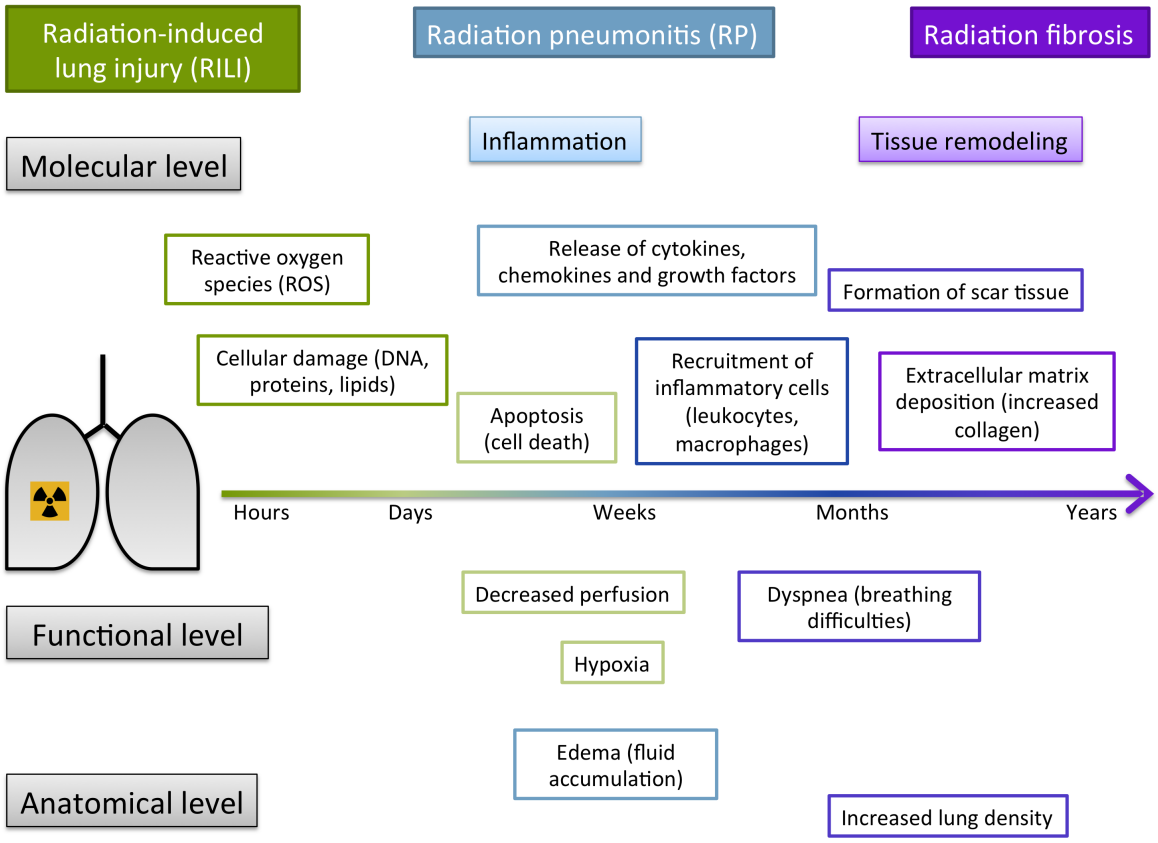

Figure 2.1 **RILI process over time at the molecular, functional and anatomical level.** Upon irradiation, normal lung tissue responds with a cascade of molecular events leading to functional clinical symptoms and anatomical changes. Each step in the RILI process can be a target for imaging.

Table 2.1 RILI scoring schema according to the Radiation Therapy Oncology Group (RTOG) for both early and late effects

RTOG scoring	Acute early effects	Late effects
Grade 1	• Mild symptoms of dry cough or dyspnea on exertion	• Asymptomatic or mild symptoms (dry cough) • Slight radiographic appearances
Grade 2	• Persistent cough requiring narcotic, antitussive agents • Dyspnea with minimal effort but not at rest	• Moderate symptomatic fibrosis or pneumonitis (severe cough) • Low grade fever • Patchy radiographic appearances
Grade 3	• Severe cough unresponsive to narcotic antitussive agent or dyspnea at rest • Clinical radiological evidence of acute pneumonitis • Intermittent oxygen or steroids may be required	• Severe symptomatic fibrosis or pneumonitis • Dense radiographic changes
Grade 4	• Severe respiratory insufficiency • Continuous oxygen or assisted ventilation	• Severe respiratory insufficiency • Continuous oxygen • Assisted ventilation
Grade 5	• Death	• Death

the injury site and secrete chemokines, cytokines and growth factors to recruit and activate more cells (macrophages) to assist in the process. Following RT, this process is not properly regulated and can lead to chronic inflammation, which promotes RILI. The cascade of inflammatory signaling triggers the repair phase with the secretion of interleukin (IL-1 and IL-6), tumor necrosis factor (TNF-α) and transforming growth factor (TGF-β), as well as the recruitment and activation of macrophages. All these factors contribute to tissue remodeling and scarring in the form of fibrosis while perpetuating the inflammatory response leading to chronic RILI [23].

Figure 2.1 illustrates the process of RILI over time at the anatomical, function and molecular levels.

RP is a complex process and studying the cellular inflammatory infiltrate or cell recruitment can be used to understand the process and potentially design targeted probes or therapeutic agents. It was shown that there is a dramatic increase in mast cells (type white blood cells from the immune system known to play a role in allergy) infiltration in the lungs of rats following thoracic irradiation [24]. The predominant cell types recruited in RILI in mice are macrophages and lymphocytes. This acute response is thought to be due primarily to parenchymal cell injury and can therefore sensitize the lungs to a subsequent injury from another exposure like endotoxins [25].

Pulmonary function tests (spirometry) are the gold standard to clinically measure lung function by detecting changes in volumes or flow following inhalation and exhalation. However, they are non-specific, lack spatial resolution and are not sensitive to small lung function changes that can be compensated for by unimpaired lung areas. Imaging can overcome these drawbacks anatomically, functionally or molecularly for diagnosis of lung injury and monitor the potential efficacy of new therapeutic agents. Imaging needs to be validated and benchmarked with proven techniques to demonstrate safety and sensitivity, thereby improving early diagnosis and allowing for a better chance to intervene in the course of treatment. In this way, clinical and pre-clinical imaging can be complementary where one contributes to improving the other [26].

2.5 Imaging Radiation-Induced Lung Injury: Current Status

Current clinical methods to evaluate pulmonary disease include tissue biopsies for histological analysis or bronchoalveolar lavage analysis, both invasive methods and subjective depending on where and when the sample was taken. Lung function tests are non-specific and subtle changes

can go undetected [27]. RILI is most commonly evaluated with anatomical imaging and less so with functional or molecular imaging (Figure 2.2).

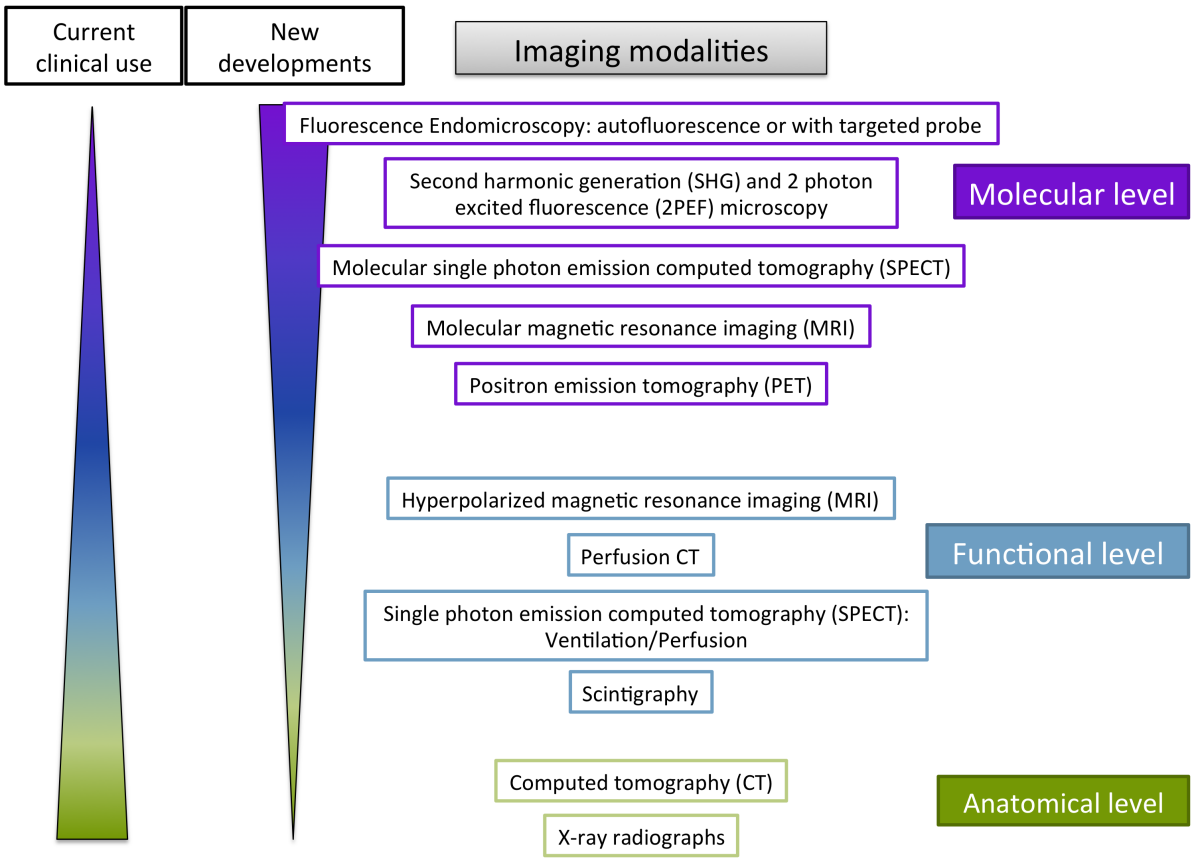

Figure 2.2 **Imaging modalities for RILI imaging from anatomical, functional to molecular level.** The current use in the clinic is inversely proportional with new developments in the field. More established techniques are more anatomical and used more clinically. The more novel the development, the more molecular and the less it is used clinically.

2.5.1 Anatomical Imaging

X-Ray radiographs and Computed tomography (CT)

As mentioned earlier, anatomical imaging remains the principal method to assess RILI clinically. The most common diagnosis tool is X-Ray radiographs (2-dimensional) and its 3-dimensional equivalent, computed tomography (CT). Both methods use X-rays traveling through the body

and attenuation by tissue is measured on the other side with a detector. In the case of CT, the source and detector rotate around the patient to reconstruct a 3D image. X-Ray based imaging relies on the differences in tissue attenuation properties going from high density (bones) to low density (lung). Cell infiltration, edema or fibrosis from RILI will induce an increase in lung density (towards soft tissue density), which becomes visible on CT images. These changes are referred to as radiological evidence of RILI, be it pneumonitis or fibrosis related [15].

Airway remodeling is commonly assessed with CT from which one can extract many features of fibrosis such as reticulation (fine network of lines from architectural distortion), honeycombing ("clustered cystic air spaces" possibly due to small airway dilation) and ground-glass opacity (fibrosis smaller than the CT resolution or active inflammation) [28, 26].

Importantly, increased CT density values in the lungs can be correlated with 3D dose-distribution maps [15].

Pre-clinical models are key to understanding and developing techniques for RILI. With the advent of small animal imaging and RT equipment, it is now possible to compare clinical and pre-clinical results. Monitoring CT changes longitudinally in a partial lung irradiation mouse model showed a dose dependence using the same machine to image and deliver RT [29].

There are key differences in physiology and radiosensitivity when comparing pre-clinical rat models to humans. These need to be taken into consideration for any kind of translational research. The dose commonly given to patients clinically is 60 Gy in 30 fractions and for SBRT: 48 Gy in 3 fractions for peripheral or 50 Gy in 5 fractions for central targets. In the rat model presented in this work, the right lung was irradiated with 18 Gy in 1 fraction on a clinical linear accelerator and the onset of RILI was monitored. This rat model of RILI was used to recapitulate the RILI process to a sufficient extent to image and test mitigating strategies on.

Figure 2.3 ([21], Chapter 5) shows an example of microCT imaging in a rat model of RILI. The affected lung appears denser with opacity on CT and shows a "patchy" pattern (Figure 2.3, right, arrow). The heart and mediastinum shift towards the injured lung is also noticeable (Figure 2.3, right).

Magnetic resonance imaging (MRI)

Magnetic resonance imaging (MRI) can also provide anatomical images of RILI. MRI is a technique based on magnetic fields and radiowaves. MRI signal comes from protons (hydrogen mainly from water present in the body) and therefore provides high soft tissue contrast. However, MRI is not the method of choice for the lungs due to several factors: the lungs have more

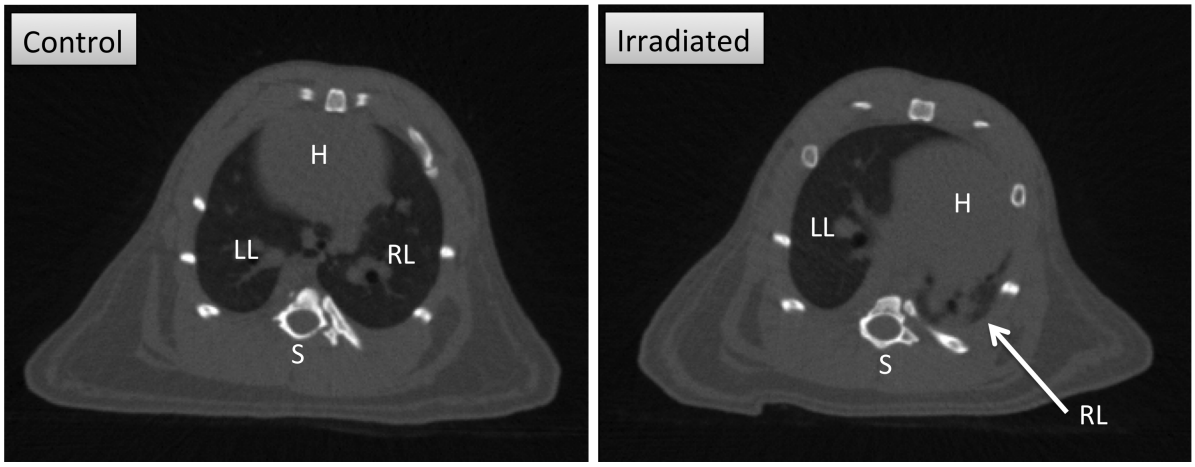

Figure 2.3 **Pre-clinical CT image (transverse plane) of rat model of RILI 24 weeks following 18 Gy irradiation to the right lung.** We observe fibrotic lung tissue in the irradiated lung appearing denser on CT imaging (arrow) compared to the control. Also visible is the shift of the heart and mediastinum towards the injured lung. Left: Control; Right: Irradiated. H: Heart; S: Spine; LL: Left Lung: RL: Right Lung

air space than tissue, leading to a loss of MRI signal, the air-tissue susceptibility artifact and motion artifacts due to breathing are problematic.

Pulmonary inflammation is characterized by the presence of fluid in the lungs (edema). Edema can be visualized using MRI where an increased signal appears. Changes in MRI signal allow for monitoring the effects of anti-inflammatory drugs such as glucocorticosteroids in pre-clinical models [26].

2.5.2 Functional Imaging

Scintigraphy and Single Photon Emission Computed Tomography (SPECT)

A radioactive tracer is administered and localizes to the site of interest. The tracer emits gamma rays that can be detected using gamma cameras (2D planar scintigraphy). By detecting those gamma rays around multiple angles around the patient, a 3D image of tracer localization is reconstructed. Scintigraphy (2-dimensional) and its 3D counterpart SPECT are clinically used to image lung ventilation and perfusion. Radioactive technetium labeled macro-aggregated albumin (Tc99m-MAA) is injected intravenously in the patient. Following the radiolabeled tracer allows monitoring lung perfusion (gas exchange). Ventilation is imaged through the inhalation of radionuclides (Xenon or technetium DTPA), which mimics where air localizes in

the lungs. Defects in ventilation or perfusion can be visualized and localized based on those scans.

Ventilation and perfusion (V/Q ratios) of the lungs can be obtained with ^{133}Xe SPECT and regional defects can be identified. It is one of the most common imaging methods for pulmonary function, although it suffers from poor spatial resolution [26].

SPECT pulmonary function measurement of defects in perfusion is more sensitive than in ventilation, and both are more common than CT density changes [15].

2.5.3 Molecular Imaging

Fluorodeoxyglucose (18-F) Positron Emission Tomography (FDG-PET)

In positron emission tomography (PET) imaging, a molecule of interest is labeled with a radioactive positron-emitter. The probe localizes in the region of interest to be imaged, emits a positron that annihilates with a nearby electron and emits two photons traveling in opposite directions towards a ring detector. It is then possible to reconstruct an image of where the photons came from inside the body and therefore where the radioactive imaging probe was localized. In the case of FDG, the imaging probe is a radiolabelled modified glucose molecule, which gets trapped in cells consuming glucose, and is therefore a marker of metabolism, localizing regions of high glucose intake.

Pulmonary inflammation is difficult to identify from chest X-ray and CT alone as it provides only anatomical information. Molecular imaging has the potential to visualize pulmonary inflammation by targeting inflammatory markers such as FDG-PET for the increased glucose consumption by inflammatory cells or by labeling inflammatory cells themselves [27].

Lung inflammation can be imaged with FDG-PET, where a signal increase is observed due to increased tracer uptake in inflammatory cells, including neutrophils and macrophages [26].

Pulmonary fibrosis can be reproducibly monitored with FDG-PET by evaluating standardized uptake value (SUV) metrics in patients with idiopathic pulmonary fibrosis [30].

FDG-PET allows monitoring pneumonitis following RT. However, those radiological changes do not always correlate with clinical symptoms but show superior sensitivity [15].

2.6 Imaging Radiation-Induced Lung Injury: New Developments

2.6.1 Functional Imaging

Hyperpolarized MRI

In lung injury, gas exchange is impaired due to a thickening of the blood-gas barrier between capillaries, where red blood cells uptake oxygen, and the alveolar space [26].

Hyperpolarized (HP) MRI is a heavily researched area of lung imaging. HP ^{129}Xe can be used with MRI to image gas exchange in the lungs with a single breath hold in healthy volunteers and patients with pulmonary fibrosis. After the subject inhales HP ^{129}Xe, the gas remains mainly in the airspaces but a small fraction of it also dissolves in the lung tissue. ^{129}Xe resonates differently when it is in interstitial tissue or plasma so it is possible to distinguish these two dissolved phases from each other. These two compartments, referred to as the barrier and the RBCs (red blood cells), differ in their chemical shift. With ^{129}Xe behaving like oxygen, it is possible to use it as a probe for studying gas exchange. ^{129}Xe defect maps were compared to CT images of idiopathic pulmonary fibrosis (IPF) patients and show similar regions of fibrosis. It is possible to derive defect maps based on ratios between gas, barrier and RBCs phases. RBCs to gas maps show reduced intensity and defects in gas exchange in IPF patients, whereas healthy volunteers showed homogenous maps [31].

HP ^{3}He-MRI from lung cancer patients were compared before and after RT. Post-RT regions of pneumonitis present on CT images were correlated with areas of reduced ventilation obtained with HP ^{3}He-MRI [32].

Moreover, hyperpolarized MRI was used in RILI rat models to image lung anatomy, function and metabolism. Detected changes in imaging signal due to pneumonitis correlate with histology and could be used to monitor RILI [22]. HP ^{129}Xe MRI combined with gas transfer modeling was also applied to RILI rat models for the detection of early and late effects post-irradiation [33, 34]. Indeed, early gas exchange defects were further detected with HP ^{129}Xe MRI in a rat model of RILI and showed significant differences in pulmonary tissue thickness and relative blood volume measured in irradiated animals compared to controls [35]. In another study, early RILI including inflammation and hypoxia were investigated in a rat model with hyperpolarized ^{13}C MR spectroscopy and imaging. Mapping the lactate to pyruvate ratio signal as a surrogate of metabolic activity demonstrated an increased signal in RILI rats compared to controls [36, 37].

Contrast enhanced perfusion MRI

Contrast enhanced perfusion MRI can be used to visualize early and late effects following RT. Gadolinium-DTPA is injected in the subject and showed altered kinetics with a contrast enhancement in irradiated compared to controls [15].

CT perfusion imaging (CTPI)

CT perfusion imaging (CTPI) measures organ perfusion by injecting an iodine-based contrast agent and monitoring its transport through the organ. This is usually combined with mathematical models to extract parameters of interest. This technique was used to image patients post-RT to detect acute RILI. RILI patients showed changes in blood flow, volume and permeability surface between pre- and post-RT [38].

2.6.2 Molecular Imaging

Molecular MRI

MRI can be used as a molecular imaging modality by tagging a molecule of interest with Gadolinium to become an MR imaging probe. As the imaging probe localizes to the site of interest (in this case the lungs), it is possible to visualize and quantify the accumulation of the probe in a specific location using MRI. For fibrosis being characterized by an overexpression of collagen, molecular MRI was used to specifically detect pulmonary fibrosis in a mouse model using a collagen type I targeted probe [39, 40].

MRI in combination with nanoparticles can provide insight into the development of pulmonary fibrosis. Gadolinium-based nanoparticles were administered intra-tracheally in a mouse model of lung fibrosis and were monitored with MRI. Nanoparticle contrast provided an increased MRI signal in fibrotic areas of the lungs [41].

Molecular scintigraphy and SPECT

SPECT can also become a molecular imaging technique using the idea of imaging probes to target a specific process in RILI.

Collagen accumulation is an important feature of pulmonary fibrosis and therefore a good target for imaging probes. A collagen targeting peptide (collagelin) was synthesized based on the Glycoprotein VI affinity for collagen and labeled with Tc-99m for in vivo scintigraphy in a lung fibrosis mouse model [42].

$\alpha v\beta 6$ integrin overexpression plays an important role in pulmonary fibrosis and is a potential target for drug development as well as imaging. A specific $\alpha v\beta 6$ integrin peptide was labeled with ^{111}In for SPECT-CT imaging in a mouse model of lung fibrosis and was successfully detected in the lungs with an increased signal in injured lungs compared to controls [43].

Two biomarkers for RP imaging were targeted to develop SPECT imaging probes for perfusion (macroaggregated albumin) and for apoptosis (duramycin). Two to three weeks following RT, perfusion volume decreased and duramycin uptake increased, while no changes in breathing rate were observed at this time. This suggests that SPECT imaging with new biomarkers is a good predictor of RP [44].

Molecular SPECT for lung inflammation imaging was developed, in which annexin V (marker of cell stress) or interleukin-8 (binds neutrophils) were radiolabeled [26].

PET

Activation of macrophages plays an important role in the pathogenesis of pulmonary fibrosis. Macrophages were targeted using a cysteine cathepsin probe for both optical pre-clinical and PET imaging in patients showing an increase in signal in fibrosis cases [45].

Fluorescence endomicroscopy (FE)

Lung being an accessible organ, it is amenable to minimally invasive imaging to obtain "optical biopsies" through bronchoscopy. FE or endoscopic confocal fluorescence microscopy is a promising new technique that allows fluorescence optical imaging at the tip of an endoscope. A laser scanning unit coupled to a bundle of optical fibers allows the excitation photons to travel through the endoscope to the tissue and the emitted fluorescence is collected by the same fibers back to give a detailed image of the field of view. It has been used in conjunction with fluorescent probes to observe a variety of cellular and architectural changes in the lungs of normal or injured rat models [46]. Confocal fluorescence endomicroscopy is amenable to clinical use to image the human airways as far as the alveoli, using tissue autofluorescence (elastin at 488nm) as contrast. Structural differences were observed between smokers and non-smokers [17, 47]. Fluorescence endomicroscopy was used to image acute lung injury in a rat model with a fluorescent smart probe activated by an enzyme expressed by neutrophils and macrophages (myeloperoxidase). Enhanced lung enzymatic activity was observed in injured lungs compared to controls [48]. A fluorescent collagen probe was used with fluorescence endomicroscopy to detect pulmonary fibrosis (Figure 2.4, right). FE in combination with

fluoroscopy (X-Ray radiographs) (Figure 2.4, left) and pre-imaging CT allows for image-guided bronchoscopy where it is possible to correlate fibrosis location with FE images of collagen fibers (Perez et al., submitted: Chapter 6).

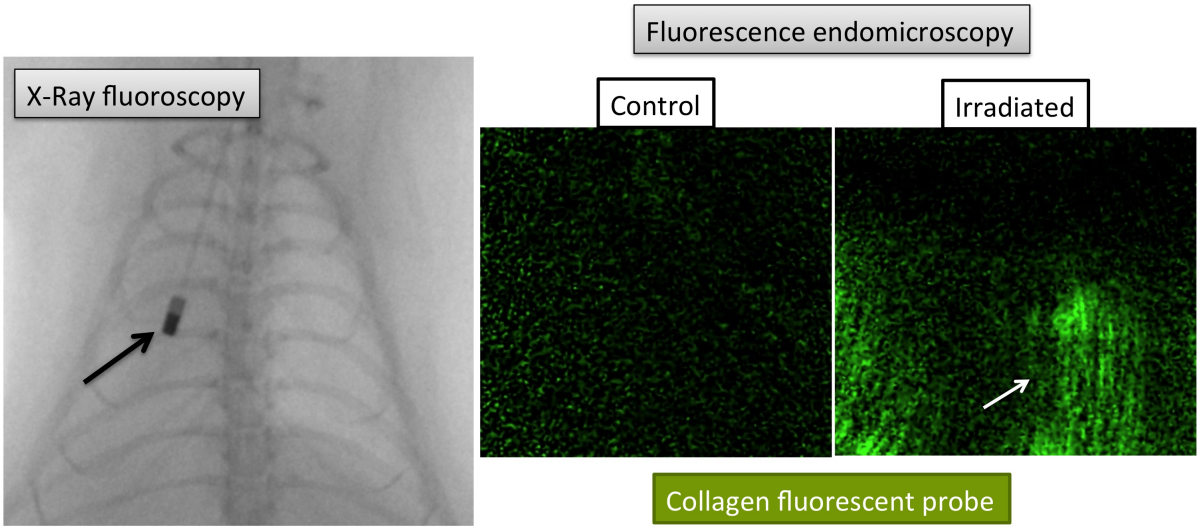

Figure 2.4 **Image-guided Fluorescence endomicroscopy (FE) of RILI.** Left: X-ray fluoroscopy image of RILI rat model showing the location of the tip of the endoscope probe (black arrow). Right: FE images of control and irradiated lung using a fluorescent collagen probe. The white arrow shows collagen fiber structures in the irradiated lung as opposed to random patterns of dotted fluorescence in the control lungs.

Second harmonic generation (SHG) and two photon excited fluorescence (2PEF) microscopy

Second harmonic generation (SHG) microscopy allows for the quantitative analysis of fibrillar collagen structures, a hallmark of fibrosis [49]. Nonlinear optical microscopy combining second-harmonic generation (SGH) and two photon excited fluorescence (2PEF) was integrated in an endoscopic fiber-optic spectrometer for the exploration of the lungs. During fibrosis, the extra-cellular matrix remodels with an accumulation of collagen and elastin, which can be detected by SGH and 2PEF, respectively [50].

2.7 Imaging in the Prevention, Mitigation and Treatment of RILI

Radioprotectors such as free radical scavengers (amifostine, captopril or pentoxifulline) have a protective effect on tissue following RT and can be used to prevent RILI. However, with the results of clinical trials being limited, it is not currently approved for RILI prevention. Once the RILI diagnosis is established, the most common treatment is the use of corticosteroids due to their anti-inflammatory properties. It is unclear if this treatment is beneficial even after cessation. A few other potential RILI therapies are being explored including antioxidants, superoxide dismutase, nitric oxide, TGF-β, statins, matrix metalloproteinases, cytokines and growth factors [23].

2.7.1 Radioprotectors

The potential of amifostine as a radioprotector was tested in a rabbit model of lung SBRT with CT, contrast-enhanced MR angiography (perfusion), ^{3}He MRI (ventilation) and compared to histology. Decreased perfusion was observed with ce-MRA in the irradiated group but not in the irradiated with amifostine, while no changes were observed in ventilation with ^{3}He-MRI [51].

2.7.2 Normal lung avoidance RT planning

Functional imaging information such as ventilation and perfusion acquired with SPECT, PET, MRI or CT can be incorporated into treatment planning. The goal of functional image guided radiotherapy treatment planning is to specifically avoid regions of highly functional lung tissue while increasing the dose to defective regions. Despite many feasibility studies of the use of functional images in treatment planning, the clinical impact has not been proven. Clinical trials are underway to incorporate MR or CT ventilation images for radiation therapy planning. Ventilation defects are less common than perfusion defects and have been shown to be a superior metric for assessing RILI. Importantly, the use of functional imaging techniques has to include accurate image registration in order to be included in treatment planning, including fiducials, reproducible patient positioning, breath hold or gated breathing scans. Thus far, the benefits of using functional image guided planning have not showed significant clinical impact and more work is needed in order to understand the underlying mechanism of RILI imaging and the effect of modifying dose delivery accordingly [52].

By integrating ventilation and perfusion SPECT imaging information with commonly used dosimetric values, it is possible to obtain a superior predictor of RP. This could lead to sparing highly functional lung regions during treatment planning to potentially reduce the risk of RP [53].

Dosimetric parameters were prospectively combined with functional imaging data acquired with 4D-CT, SPECT ventilation and perfusion or both to evaluate RP. RP correlated with dosimetric parameters and functional imaging, especially when combined [54].

2.7.3 Mesenchymal stem cells (MSCs)

Mesenchymal stem cells (MSCs) have been proposed in the treatment of lung injury (inflammation and fibrosis) for their immune-modulatory properties and their paracrine anti-inflammatory potential [55]. Fluorescence endomicroscopy (FE) in a rat model of RILI was used to track MSCs *in vivo*. 3 weeks following RT, rats were injected with fluorescently labeled MSCs intravenously or endotracheally and were imaged with FE. MSCs were visible in the lungs although more numerous when injected directly in the trachea. An automated cell counting algorithm allowed for the quantification of MSCs in controls and RILI showing a slight increase in detected cells in the injured lung (Chapter 4) [20].

2.8 Future Research Directions

The emerging trend in RILI imaging and imaging in general is moving towards molecular imaging. Rather than looking at anatomical changes that take time to develop before becoming visible on anatomical images, it is now possible to image molecular targets at every stage of disease progression. Molecular and functional imaging give a better understanding of RILI and might provide useful diagnostic information early on in order to readapt RT treatment or give mitigating agents before permanent fibrosis damage occurs. These new molecular imaging techniques, although promising, require benchmarking and validation before they can be approved for clinical use. Indeed, the process from bench to bedside takes time for newly developed imaging probes and imaging devices. The power of molecular imaging with *in vivo* visualization of molecular processes is contributing to the assessment of new therapeutic strategies for RILI. Future research for RILI imaging will be in designing and validating new targeted imaging probes, and using these techniques to assess the potential of RILI treatments.

Ultimately, the goal is to make RT more efficient with less toxicity in order to achieve better tumor control for cancer patients.

2.9 Conclusion

This chapter described the molecular steps involved in RILI following thoracic irradiation as well as provided an overview of the imaging techniques used clinically and in development stage for RILI management.

RILI is a complex process composed of multiple stages of molecular events leading to pneumonitis and fibrosis. Each molecular player in the process can be used as an imaging target. Imaging of RILI is evolving from purely anatomical (CT) to functional (SPECT, MRI) and molecular (PET, SPECT, MRI, optical). Molecular imaging has the potential to contribute to RILI diagnosis, monitoring and mitigation. However, more research both clinically and pre-clinically is required in order to bring new imaging techniques from bench to bedside.

2.10 Key Terms and Definitions

- **Contrast Agent:** Substance used to enhance contrast in medical imaging.
- **Cytokine:** A signaling protein secreted by immune cells that has an effect on other cells.
- **Fibrosis:** The scarring process following tissue injury. Tissue remodeling takes place with the deposition of extracellular matrix (collagen).
- **Growth Factor:** A substance that promotes cell growth and proliferation.
- **Imaging probe:** Substance that detects and allows the visualization of a biological process. A specific target that binds or detects the process of interest is coupled to a labeling element that can be detected with imaging.
- **Inflammation:** Process by which the body defends itself from injury or infection. It involves the recruitment of cells from the immune system and the release of cytokines.
- **Lung Perfusion/Ventilation:** Perfusion is the blood in capillaries that attain the alveoli for gas exchange. Ventilation is the air that attains the alveoli for gas exchange.

- **Medical Imaging:** Techniques used to visualize the inside of the body for clinical diagnosis.
- **Molecular Imaging:** Visualization and quantification of biological processes at the molecular level in a living organism.
- **Radiation Therapy Treatment Planning:** Following cancer diagnosis, a CT scan is acquired and the tumor as well as organs at risk are contoured on the image. Based on the contours, the radiation beams are chosen and optimized to maximize dose to the tumor while minimizing the dose to the surrounding normal tissue. The dose is calculated and the best plan is chosen to be delivered to the patient.

Chapter 3

Confocal Laser Endomicroscopy for Stem Cell Therapy Imaging: Application in Radiation-Induced Lung Damage

Jessica R. Perez and Issam El Naqa

Section of book chapter: *Emerging applications of intra-vital smart micro-imaging: from bench-to-bedside* [18]

Gabriel Paré, Réjean Lebel, **Jessica R. Perez**, Frédéric Chagnon, Marc-André Bonin, Catherine Bibeau, Issam El Naqa, Eric Marsault, Martin Lepage and Olivier Lesur

Book Chapter published in: *Microscopy and imaging science: practical approaches to applied research and education*

3.1 Preface

The objective of this chapter was to provide background into stem cell therapy imaging in general and then to introduce the use of endomicroscopy and its application in tracking stem cells in the lung of a rat model of RILI.

3.2 Abstract

Stem cell therapy application has been hindered by the lack of understanding regarding the fate of inoculated cells, and the mechanisms by which they heal targeted tissues. Mesenchymal stem cells (MSCs) are proposed for their immune-modulatory properties and their potential ability to mitigate radiation-induced lung damage (RILD), a side effect of lung cancer radiotherapy. Fluorescent probe confocal laser endomicroscopy (FP-CLE) tracking and quantification of DID-labeled MSCs *in vivo* in a rat model of RILD is shown to be achievable. This method can be complemented using other cell labeling methods or by combining MSCs monitoring with FP-CLE imaging of the pathology to assess the potential of stem cells in treating damaged organs.

3.3 Stem Cell Therapy Imaging

Stem cell therapy (SCT) aims to repair or regenerate damaged organs by one or several mechanisms. This includes differentiating into functional cells and replacing damaged ones, secreting growth factors in a paracrine fashion to stimulate resident stem cells to repopulate the damaged region, or by reducing further damage such as chronic inflammation through immune-modulation. Despite great progress in SCT research, its clinical use remains limited [56]. Stem cells fate and interactions with host cells remain areas of intense research. Molecular imaging and cell tracking methodologies can shed light on these aspects, and can also contribute to identifying roadblocks in the way of successful and safe SCT or to compare and optimize different methods to achieve the desired goals, such as engraftment optimization or survival [56].

A stem cell labelling method must be selected based on the hypothesis or objective, which guides criteria such as cell detection sensitivity, resolution, monitoring period and cost-effectiveness [57]. Labelling can be achieved in a direct or indirect way: with a fluorescent dye, for example, that passively enters the cell or with a reporter gene system where the signal is turned on when the gene is activated, respectively. The former is simpler to use and readily available but is unspecific. Direct labelling does not differentiate between labelled cells and released labelling agents (e.g., after the death of labelled stem cells) that are internalized by other cells. The latter is more challenging to implement but has the potential to answer more complex questions, such as the status of cell viability [58]. Cells can be labelled directly with superparamagnetic iron oxide nanoparticles (SPIONs) and be followed with magnetic resonance

imaging (MRI) or with a positron emitting radionuclide and followed by positron emission tomography (PET) [59]. PET can also be used with reporter gene systems (indirect labelling) to detect, track and quantify stem cell transplantation [60]. MRI-compatible reporter genes can be used as well to monitor and track cells with high resolution *in vivo* [61]. Optical methods like whole-body bioluminescence imaging (BLI) is used pre-clinically to track cells in mice models by gene fusion approaches. BLI has been shown to be semi-quantitative and very sensitive to monitor cell survival and to measure gene expression *in vivo* [62]. With multimodality imaging labels, one can also track cells with two or more imaging methods simultaneously to gain further insights into the stem cell behaviour.

In FP-CLE, labelling can be achieved using a fluorescent dye that passively enters/labels the cell or with a reporter gene system using a fluorescent protein. Intra-vital micro-imaging allows to visualize single cells *in vivo* at cellular resolution [63, 64]. Several applications have already been reported in the literature, including studying stem cells niches [65], homing and engraftment [66, 67], and determining the safety of administering stem cells at varying concentrations [68]. CLE was used to follow transplanted stem cells as a potential treatment for irritable bowel syndrome [69]. In the following section, we discuss the monitoring of mesenchymal stem cells (MSCs) in a SCT rat model of radiation-induced lung damage (Chapter 4) [20].

3.4 Radiation-Induced Lung Damage Mitigation by Mesenchymal Stem Cells (MSCs) Therapy

In the scope of lung cancer treatment by radiation therapy (RT), radiation-induced lung damage (RILD) to healthy surrounding tissues is a limiting factor for dose escalation, and occurs in 30% of patients. RILD limits RT by reducing the total dose that can be delivered – which then can be too low to destroy all cancer cells (small/no therapeutic window) [4, 5]. RILD involves two main phases: an early inflammatory phase (pneumonitis) and a late fibrotic phase (fibrosis) that can be life threatening [23].

MSCs are an alternative treatment option which is currently explored. MSCs are adult stem cells derived from the bone marrow. They can differentiate to give rise to bone, cartilage and muscle tissue [11]. They have been shown to promote organ repair in a variety of organs including the lung [8]. Their mechanism of action is still being investigated but it was reported

that their main role in repair relies on paracrine immunomodulatory effects rather than engrafting and differentiating in functional tissue [11].

3.5 FP-CLE Imaging of MSCs Therapy in RILD

To assess the potential of MSCs in mitigating RILD, we established a rat model of the disease following lung irradiation in a clinically relevant fashion, involving CT simulation, organ contouring, treatment planning, and radiation delivery with a clinical linear accelerator.

3.6 Material and Methods

3.6.1 Rat RILD model preparation and SCT

Sprague-Dawley female rats were anesthetized (isoflurane) and imaged in a CT simulation scanner (Philips Brillance Big Bore, 120 kVp, 175 mA). Using this acquisition, RT was planned to mitigate surrounding organ dose while delivering a 18 Gy dose to the right lung with a 6 MV photon beam. Two or three weeks later, MSC were injected in the animals, and pCLE imaging was performed through a tracheotomy as described before – but in this experiment, animals underwent a CT scan prior to pCLE, and the latter procedure was performed under fluoroscopic guidance (Philips Pulsera).

3.6.2 MSC culture, labeling and injection

MSCs were harvested from the femur bone marrow and cultured as previously described [70]. DiD (Vybrant DiD Cell-Labeling Solution, Thermo Fisher Scientific) was added to MSC at a concentration of 10 μM for 30 minutes in normal culture conditions, and then washed twice with sterile DPBS, and fresh culture media was then added. The next day, MSC labeling was confirmed with fluorescence microscopy. MSC were then harvested, suspended in 1 ml PBS, and injected intravenously (1 million cells).

3.6.3 pCLE procedure and collagen imaging

The animals were prepared for pCLE as described above, and a PE50 catheter was inserted in the right jugular vein. To highlight collagen structures in the fibrotic lung, a collagen-binding

probe derived from the structure of conjugate EP-3533P [39] tagged with a single fluorescein moiety was i-v injected in the jugular vein 15 min before imaging at 10 $\mu mole/kg$ in 1 ml of saline.

3.7 Results and Discussion

The pre-scan CT confirmed RILD in the irradiated right lung (blue outline) as shown in Figure 3.1A. Increased CT signal in this lung was attributable to inflammation, edema and fibrosis. Using fluoroscopy, the distal tip of the S1500 probe and its airway positioning within the affected region is shown in Figure 3.1B. Fluorescent-enhanced collagen microfibrils can be detected in selected areas (ROI) using pCLE in Figure 3.1C, and the presence of MSCs in a similar area is displayed in Figure 3.1D. This work is presented in chapter 4 [20].

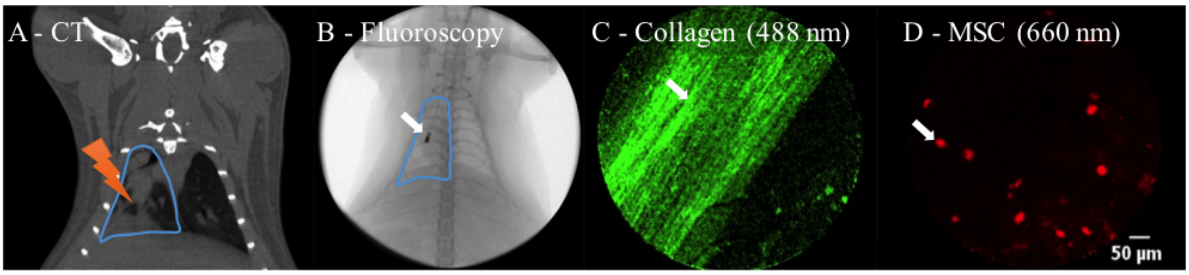

Figure 3.1 **Multimodality imaging of RILD in rats.** (A) CT-scan recorded a few days prior to the pCLE procedure. pCLE was performed under fluoroscopic guidance (B). Images from both lungs were recorded here, pCLE images acquired in an irradiated lung are shown. A collagen targeted probe highlights linear collagen structures related to fibrosis in the green channel (C), while DiD-labelled MSC are tracked in the red channel (D).

Chapter 4

Tracking of Mesenchymal Stem Cells with Fluorescence Endomicroscopy Imaging in Radiotherapy-Induced Lung Injury

Jessica R. Perez, Norma Ybarra, Frederic Chagnon, Monica Serban, Sangkyu Lee, Jan Seuntjens, Olivier Lesur and Issam El Naqa

Article published in: *Scientific Reports* [20]

4.1 Preface

The first step in assessing the potential use of MSCs in RILI mitigation is to be able to follow them once administered in the body. The purpose of this chapter was to establish an imaging method to track stem cells in the lung. This proof of principle allows the visualization of fluorescently labeled MSCs in a rat model of RILI with fluorescence endomicroscopy (FE) imaging. In this article we were able to detect and quantify the presence of MSCs *in vivo*.

4.2 Abstract

Mesenchymal stem cells (MSCs) have potential for reducing inflammation and promoting organ repair. However, limitations in available techniques to track them and assess this potential for lung repair have hindered their applicability. In this work, we proposed, implemented and

evaluated the use of fluorescence endomicroscopy as a novel imaging tool to track MSCs *in vivo*. MSCs were fluorescently labeled and injected into a rat model of radiation-induced lung injury via endotracheal (ET) or intravascular (IV) administration. Our results show that MSCs were visible in the lungs with fluorescence endomicroscopy. Moreover, we developed an automatic cell counting algorithm to quantify the number of detected cells in each condition. We observed a significantly higher number of detected cells in ET injection compared to IV and a slight increase in the mean number of detected cells in irradiated lungs compared to control, although the latter did not reach statistical significance. Fluorescence endomicroscopy imaging is a powerful new minimally invasive and translatable tool that can be used to track and quantify MSCs in the lungs and help assess their potential in organ repair.

4.3 Introduction

Stem cell therapy has been proposed for many years to repair damaged organs. However, little clinical success has been achieved with a few exceptions, and stem cell therapy remains at the research stage. One of the hindering reasons is due to our lack of knowledge and understanding of the biological location and the mechanisms of action of stem cells after being injected.

Bone marrow derived stem cells, mesenchymal stem cells or marrow stromal cells (MSCs) have demonstrated great promise in regenerative medicine for multiple organs including the lungs [8]. Although MSCs therapy showed beneficial effects in the treatment of injured tissue, their mechanisms of action are still being investigated. In particular, rather than MSCs engrafting in the tissue and differentiating into lung tissue for repair, it appears now that this may be a fairly rare event and that the main beneficial effects of MSCs may lie in their paracrine immunomodulatory capacity [10, 11]. Clinical trials are underway using MSCs for the treatment of inflammatory diseases, including chronic obstructive pulmonary disease (COPD), which relies only on anti-inflammatory properties of MSCs to improve lung function [10].

Radiotherapy is used routinely as part of cancer treatment. Among patients undergoing radiation therapy, some will develop side effects, which could seriously impact their quality of life and lead to complications and even death [3]. The therapeutic window between delivering high enough dose to the cancer while still sparing normal tissue is critical in radiation oncology [4]. Radiation-induced lung injury (RILI) occurs in about 30% of thoracic irradiations and is one of the major limiting factors for increasing the dose to achieve better tumor control [5]. RILI is an inflammatory process, with the combination of damage to parenchymal cells as well as vascular endothelium and connective tissue, and including the release of cytokines and growth

factors [3]. Currently, limited therapeutic options are available so MSCs immunomodulatory effects could potentially offer an alternative to mitigate those effects.

Assessing the potential of MSCs for tissue regeneration suffers from limitations in available techniques to follow the cells [64]. This is currently done by *in vitro* methods such as immunohistochemistry (IHC) and real-time polymerase chain reaction (RT-PCR). Those techniques, although very informative require the sample to be either fixed for IHC or destroyed for RT-PCR. A non-invasive method that would be able to track the cells *in vivo* continuously would hence be of great interest to investigate the regenerative potential of MSCs mediated tissue repair and to better understand the underlying dynamics of the process [71].

With the advent of molecular imaging, a number of questions with previously unknown answers can now be addressed [56]. Whole body imaging techniques have been proposed to track delivered stem cells in an injury model, including positron emission tomography (PET), Magnetic resonance imaging (MRI) and optical imaging methods. PET gives 3D imaging and is highly sensitive, however it requires the use of a radioactive tracer and suffers from poor resolution. MRI gives high 3D resolution and great tissue contrast but is still an expensive and complicated method. Bioluminescence imaging is specific and simple but does not have 3D capabilities and is limited to surface imaging in preclinical models [56]. Fluorescence endomicroscopy is minimally-invasive and has the ability to image accessible organs such as the lungs at the cellular level and in real time [17]. This new technology is also amenable to fluorescence endomicroscopy and has been used to detect real-time cellular enzymatic activity (e.g. myeloperoxidase) [48] or to follow fluorescently labeled cells *in vivo* [19]. MSCs have been imaged with endomicroscopy in a preclinical model of inflammatory bowel syndrome [69].

In this work, we investigate the possibilities of using endomicroscopy in conjunction with fluorescently labeled MSCs to assess their behavior in lung a radiation-induced lung injury model. Endomicroscopy is a promising technique that is currently used clinically and therefore opens new doors in terms of the translational potential of this investigation.

The study presents a multidisciplinary effort that combines: (1) The establishment of a rat model for imaging radiation lung injury that includes, to the best of our knowledge, first time investigation of endomicroscopy imaging techniques to assess such model. Our developed rat model mimics treatment planning and delivery procedures of radiation therapy that are consistent with current clinical practice to simplify its potential translation; (2) Application of MSCs therapy as an agent to mitigate radiation induced lung damage. This involves extraction of MSCs, culturing and optimization of cell labeling for real-time tracking purposes; (3) The

optimization of an endomicroscopy imaging protocols for our application in MSCs tracking, which involved several pilot studies to ensure feasibility and efficacy (control vs injured rats, MSCs injection protocol both endotracheal and intravascular, and cell visualization); (4) The design, validation and application of quantitative image processing algorithms to customize automated cell counting from *in vivo* endomicroscopy video aquisitions for comparing different injection routes and imaging conditions.

4.4 Results

4.4.1 *In vivo* imaging of MSCs

In order to assess fluorescence endomicroscopy as an imaging tool for detection of MSCs, we labeled them in culture with membrane dye DiD prior to injection. We chose DiD for its ease of use and its low cell toxicity. Light tissue penetration and autofluorescence are indeed a recurring issue in optical imaging. In our case, we are interested in "surface" imaging of the lining epithelial tissue of the lungs and tracking MSCs fate in a lung injury model with endomicroscopy. Thus, the premise of this work, does not require deep tissue penetration. However, we are also limited by the available lasers and filters technologies in the microendoscope, which contains two channels: green (488 nm) and red (660 nm). Therefore, we chose DiD to match the red channel available since NIR dyes are not per se supported on such a microendoscope system, as applications are limited to surface imaging. On the other hand, 660 nm is not so far to the bottom line level of NIR channel (ie 700 nm). We also chose the red rather than the green to limit excess autofluorescence which is more prominent in the green region of the light spectrum.

To evaluate the impact of radiotherapy and the different routes of MSCs administration with imaging, rats were divided into 4 groups (n = 5 per group): control with intravascular injection of MSCs (Ctrl MSC-IV), control with endotracheal injection of MSCs (Ctrl MSC-ET), irradiated with intravascular injection of MSCs (RT MSC-IV) and irradiated with endotracheal injection of MSCs (RT MSC-ET). MSCs administration and endomicroscopy imaging were conducted 3 weeks post-radiation therapy to follow the distribution of labeled-MSCs.

We were able to detect injected MSCs for both delivery routes, and in radiation damaged lungs. A sample video of MSCs injected ET in an irradiated rat model imaged with fluorescence endomicroscopy is available in supplementary material [20]. Figure 4.1 shows representative *in vivo* fluorescence endomicroscopy images for endotracheal and intravascular injection of MSCs in control and irradiated lungs. Labeled MSCs appear as bright spots on the images. Control

images without any labeled cells injected were also acquired and appear as background noise of gray levels. Qualitatively, there appear to be more MSCs in the ET group compared to IV.

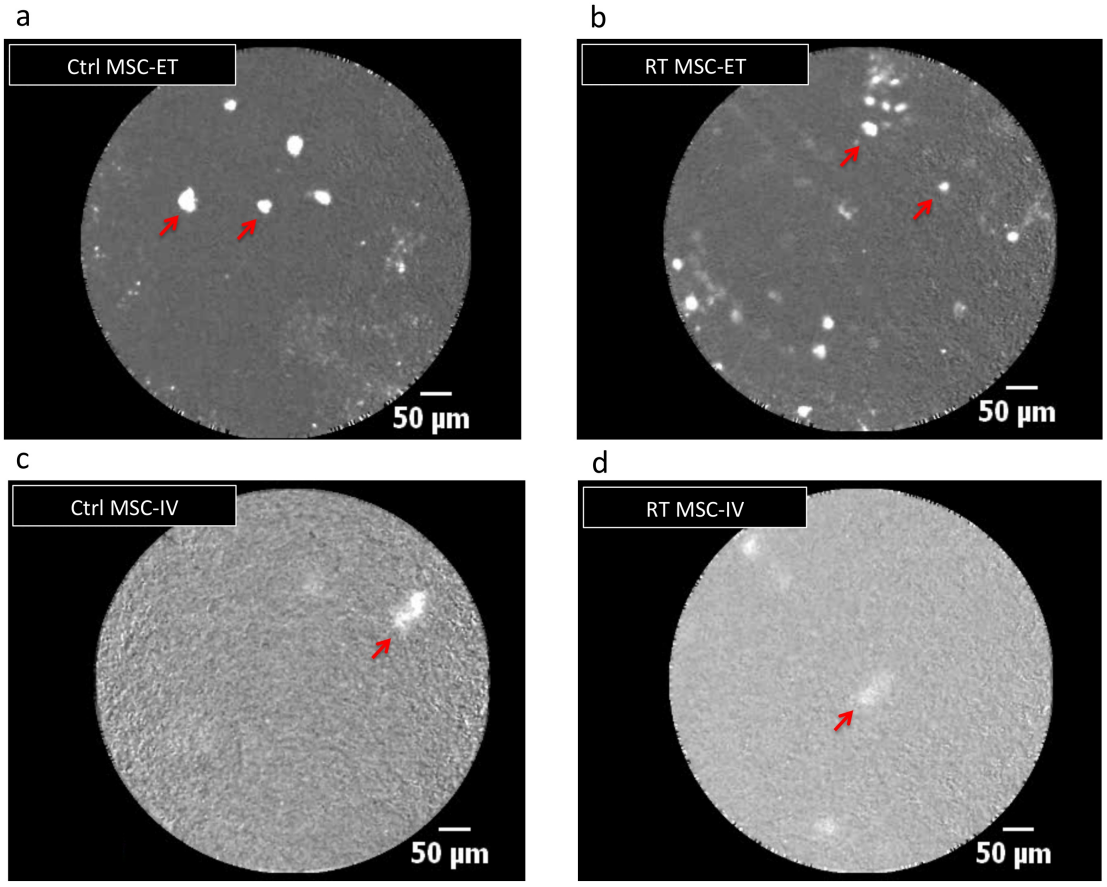

Figure 4.1 **In vivo fluorescence endomicroscopy imaging of labeled MSCs in the lungs for each injection route and condition.** Representative images from video sequences. MSC appear as bright spots (examples of cells shown by red arrows). (a) Ctrl-MSC ET. (b) RT-MSC ET. (c) Ctrl-MSC IV. (d) RT-MSC IV. Cells appear brighter and more numerous in ET injection (top row) compared to IV (bottom row). More cells are observed in irradiated lungs (right) compared to controls (left).

4.4.2 Image analysis and quantification

In order to quantify the visual differences between conditions, we developed an automatic cell counting algorithm in Matlab. Each frame of the acquired video is treated as a stand alone

image and objects (MSCs) are counted on each frame using a granulometry approach. Figure 4.2 describes the different steps of the automated cell counting algorithm.

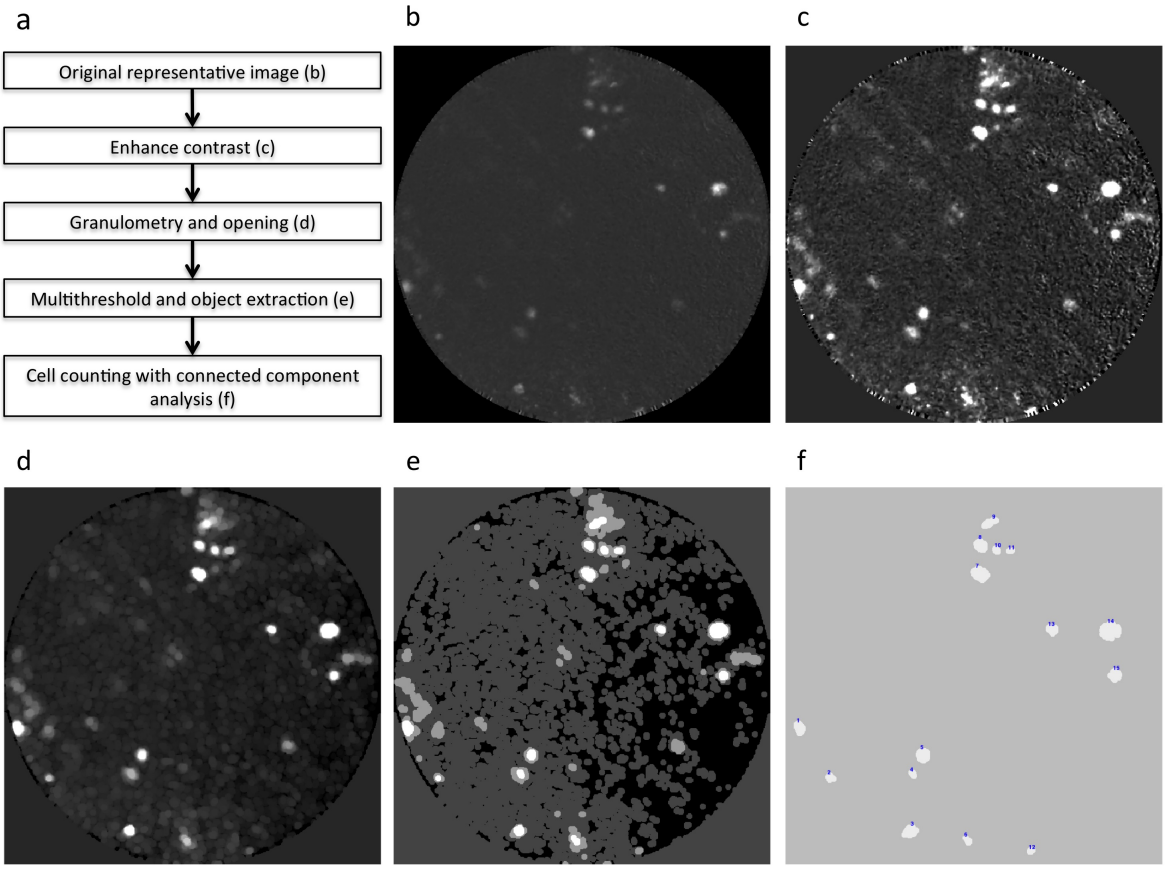

Figure 4.2 **Automatic cell counting algorithm for image quantification.** Each frame in the video sequence is treated as a stand alone image. (a) Summary of workflow. (b) Original representative image. (c) First contrast is enhanced followed by granulometry (d) to determine objects size and image opening. (e) Then, a threshold is applied to highlight bright cells. (f) Finally, cells are counted with connected component analysis.

Cell counting algorithm validation

The developed cell counting algorithm was validated on 400 random video frames (200 for ET and 200 for IV, including control and RT). MSCs were counted on each random frame both visually (ground truth, average of 2 independent observers) and automatically (Figure 4.3). We obtained a concordance correlation coefficient (CCC) of 0.91 (1 being perfect agreement) for

ET and a CCC = 0.73 for IV. To assess inter-observer variability we compared cell counts from two independent observers and obtained a CCC = 0.85 for ET and CCC = 0.81 for IV.

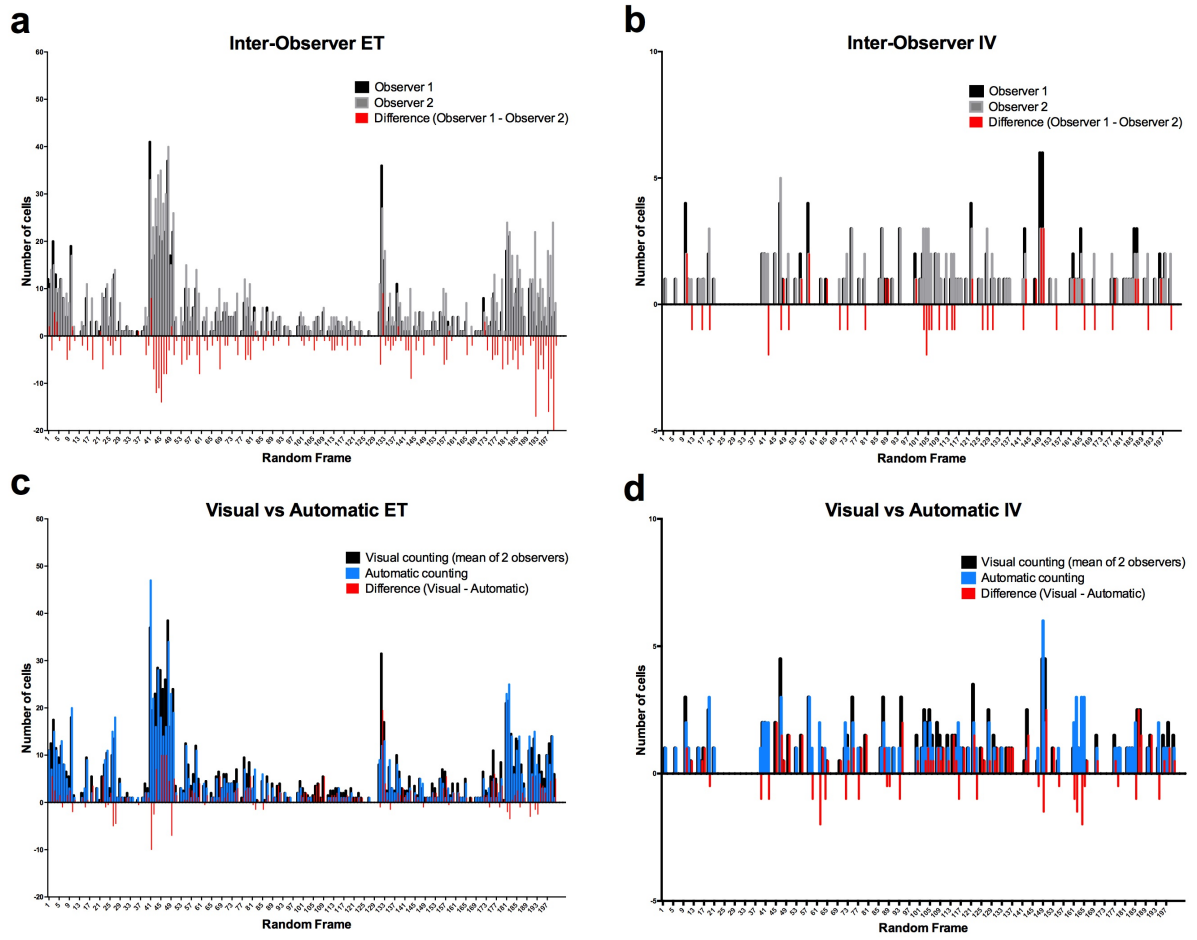

Figure 4.3 **Automatic cell counting algorithm validation.** Graph represents number of counted cells for each random frame comparing inter-observer variability and visual vs automatic counting with residual differences. (a) Inter-observer variability ET. (b) Inter-observer variability IV. (c) Visual vs Automatic ET. (d) Visual vs Automatic IV.

Cell Counting in Video Sequence

Once the automatic cell counting algorithm was validated, we applied it to full video sequences. As the endoscope probe moves through the lungs acquiring images, we compute the number of detected cells per frame in each video sequence (Figure 4.4). The number of detected cells varies depending on the region being imaged and motion, including breathing and heartbeat.

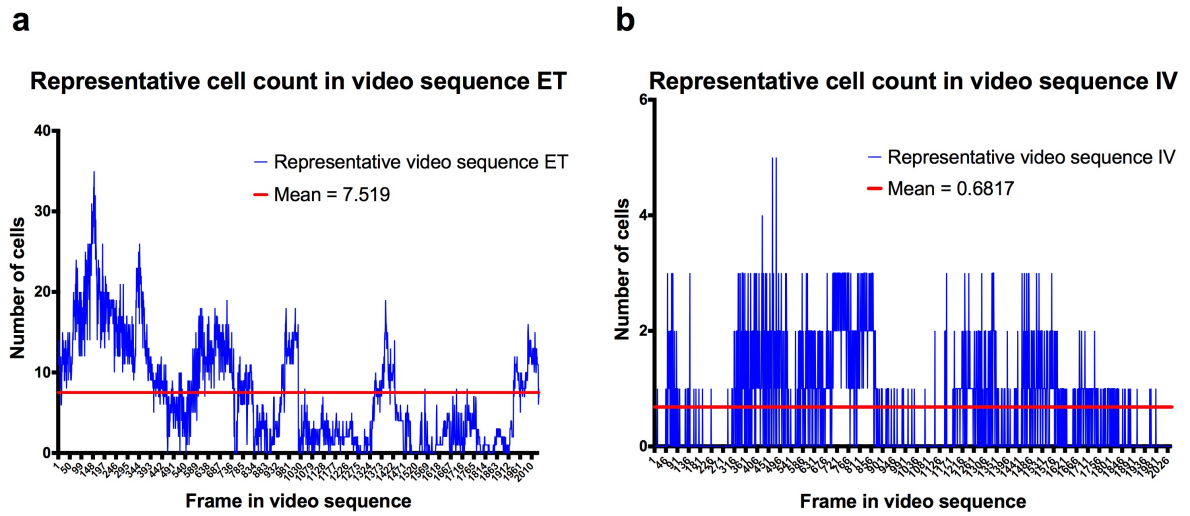

Figure 4.4 **Number of detected cells per video frame in a representative video sequence.** Representative cell count per frame using the automatic cell counting algorithm for ET (a) and IV (b). As the microendoscope probe moves in the lungs acquiring images, the number of detected cells varies.

4.4.3 MSCs imaging in different conditions

Impact of MSCs delivery routes

We compared two MSCs delivery routes, ET or IV. Using the automatic cell counting algorithm, we computed the mean number of detected cells for both conditions in each rat (Figure 4.5). We observe significantly more MSCs in ET than IV with a mean number of detected cells of 3.6 compared to 0.5, respectively (Mann-Whitney test with p = 0.02) (Table 4.1, control column).

Impact of RILI

To evaluate the impact of radiation damage on MSCs imaging, we developed a rat model of RILI. We compared images from control rats and irradiated rats (RT) using the cell counting algorithm. We observed an increase in the mean number of detected cells in RT compared to control for both groups with 3.6 cells for controls and 5.4 for RT in the ET group, and 0.5 for controls and 0.8 for RT in the IV group (Figure 4.6). However, these differences did not reach statistical significance (Mann-Whitney test with p = 0.39 for ET and p = 0.63 for IV).Table 4.1 summarizes the mean number of detected cells per condition.

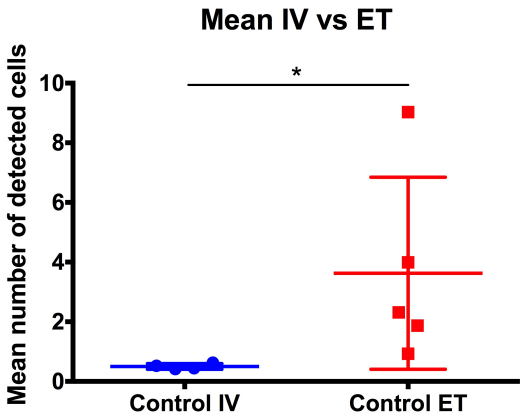

Figure 4.5 **Mean number of detected cells for intravascular and endotracheal injection.** The mean number of detected cells was computed for each video and each rat (each point is one rat with two videos per rat). The horizontal bars represent the mean and standard deviation. The mean number of detected cells differed significantly with 0.5 for IV and 3.6 for ET (p=0.02).

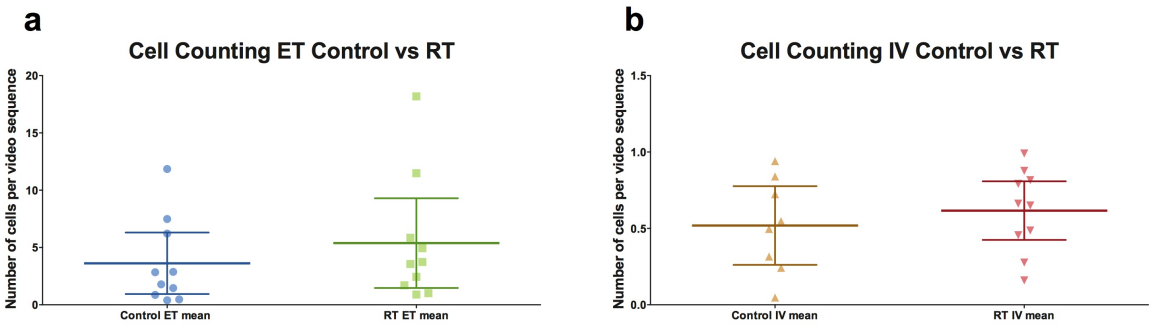

Figure 4.6 **Mean number of detected cells in control and irradiated rats for intravascular and endotracheal injection.** Each point represents a video (two videos per rat) and the horizontal bars represent the mean with 95 % CI. A higher mean number of detected cells was observed in the radiation group for both ET with 3.6 for control and 5.4 for irradiated and IV with 0.5 for controls and 0.8 for irradiated. However, those differences were not statistically significant.

Table 4.1 Mean number of detected MSCs calculated with the automatic cell counting algorithm for each condition.

Mean number of detected MSCs	Control	Irradiated (RT)
Endotracheal (ET)	3.6	5.4
Intravascular (IV)	0.5	0.8

We also computed the total number of cells for each video sequence. We obtain a mean total number of cells of 3698 for Ctrl MSC-ET and 5488 for RT MSC-ET, and 516.9 for ctrl MSC-IV and 612.4 for RT MSC-IV. The total number of cells also shows a higher number of cells in the RT groups, however these differences did not reach statistical significance either.

4.4.4 Histology and Microscopy

Following *in vivo* fluorescence endomicroscopy imaging, lungs were harvested, fixed frozen and sectioned. Lung sections were also stained for nuclei in the tissue. We were able to detect previously labeled and injected DiD-MSCs for both ET and IV delivery (Figure 4.7). However, very few cells were detectable in lung sections.

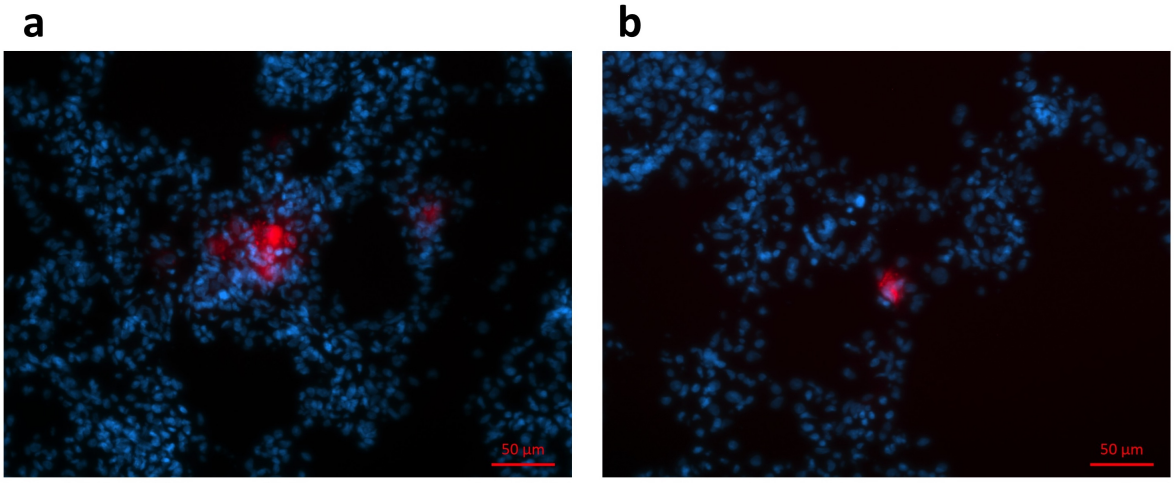

Figure 4.7 **Fluorescence microscopy of lung sections post-endomicroscopy imaging.** MSCs appear red stained for *in vivo* imaging with DiD. Nuclei stained blue with DAPI. (a) Lung sections of rat where MSCs were injected ET and (b) IV.

4.5 Discussion

We proposed and evaluated the use of fluorescence endomicroscopy imaging to detect MSCs in the lungs. We were able to detect fluorescently labeled MSCs injected both IV and ET as well as in a RILI model. We also developed an automated cell counting algorithm to calculate the mean number of cells detected in endomicroscopy video sequences.

The choice was made to use DiD as a labeling method for its ease of use and its low cell toxicity. DiD being a lipophylic dye, it is expected to remain confined into the lipid bilayer of the cell membrane, as has been demonstrated by previous studies [72].However, it is possible for the dye to transfer from the labeled cell to an unlabeled adjacent cell if the membranes are in contact. The labeling becomes less intense as the dye is diluted each time the cell divides. Fluorescent debris might occur if the cell dies or the membrane breaks. Debris would appear smaller than cells and we implemented in our counting algorithm a size constraint as well as a roundness shape structure to take this issue into account. Debris of dead cells could also be taken up by macrophages and the labeling would be on macrophages instead of MSCs thus creating possible false positives. In our case, the experimental time frame was specifically chosen to mitigate such concerns; cells were labeled 2 days prior to injection and washed so that the excess dye outside the cells (background) was removed. Cells were injected and rats were immediately imaged with microendoscopy, so that DiD would not have sufficient time to be released from the cells by the time we imaged. After a few hours or days, the dye is released by the dying MSCs or MSCs fusing with other cells and then, specificity in the detected signal may be lost. However, the timing between injection and imaging was kept tight and no degradation of DiD was observed. Extensive testing of the stability of DiD labeling of MSC *in vivo* was deemed outside the scope of the present study. Nonetheless, the study was designed such that there is very little time between injection and imaging to avoid any possible loss of specificity of the detected signal, which was not observed in our studies. DiD was used by others to image cells 5 days after labeling and injection [72]. While we cannot rule out that some DiD did leak out of the membrane, the manufacturer of the dye clearly states that DiD does not readily transfer to unlabeled cells. While the dye could be taken in by phagocytes after MSC death but not necessarily re-integrated in membranes by other cells, the labeling in the cells would then be much lower or exhibiting distinctive pattern than that of MSC. We used a simple membrane dye to label MSCs, but this method is amenable to many different labeling solutions. For example, MSCs could be labeled with two different colors and/or with a reporter gene system. Cell labeling can also be combined with anatomical or functional markers to answer more advanced biologically relevant questions.

IV MSCs injection showed much fewer cells on the images compared to ET. Our goal is to track the administrated MSCs and monitor their interaction with the lung epithelial tissue, which is more likely to impact the ability of these cells to reverse radiation-induced lung injury. The fact that microendoscopy is a surface optical imaging helps with this regard. This explains why ET injected cells, which appear on the same side of the lungs as the endoscope probe

could be tracked and imaged well. IV injected cells can be detected but to a limited extent since some may have extravasated to the airways but many remain in the capillaries deeper below the surface. It is likely that some may still after longer periods become visible but such waiting raises other problems in terms of dye dilution and it is outside the scope of the current work.

The lung being a large organ and the endoscope tip being somewhat rigid, we are limited in terms of the surface or the volume of the lung that we could cover. This is a common limitation of all microendoscopic devices, which need direct contact to surface tissues in order to perform resolution imaging. However, our goal is to localize the presence or absence of MSCs in areas of the lung with suspected damage. Other methods are more appropriate for whole organ imaging such as PET, however this would provide a macroscopic image of where the majority of cells are located if there is enough of them in close proximity to produce a detectable signal and it lacks the necessary resolution to address cellular level distribution. By using microendoscopy, we obtain a microscopic view of MSCs distribution within the organ at the cellular level. This allows us to quantify cells at microscopic resolution *in vivo*. More importantly, we are interested in the paracrine interaction between lung cells and injected MSCs. The interpretation of results that ET cells are likely to be more confined to the lung, then, a surface imaging method is sufficient to address the question at hand as such cells would be within the proximity of the endoscope probe. However, many IV injected cells may still remain in the capillaries of lungs and in the general circulation, which are less accessible by this method and also explain why they are less likely to have an impact in repairing lung injury as shown by our previous results.

We tested this method on a RILI model and on average we detected more MSCs in irradiated lungs compared to controls. Since the variability in detected cells number is so large between frames of a video sequence (for example, sometimes detecting no cell and sometimes 10), the standard deviation on the mean was too wide to reach statistical significance. The MSCs injection happening at the time of imaging shows that an increased number of cells in RT is probably not due to the homing effect. We hypothesize that because the lung was injured and the tissue is collapsing following irradiation, upon MSCs injection, more cells were visible as they were more confined in injured lungs compared to normal tissue.

We developed and validated an automatic cell counting algorithm which yields results consistent with visual counting with differences similar to those observed between observers. However, our image analysis was based on treating each video frame as a stand alone image and averaging over all the frames present in the video sequence. That means that double-counting of cells may occur in consecutive frames of the same region, for example. Due to the nature of the microendoscopy videos (see supplementary sample video), it is not possible to keep track of

each cell individually. From one frame to the other, cells may appear and disappear and there is no current way of knowing if it is a new cell or a cell that is coming back after having skipped a few frames. Due to respiratory motion and heartbeat, the cell count could be varying between adjacent or subsequent frames. Therefore, the average number of cells seem to represent the best estimate to quantify the cell count in these videos.

The endoscope probe was moved manually through the lungs and it is therefore not possible to know the exact distance covered by the video sequences. One of the drawbacks of this technique is the lack of a positional device tracking system which could provide more information on which part of the lung is being imaged at which time. When looking at the images alone we are unable to distinguish the location within the lung with accuracy. An improved deployment of such technology could consist of image-guided endomicroscopy to determine the location of the probe, which can then be correlated with fluorescence images acquired in real time.

We aimed to explore the potential of fluorescence endomicroscopy as a novel method to track MSCs *in vivo* for repair of radiation-induced lung injury. To the best of our knowledge, this is the first application of endomicroscopy for live tracking of MSCs in such lung injury model. Moreover, the method allows for real-time detection of administered cells *in vivo* with cellular resolution and can be used for studies of cell tracking in other injury models as well. We acknowledge the limitation characteristics of any optical-based imaging technique; however, there is significant value in the results presented here in that it demonstrates the feasibility of using endomicroscopy in accessible organs, such as the lungs, to help resolve current questions pertained to stem cell lung treatment, including the efficacy of different administration routes. Therefore, our study results show great promise for further developing this technology with potentially other cell types or different injury models.

In conclusion, fluorescence endomicroscopy is a powerful new technique to follow stem cells in damaged lungs but more work is still needed to increase its potential for stem cell therapy imaging.

4.6 Methods

All experiments were approved by the Animal Care Committee at the Research Institute of the McGill University Health Centre and in accordance with the ethical guidelines of the Canadian Council on Animal Care.

4.6.1 MSCs Isolation and Culture

MSCs were isolated as previously described [70]. Briefly, femurs of female Sprague-Dawley rats were harvested. Bone marrow was flushed through the bone, filtered (70 μm) and pelleted by centrifugation at 300 g for 5 minutes. Cells were counted (cell counter) and plated in T75 flasks at a density of 500,000 cells per cm^2. MSCs were cultured in Mesenchymal Stem Cell Growth Medium (MSCGM, Lonza, Switzerland) supplemented with antibiotic-antimycotic (Invitrogen, Thermo Fisher Scientific, USA). Media was changed after 24 h to select for adherent cells and subsequently every 3 days until 80 % confluence was reached. MSCs were expanded and passaged as needed, never exceeding passage 4 for injection to rats.

4.6.2 MSCs Labeling

DiD (Vybrant ®DiD Cell-Labeling Solution, Thermo Fisher Scientific, USA) was chosen to match the red channel (660 nm) available on the endomicroscope with absorption peak of 650 nm and emission of 670 nm. DiD was mixed with MSCBM media at a concentration of 10 μM and added to MSCs in culture. MSCs were incubated with DiD-media for 30 minutes at 37 °C in 5 % CO_2. Following incubation, MSCs were washed twice with 1X sterile DPBS and fresh media was added. The next day, MSCs were checked for proper labeling with fluorescence imaging. Previous *in vitro* tests demonstrated no effect on cell survival when MSCs were labeled with DiD.

4.6.3 MSCs Administration

For intravascular injection: 1 million DiD-labeled MSCs were resuspended in 1 mL of sterile DPBS and injected through canulation of the jugular vein at slow speed to prevent embolism. For endotracheal injection: 200,000 cells were resuspended in 0.2 mL of sterile DPBS and directly administered in the trachea through tracheotomy.

4.6.4 Tracheotomy

Tracheotomy in laboratory rats has been described before [73]. All surgical procedures were performed using sterile technique and under intramuscular anesthesia with ketamine/xylazine. Rats were immobilized in supine position on the surgical table. A midline cervical skin incision was done, and the cervical trachea was exposed by vertical separation of the muscles. A 14G catheter was passed through the trachea to allow the endoscope probe to pass.

4.6.5 Fluorescence Endomicroscopy Imaging

All imaging procedures were conducted with rats under intramuscular anesthesia with ketamine/xylazine. The fiber optic probe of the endomicroscope (Cellvizio dual band, Mauna Kea Technologies, France) was inserted through tracheotomy into the airways. Images were acquired in the red channel (660 nm) immediately post injection with 2 consecutive acquisitions of 2 minutes length for each animal. This short time frame aims to ensure that DiD is still confined to the lipid bilayer and hence, to reduce possible loss in detected signal specificity. Due to bronchial architecture and operator expertise the probe was most likely to be directed to the right lung where RT damage was present.

4.6.6 Rat Model of RILI

A rat model for radiation-induced lung injury was established. Sprague-Dawley female rats were anesthetized with isoflurane and were imaged on a computed tomography (CT) simulation scanner (Philips Brilliance Big Bore, Philips Medical Systems, Bothell, WA, USA) following an optimized small animal protocol (120 kVp X-ray tube voltage, 175 mA tube current, 0.37 mm in-plane resolution, 0.4 mm axial resolution). To this end, the animals were placed in a prone position on an in-house built Styrofoam holder with reference markers for positioning reproducibility. The lungs, heart and spinal cord were contoured on the CT images. A single fraction of 18 Gy was prescribed to the right lung with a 6 MV photon beam. A hemithorax parallel-opposed 3D conformal treatment plan was designed (Eclipse™V 11.0, Varian Medical Systems, Palo Alto, California, USA) for each individual animal based on the CT image. Each plan was adapted to animal's anatomy as shown in the CT image to avoid a toxic level of radiation to the spinal cord, heart and left lung. The prescribed dose was delivered using a clinical Novalis Tx linear accelerator (Varian Medical Systems, Palo Alto, California, USA). Anesthetized rats were positioned relative to the markers established at the planning CT. For each rat prior to irradiation, final positioning accuracy was established using cone beam CT.

4.6.7 Image Analysis and Quantification

Regarding video sequence analysis, we treated each frame individually as a stand-alone image. Images were analyzed with Matlab (The Mathworks, Inc., USA). We first enhanced the contrast of the image. Then we applied a granulometry algorithm (as previously described in the Matlab image processing toolbox example "granulometry of snowflakes") to our images in order to

determine the size and number of objects (cells) present in the image without actually detecting individual objects first. To extract the cells, we opened the image with a disk structuring element of radius determined previously to obtain the granulometry image. A double threshold was subsequently applied to the resulting image to select fluorescent cells over background and the image was segmented in black and white. The threshold was determined visually and adjusted for each condition (IV or ET) to encompass the bright objects. Using connected components analysis each detected object was counted.

In order to validate, this automatic cell counting method, we randomly selected 200 frames for the IV group and 200 for the ET group. Cells were visually counted on all random frames by two independent observers and the average of the two was used as ground truth for validation. The automatic cell counting algorithm was applied on the same frames and the concordance correlation coefficient (CCC) was computed.

Following validation the automatic cell counting algorithm was applied to all video sequences yielding cell number per frame for each video. The average cell count was extracted for each video and each rat.

4.6.8 Histology and Microscopy

Following the imaging session, rats were euthanized and lungs were harvested. They were frozen in OCT (Tissue-Tek™O.C.T. Compound, Electron Microscopy Sciences, USA) and stored at -80 ^{o}C shielded from light. Lung sections were cut and stained with DAPI ((4',6-Diamidino-2-Phenylindole, Dihydrochloride), ThermoFisher Scientific, USA) in order to detect cell nuclei and fluorescent DiD-MSCs. Images were acquired on a fluorescence microscope (AxioVert A1, Zeiss, Germany) with filters mPlum for DiD and DAPI and magnification 20X.

4.7 Acknowledgments

This work is partly supported by the Canadian Institutes of Health Research (CIHR) grants MOP-114910 and MOP-136774. Partial support to J.P. and S.L. for this work came from the Natural Sciences and Engineering Research Council (NSERC) Medical Physics Research Training Network CREATE grant # 432290.

4.8 Author contributions statement

J.P., J.S. O.L. and I.E.N conceived the experiment(s), J.P., N.Y., F.C., S.L., M.S., and O.L. conducted the experiment(s), J.P. analyzed the results. All authors reviewed the manuscript.

Chapter 5

A comparative analysis of longitudinal computed tomography and histopathology for evaluating the potential of mesenchymal stem cells in mitigating radiation-induced pulmonary fibrosis

Jessica R. Perez, Sangkyu Lee, Norma Ybarra, Ola Maria, Monica Serban, Krishinima Jeyaseelan, Li Ming Wang, Jan Seuntjens and Issam El Naqa

Article published in: *Scientific Reports* [21]

5.1 Preface

In chapter 4, we established an imaging method to detect and visualize fluorescently labeled MSCs in a rat model of RILI. The next question was: do they have a beneficial effect and contribute to mitigating RILI? In order to assess MSCs potential, we needed to be able to quantify the extent of RILI and use it as an end-point. The objective of this chapter was to follow our RILI rat model receiving stem cell therapy with computed tomography (CT) imaging over time and evaluate the impact of MSCS on the evolution of of RILI. Imaging results were compared to histopathology as the gold standard to evaluate the extent of lung fibrosis.

5.2 Abstract

Radiation-induced pulmonary fibrosis (RIPF) is a debilitating side effect that occurs in up to 30% of thoracic irradiations in breast and lung cancer patients. RIPF remains a major limiting factor to dose escalation and an obstacle to applying more promising new treatments for cancer cure. Limited treatment options are available to mitigate RIPF once it occurs, but recently, mesenchymal stem cells (MSCs) and a drug treatment stimulating endogenous stem cells (GM-CSF) have been investigated for their potential in preventing this disease onset. In a pre-clinical rat model, we contrasted the application of longitudinal computed tomography (CT) imaging and classical histopathology to quantify RIPF and to evaluate the potential of MSCs in mitigating RIPF. Our results on histology demonstrate promises when MSCs are injected endotracheally (but not intravenously). While our CT analysis highlights the potential of GM-CSF treatment. Advantages and limitations of both analytical methods are contrasted in the context of RIPF.

5.3 Introduction

Lung cancer remains the leading cause of cancer death with a very low 15% 5-year survival rate. Radiotherapy (RT) is one of the most commonly used treatments and it is estimated that about 50% of cancer patients will undergo RT at some point during the course of their treatment [7]. Side-effects from RT are a major limiting factor preventing dose escalation for potential better tumor control and overall survival. RT side effects or radiation-induced lung injury occur in about 30% of thoracic irradiation [5] and can be divided into two phases: an early inflammatory phase named pneumonitis occurring weeks following treatment, and a later fibrotic phase (RIPF) that occurs months to years post-RT. Clinical symptoms include dyspnea, cough, respiratory insufficiency that can seriously impact patients' quality of life and in extreme cases lead to death. The exact molecular mechanisms behind RIPF remains an area of active research. It involves a cascade of events including direct DNA damage, cell death, the release of inflammatory cytokines, the recruitment of immune cells and the remodeling of the extra-cellular matrix eventually leading to scar formation and lung fibrosis [7, 23].

Limited treatment options are available for RIPF and involve mostly steroids and oxygen inhalation with marginal success [23]. One of the promising experimental treatment options currently being investigated is the use of Mesenchymal Stem Cells (MSCs). They exhibit immunomodulatory properties, which can help reduce inflammation and further prevent damage

leading to fibrosis [55]. MSCs have exhibited great promise in the treatment of pulmonary fibrosis in pre-clinical models [74, 75]. MSCs can be harvested, cultured and then injected directly into the trachea or systemically intra-venously. An alternative and less invasive option, is to stimulate the host's stem cells so they can be recruited to the site of injury. This can be achieved with the injection of a stem cells-stimulating drug: Granulocyte macrophage colony-stimulating factor (GM-CSF). GM-CSF plays an important role in tissue repair and in the process of pulmonary fibrosis [76] but its detailed function is still an area of active research. The rationale for using GM-CSF is driven by its ability to mobilize autogenous MSCs in each rat instead of injecting allogenic MSCs from other rats. In addition, Moore et al. [76] demonstrated that the deficiency of GM-CSF enhanced pulmonary fibrosis as a result of impaired production of the potent antifibrotic eicosanoid, Prostaglandin E2. The effect of GM-CSF on mobilization of stem cells and reduction of lung fibrosis has been previously established. In this study, we did not aim to re-evaluate these treatment options at a mechanistic level but rather to contrast their efficacy with serial CT imaging and histopathological analyses as a necessary prerequisite for clinical translation.

Current common approaches to assess and monitor RIPF could be divided into: (1) medical imaging: most commonly computed tomography (CT); and/or (2) histopathology, which remains the gold standard.

Medical imaging can be used to visualize and monitor the onset of RIPF. Radiological evidence of RIPF is part of diagnosis alongside clinical presentation of symptoms [15]. CT is readily available in the clinic and is a powerful tool to image RIPF. CT imaging being based on density changes, the lung is an ideal candidate organ. On CT images, air appears black (low density, -1000 Hounsfield units (HU)), bones appear white (high density, 700 to 3000 HU) and soft tissues are in between with a density comparable to water (0 HU). In the case of RIPF, edema, immune cells infiltrates and fibrosis all contribute to increasing the density of the lungs and therefore, it is possible to visualize those changes non-invasively and longitudinally over time with serial CT imaging [29]. CT density changes have been shown to correspond to the dose of radiation in a mouse model, typically exhibiting changes above 10 Gy [77]. Density and morphological changes were observed in a mouse model of RIPF with CT imaging and interestingly, those changes appeared prior to the onset of clinical symptoms [78]. Rather than qualitatively assessing average density variations or scoring morphological differences, the quantification of RIPF on CT images was proposed by using the density distribution or histogram of the lung in order to get a more reproducible measure independent of the observers [79]. The idea of using CT density changes in monitoring RIPF (and correlating these with

radiation dose) is not new [80, 81] and has been successful and implemented routinely in the clinic. With the advent of new imaging technologies the quality of CT images obtained has increased dramatically and therefore allowed for the detection of more subtle changes, even in small animals. CT density changes over time were previously compared to histological findings in a rat model but did not lead to conclusive correlation with the average lung density most probably because of the focal development of fibrosis in different lung regions [82]. Recently, Reddy et al [75] demonstrated anti-fibrotic efficacy of MSCs in comparison to pirfenidone in a bleomycin-induced pulmonary fibrosis model using high resolution CT.

Histopathology allows the detection of RIPF at the cellular level with standard evaluation of tissue architecture on hematoxylin & eosin (H&E) slides by a trained pathologist. Specifically, by staining the tissue with fibrosis targeted dye: Masson's trichrome that makes collagen, the main component of fibrosis, appear blue. Masson's trichrome staining can be evaluated by visual inspection with a fibrosis scoring scale such as the Ashcroft scale or a modified version of it [83], or quantified using an automated software based on color, determining the amount of blue pixels. Dong et al [74] used histopathology techniques to demonstrate that anti-fibrotic effects of MSCs on irradiated lungs could be related to host secretions of hepatocyte growth factor (HGF) and prostaglandin E2 (PGE2).

In this work, we assess the potential of different MSCs treatment routes in mitigating RIPF using both CT and histopathology and contrast their findings, advantages and limitations in each case. A rat model of RIPF was established in a clinical setting including CT simulation, treatment planning and radiation delivery on a clinical linear accelerator. Following irradiation, the rats were treated for RIPF with MSCs or drug stimulation and monitored longitudinally with serial CT imaging. Following standard convention, after 24 weeks of follow up, stable RIPF was observed and quantified with histopathology and compared to longitudinal CT images.

5.4 Results

5.4.1 Onset of RIPF over time on serial CT images

Female Sprague-Dawley rats (Charles River Laboratories, QC, CA) were divided into 5 groups (25 total, n = 5 per group): Non-irradiated control (Control), Irradiated (RT), Irradiated and treated with GM-CSF drug (RT+Drug), Irradiated and treated with MSCs injected intravenously (RT+MSC-IV), and Irradiated and treated with MSCs injected endotracheally (RT+MSC-ET). We followed the rats with serial CT imaging every 2 weeks for 24 weeks post-irradiation. The

time line of 24 weeks was chosen based on extensive pilot studies following the onset of fibrosis in our RIPF rat model. It is also consistent with previous literature as in Dong et al (2015) [74] in which the study was terminated after 24 weeks, when fibrosis became stable but animal conditions worsened.

Figure 5.1 shows CT images of a representative rat with irradiated lung. We begin to observe changes in lung appearance visually at 10 weeks post RT (Figure 5.1b and e). Lung injury and fibrosis being denser than air, appears brighter on CT images compared to normally aerated lungs. Moreover, we note that the irradiated lung volume shrinks and gets denser over time prior to onset of RIPF. Interestingly, we also observe a shift in the heart and mediastinum towards the injured lung (Figure 5.1c and f).

We quantified the density of the irradiated lung (ipsilateral) by taking the average density of the lung region-of-interest (ROI) and normalizing it to the unirradiated lung (contralateral). We observe an increase in density over time in all radiation groups whereas the sham irradiation control group remains stable (Figure 5.1g). The RT+Drug group shows a consistent trend of lower densities than the other RT groups (Figure 5.1g, green curve). In order to capture differences in density between groups over time, we computed the average of the last 6 weeks of follow-up between week 14 and 24 post-RT (Figure 5.1h). All RT groups exhibit a statistically significant increase in lung density compared to Control ($p < 0.0001$). The RT+Drug group shows a significantly lower density than the other RT groups (RT+Drug vs RT: $p = 0.0045$; RT+Drug vs RT+MSC-IV: $p = 0.0094$; RT+Drug vs RT+MSC-ET: $p = 0.0472$) (Figure 5.1h).

5.4.2 Fibrosis quantification with CT histogram analysis

For each CT image (0.37 mm in plane and 0.4 mm axial resolution), we extracted a histogram of the lung ROI. In the irradiated groups the shape of the histogram varies over time. Figure 5.2a shows the changes in histogram over time for a representative irradiated lung ROI.

Based on the appearance of the histogram peaks, we qualitatively established two sections of the histograms: (1) the normal lung, ranging from -900 to -400 HU and (2) the fibrotic lung, ranging from -200 to 200 HU (Figure 5.2b). In CT, -1000 HU represents air and -500 HU lungs, so the normal lung section exhibits aerated regions of the lung, whereas 0 HU represents water and tissues which indicates poorly aerated lung regions consistent with fibrosis. As shown in Figure 5.2a, the fibrotic lung region appears at week 8 and keeps increasing as the number of voxels in the normal lung region decreases. We observe changes in lung appearance visually on

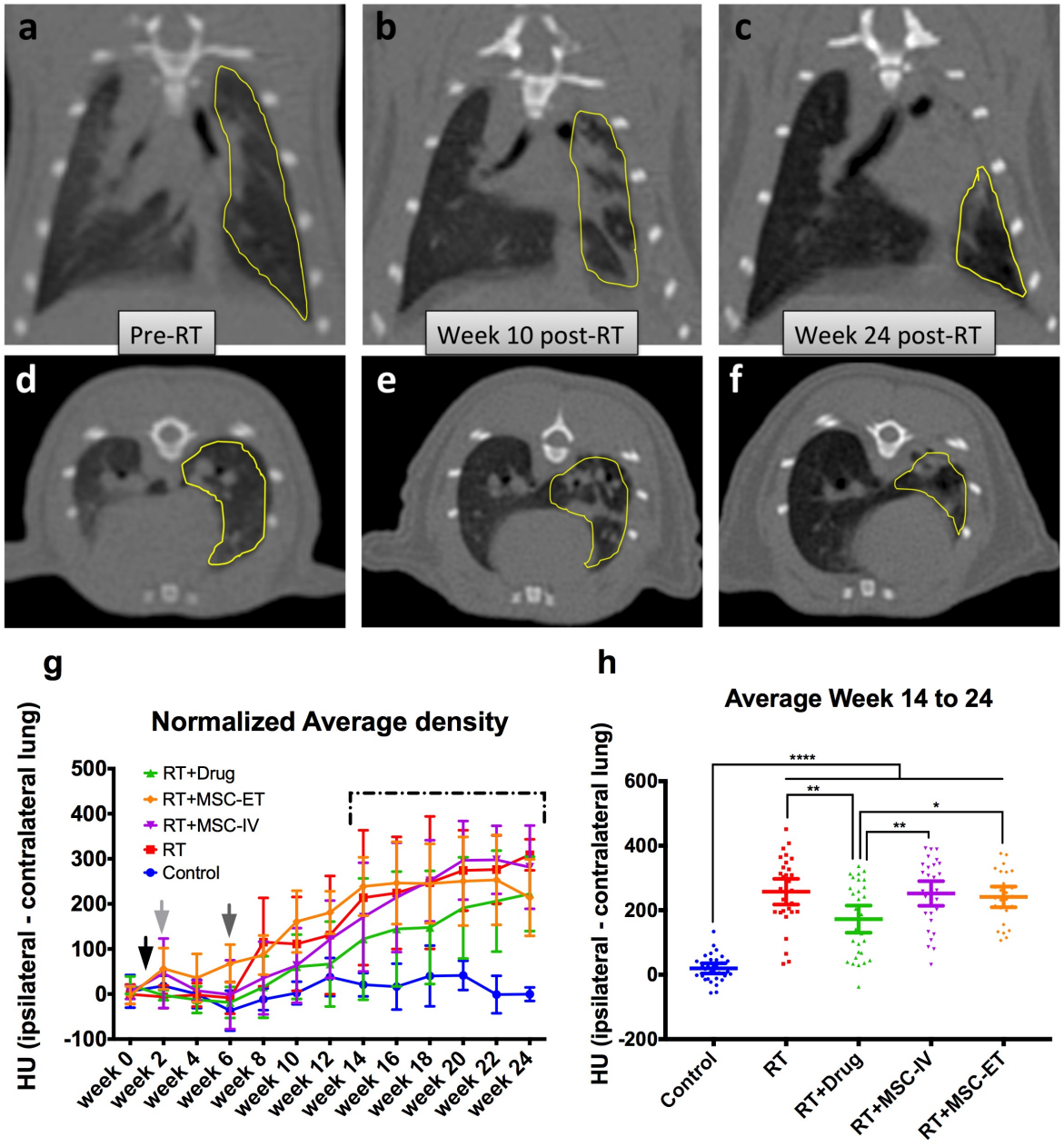

Figure 5.1 CT images of a representative rat over time. Irradiated lung contour highlighted in yellow. a) Frontal view before RT. b) Frontal view 10 weeks following RT. c) Frontal view 24 weeks after RT. d) Transverse view prior to RT. e) Transverse view 10 weeks following RT. f) Transverse view 24 weeks post-RT. g) Normalized average CT density over time for every groups. The Control group lung density remains stable whereas the RT groups show an increased density. Black arrow: RT delivery and start of Drug or MSC injection treatments. Light gray arrow: end of Drug treatment. Dark gray arrow: end of MSC treatments. Dashed line: Averaging period shown in h. h) Average lung density averaged over week 14 to 24 for each group. Bars represent the mean and 95% CI. There is a statistical difference between Control and all RT groups and between RT+Drug and the other RT groups.

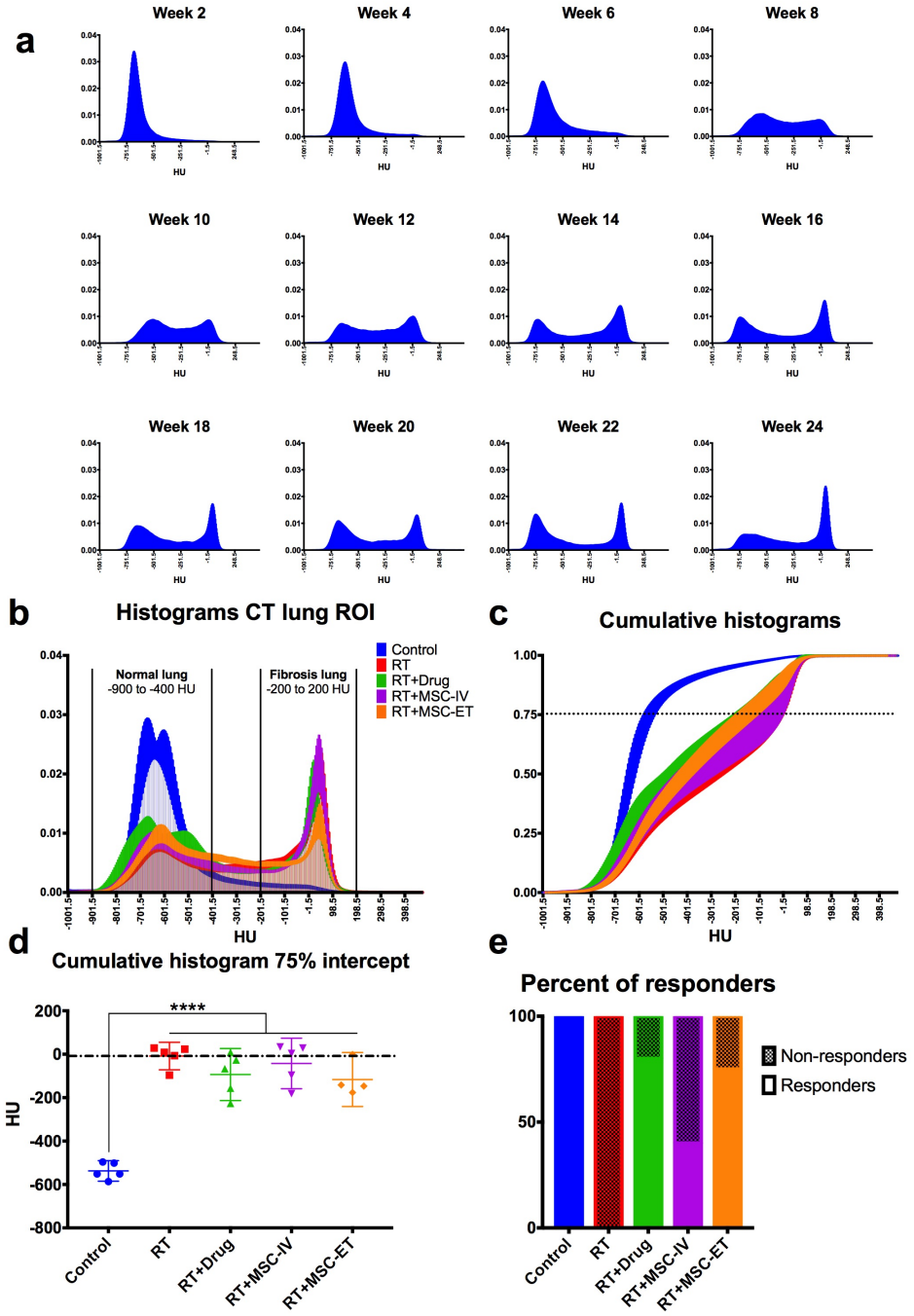

Figure 5.2 a) CT histograms of lung ROI from a representative irradiated rat over time (from week 2 to 24 post-RT. Histograms represents the portion of voxels within the lung ROI at a certain density (HU). b) CT histograms for all groups at week 24 post-RT. c) Cumulative histograms at week 24 post-RT. Dotted line at the 75% intercept line to maximize separation between groups. d) HU value of the 75% intercept from the cumulative histogram for each group. Bar represents the mean with 95% CI and each point is a rat. There is a significant difference between the Control and all RT groups. Dashed line was set at the mean of the RT group. e) Percent of rats exhibiting a response to treatment. Rats falling under the mean of the RT groups (dashed line from d) are considered "responders" (closer to Controls) and rats above the RT mean are considered "non-responders".

CT images at week 10 (Figure 5.1b and e). But, when examining quantitatively the shape of the histogram over time, we observe that change takes place earlier at 8 weeks post-RT.

The difference in histograms between the different groups was quantified at week 24 post-RT. Figure 5.2b shows the combined histograms of all groups. We observe that the control group's histogram peaks in the normal lung section with small tail in the fibrotic section. In comparison, all irradiated groups show a fibrosis peak with a majority of voxels accumulating in the fibrosis region and a much smaller peak in the normal lung section.

We can also visualize the histograms' differences by plotting the cumulative histograms for each group. It clearly appears that the Control group reaches unity much sooner than the RT groups (Figure 5.2c). In order to quantify the differences between groups, we chose to look at the 75% intercept line (Figure 5.2c, dotted line), where the spread among groups is maximal [79]. Figure 5.2d shows the 75% intercept from the cumulative histogram for all groups at week 24. There is a significant difference between Control and all RT groups ($p < 0.0001$). Despite the limited number of rats per group, we observe that some animals from the treated groups show a response to MSCs treatment as their lung appear less dense than the lungs of the RT group (closer to the Control). Figure 5.2e shows the percent of "responders" falling under the mean of the RT group (under the dashed line in Figure 5.2d. We show that 80% of rats in the RT+Drug group, 40% of the RT+MSC-IV group and 75% of the RT+MSC-ET group exhibit some response to stem cell treatment (Figure 5.2e). There is no statistical significance at the group level to conclude that there is a response from these groups, however, the observation that some subjects seem to react slightly to treatment might indicate where to focus future research direction.

5.4.3 Fibrosis quantification with histopathology

In order to better interpret the CT results, we compared them to the histopathology gold standard. After 24 weeks of follow-up, the lungs were harvested, divided in upper, middle and lower lobes, fixed, sectioned and stained with Masson's trichrome for fibrosis.

Figure 5.3a-d shows Masson's trichrome stained lung slides of Control (Figure 5.3a and b) and RT (Figure 5.3c and d). Whole lung sections from three locations in the lung (upper, middle and lower lobes) were quantified for the percent positivity (the quotient of all blue pixels over all pixels which registers a color expressed as a percentage). Histological data shows an increase of fibrosis in RT (more blue) compared to Control (Figure 5.3a and c). Figure 5.3e shows a statistical difference between Control and all RT groups (Control vs RT and RT+Drug:

$p = 0.0002$, Control vs RT+MSC-IV: $p < 0.0001$, Control vs RT+MSC-ET: $p = 0.0334$) and also between RT+MSC-IV and RT+MSC-ET ($p = 0.0350$).

5.4.4 CT and histopathology comparison

Histology can provide only a snap shot of time. Therefore, we attempted to compare the corresponding CT results from week 24 to the histopathology data. Figure 5.3f shows fibrosis quantification from CT and histopathology for each rat in a scatter plot. We observe a linear response between increased CT HU and increased percent positivity in histopathology ($R^2 = 0.4123$). There is a significant correlation between CT and histopathology scoring ($p = 0.0008$) with Spearman rank correlation $r = 0.6494$.

5.5 Discussion

In this work, we used serial CT imaging to longitudinally monitor the onset of RIPF in a rat model, compared results to histopathology and assessed the potential of different MSCs treatment routes in mitigating RIPF.

It is recognized that the translation to human population is a concern, as we are presenting results from a RIPF rat model. These differences across species as well as between different breeds of the same species have been documented and considered by our group. Some animal models are more radio-sensitive or -resistant than others and that may have an influence on the results of such studies. Translation to the human population is a serious concern for every study done using animal models. However, clinical studies for testing the potential of MSC are limited since the efficacy and safety of using these cells is still controversial, and it is premature to test new risky therapies in humans. Therefore, using such animal models as surrogates to establish a method and monitor a disease state are of great value. In our case, we performed all steps of the experiments under the most possible clinically-like conditions: clinical radiation therapy equipment (clinical Linac and clinical CT) to have a relevant RIPF rat model so the same image analysis techniques could be easily translated into patients.

Pulmonary fibrosis is characterized by the excess deposition of extra-cellular matrix with collagen accumulation as its main component [84]. Therefore, histopathological techniques that specifically stain for collagen deposition (Massons's trichrome) are considered a reliable measure of pulmonary fibrosis and remain the gold standard in assessing the extent of fibrosis.

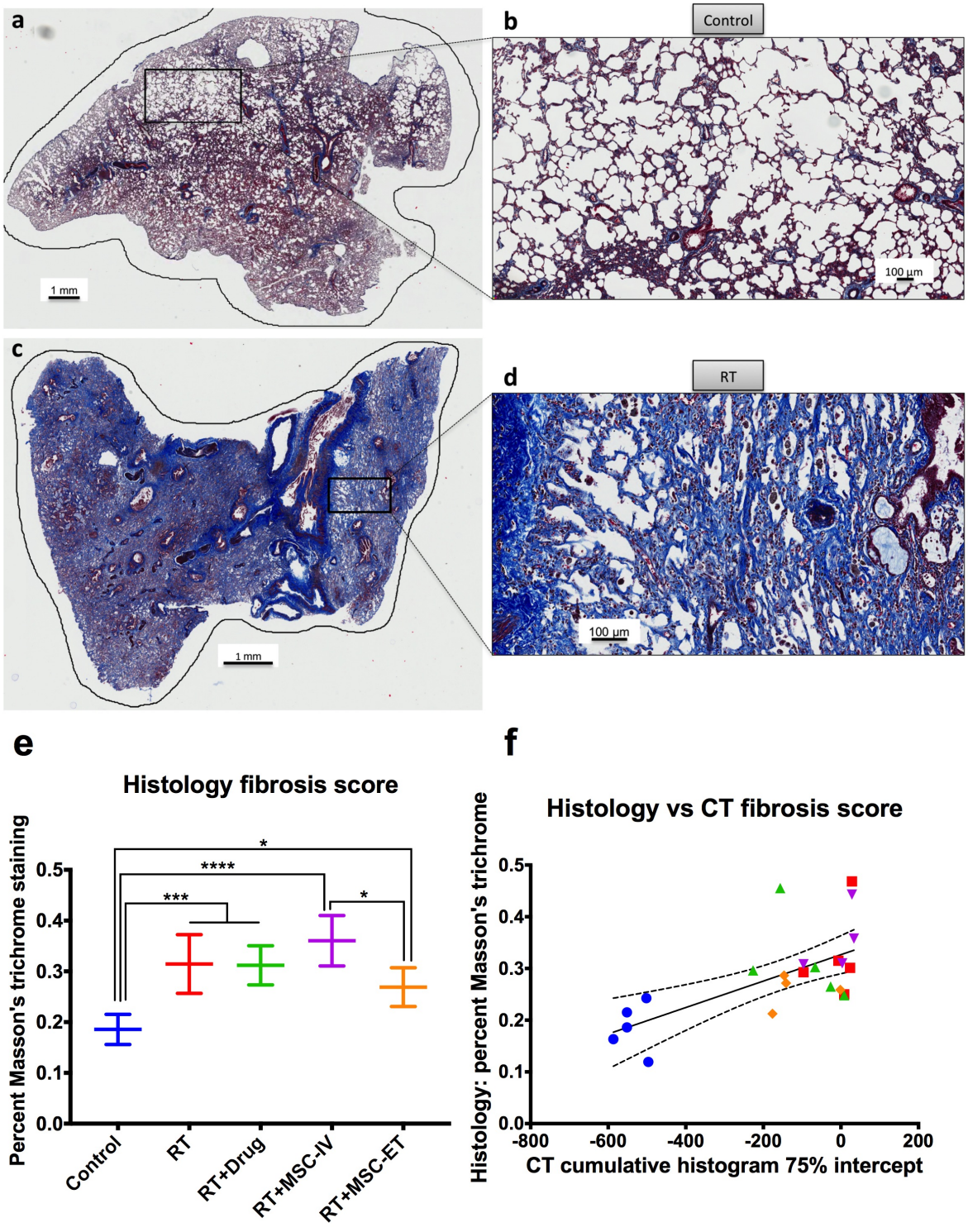

Figure 5.3 Histopathology of representative lung sections stained for fibrosis with Masson's trichrome. a) Control whole slide. b) Control zoomed in. c) RT whole slide. d) RT zoomed in. Fibrosis appears in blue. e) histopathology fibrosis score quantified with percent of blue pixels for each group. There is a statistical difference between Control and all RT groups and between RT+MSC-IV and RT+MSC-ET. f) Plot of histopathology vs CT fibrosis score. Each rat is one point and the line represents the linear regression fit.

We were able to detect changes in CT images as early as 8 weeks post-RT with serial CT histogram analysis. Fibrosis development evolves further on, up to 24 weeks following RT. At this point we were able to directly compare CT information with histopathology fibrosis staining. We observed increased fibrosis in all irradiated groups for both CT and histopathology. In that sense, CT imaging can be a good surrogate to histopathology to monitor RIPF non-invasively and longitudinally.

Our results suggest that treatment with MSCs-ET and endogenous stem cells stimulation with GM-CSF shows promise in the reduction of RIPF. We observe a consistently lower lung density in the RT+Drug group on CT images, from the onset of RIPF, up to the end of our follow up at 24 weeks post-RT. Moreover, histopathology shows less fibrosis in the RT+MSC-ET group. We did not observe an effect when MSCs were injected IV.

The study presents a detailed comparison of different BM-MSCs methods for radiation-induced pulmonary fibrosis and longitudinal evaluation of these methods using serial CT imaging with respect to the gold standard of histopathology at the end of 24 weeks. TGF-β1 is considered a key modulator in the onset and progression of fibrosis. The relationship between MSCs and TGF-β1 has been previously reported [85–87]. In investigations of co-culture analysis by our group [88] and by others in the literature [84] a mechanistic understanding of gene expression was attempted. These types of further mechanistic investigations are, however, beyond the scope of the present study and would be the subject of future research focused on our best candidates for BM-MSCs (ET-MSC and GMCSF).

There are a few caveats in our study. First, we are limited by the number of rats per group (n = 5) since we rely on observing subtle differences and there is a high variability between subjects within any given treatment group.

The number of animals per group (n = 5) is standard to obtain sufficient statistical power. We observed similar results in previous pilot studies with n = 3 per group. In accordance with the animal care guidelines, we attempted to use as few animals as possible to still obtain quantifiable results. The effect of current MSCs dosage on mitigating RIPF may be modest and the damage sustained by the lung following a 18 Gy RT might be too high to reverse it. We performed multiple pilot studies with lower and higher radiation doses (16, 18, 20 Gy) to establish the RIPF rat model protocol. Higher doses and full thorax irradiations has led to poor survivability of the rats. Since we delivered RT to one lung only (hemithorax), the other lung was used as an internal control and was able to compensate for the damaged lung. Therefore, survivability is greatly improved and none of the animals died from RT at a dose of 18 Gy to

the right lung. We also monitored weights and breathing rates and did not observe significant differences between the RT groups and the controls.

The observation period of 24 weeks was based on our previous pilot studies and similar timelines have been used by others too as in Dong *et. al.* (2015) [74]. It is noted that longer follow ups could be used but the benefits of longer periods is unclear.

For collagen staining we used Masson's trichrome, other alternatives are available such as Sirius red or hydroxyproline assays but it is unclear whether this would make a difference in the observed results [89].

Another uncertainty is associated with the fact that we rely on the MSCs homing or getting recruited to the site of injury. MSCs have a short lifespan, so we are assuming that they survive long enough to have a beneficial effect. Variations in the delivery schemes could also impact the effect of MSCs and more research is still required to determine the optimal treatment dosage.

Fibrosis reduction after MSCs injections was not significant, and this protocol needs further investigation to adjust the MSCs dosage in order to reduce fibrosis significantly. In the current study, we focused on evaluating the therapeutic potential of MSCs when administered via 3 different routes. In future studies, comparing our findings to a control group using fibroblast cells would be also of interest in order to further benchmark the potential of MSCs.

If the acute (inflammatory) phase is controlled it will not proceed to a chronic (fibrotic) phase. Therefore, we decided to provide continuous supply of MSCs once a week for 6 weeks to control the acute inflammatory phase. We followed a previous protocol applied to head and neck irradiated mice [90] with some modifications established during pilot studies on our RIPF rat model. Perhaps, this treatment dosage was insufficient to minimize or slow down the onset of fibrosis. Indeed, we did not observe a significant delayed onset of fibrosis in the MSCs group compared to irradiation alone on CT images.

Reddy et al [75] demonstrated the potential of human MSCs transplantation in mitigating pulmonary fibrosis at its early stage in mice and showed consistent results between histopathology and CT, although CT scoring was qualitative. A dedicated small animal scanner was used, however the resolution is comparable to our study. In this scenario, MSCs were administered systemically (IV), but in our case we did not observe any benefit on RIPF in the RT+MSC-IV group. The timeline of the studies is quite different with bleomycin injury leading to much faster onset of fibrosis compared to RT and could potentially explain the differences we see in outcome. Bleomycin injury models do not recapitulate the clinical outcome we are focusing on with RIPF and even though both methods lead to pulmonary fibrosis one should remain cautious as to the exact mechanisms behind the different origins of lung injury. Another critical

difference is the timing of MSCs injection, which was performed every week for 6 weeks in our study but within days after bleomycin injury, that can lead to differences in MSCs efficacy. The use of a different animal model (mice vs rats) is very critical when comparing studies as the biological response to lung injury can vary greatly between different breeds of the same species. Dong et al [74] investigated RIPF in a rat model and demonstrated human MSCs reduced inflammatory factors and histopathological appearance of fibrosis, although histological fibrosis scoring was qualitative. MSCs administration was systemic (IV) and immediately following RT. RT damage in Dong's study was assessed with histopathology at week 4 post-RT by sacrificing a group of animals at that time point. In our study, we observed RT damage at 8 weeks following RT with CT imaging and not histopathology. We only have histopathological results from week 24 post-RT. In addition, 4 weeks is too early for fibrosis onset at this time, the inflammatory process is still taking place and incomplete. Fibrosis consolidation is ongoing and will take longer to settle following our imaging analysis. In their study the rats received a dose of 15 Gy, which is lower than in our study (18 Gy) and that probably lead to less severe lung damage.

We were able to correlate increased CT and histopathological scores in irradiated groups compared to control. However, the correlation between CT and histopathology results disappears when comparing the different irradiated treatment groups. Both methods have advantages, but also suffer from limitations (Table 5.1). One such limitation is that we are limited in the resolution of the CT compared to a histopathology slide especially since we are using a clinical CT as opposed to a dedicated small animal scanner. As we used a clinical linear accelerator, we needed a clinical CT simulation in order to plan the treatment for each individual rat and establish feasibility for clinical translation. For its ease for clinical translation, we therefore used the same clinical CT scanner for the follow up period. With an optimized small animal imaging protocol we were able to reach an in-plane resolution of 0.37 mm, which is adequate to resolve fibrotic details within the lung and extract lung densities. The spatial localization of fibrosis is also tricky to correlate between a 3D image volume and a histopathology slide due to the fixation process and orientation of the tissue for sectioning. For this reason, we performed the analysis on the entire lung ROI on the CT and for histopathology we averaged the values of three different lung regions: upper, middle and lower lobes. Another issue to keep in mind is that we used Masson's trichrome staining that specifically highlights collagen deposition in the tissue, whereas we can only look at increased density on CT images. The biological basis of an increase in lung density is multifaceted and can include aspects such as the accumulation of liquid (edema) or cell infiltrates and of course includes extra-cellular matrix deposition and fibrosis. CT being an anatomical imaging method, only reveals downstream

anatomical changes that are a consequence of earlier molecular events. Having a molecular target for fibrosis imaging may allow us to detect these changes earlier. Future research in the development of targeted molecular imaging probes for RIPF will certainly bridge the gap between CT and histopathology.

Table 5.1 Advantages and limitations of CT and Histopathology

CT		**Histopathology**	
Advantages	Limitations	Advantages	Limitations
• Non-invasive (longitudinal studies) • 3D volume • Clinically translatable	• Anatomical, Macroscopic • Relies solely on density (not fibrosis specific)	• Cellular resolution • Masson's trichrome staining is fibrosis specific • Tissue architecture • Clinically translatable (biopsies)	• Invasive/ex vivo (sample required) • Fixation and sectioning affect tissue • One slice of tissue • Staining procedure

The work presented here is a multidisciplinary effort combining the establishment of a RIPF rat model with MSCs mitigation and monitoring of the disease state with clinically relevant CT imaging compared to the histopathological gold standard. This study contributes to expanding current knowledge of MSC-mediated therapies, including key aspects of cell injection time lines or preferred route of administration, in addition to evaluation methods. More work is indeed needed for stem cells therapy to translate into the clinic and we believe that non-invasive methods based on imaging will play a pivotal role in determining the best ways to achieve this goal.

In conclusion, we were able to monitor RIPF in a pre-clinical setting with CT imaging and histopathology, compared and contrasted both methods for their potential in the assessment of

RIPF mitigating MSCs therapies. More work is required to optimize the use of MSCs in RIPF and imaging will be a valuable tool to bring such new therapies to the clinic.

5.6 Methods

5.6.1 RIPF rat model

All experiments were approved by the Animal Care Committee at the Research Institute of the McGill University Health Centre and in accordance with the ethical guidelines of the Canadian Council on Animal Care.

A rat model of RIPF was established as previously described [20]. Briefly, Sprague Dawley female rats were anesthetized with isofluorane and placed in prone position on an Styrofoam bed. The rats were imaged on a CT-simulator (see section CT imaging for details). Both lungs, the heart and spinal cord were contoured on the CT images. An AP-PA (anterior and posterior parallel opposed fields) radiotherapy plan delivering 18 Gy to the right lung was designed (Eclipse™V 11.0) and delivered on a Novalis Tx linear accelerator (Varian Medical Systems, Palo Alto, California, USA) with prior positioning of each rat using cone beam CT.

5.6.2 MSCs isolation, culture and injection

MSCs were isolated from the bone marrow of male sprague Dawley rats as previously described [70]. Briefly, the femur of the rats were isolated and the bone marrow was flushed out and filtered. The resulting cells were placed in culture in Mesenchymal Stem Cell Growth Medium (MSCGM, Lonza, Switzerland) supplemented with antibiotic-antimycotic (Invitrogen, Thermo Fisher Scientific, USA), that was changed the next day and twice a week following extraction. MSCs were selected for plastic adherence and passaged when reaching 80% confluency. MSCs used for injection did not exceed passage 5. Therefore, MSCs from passage 2 to passage 4 maximum were used for injection. When passaged too many times, changes in size, and potential therapeutic effectiveness of MSCs can affect the results.

MSCs injections were performed the day of irradiation and once a week for 6 weeks following RT. Dosage of MSC injection was obtained from previous extensive pilot studies. The rationale is, if MSCs are provided to irradiated rats for multiple times, this would increase the therapeutic potential of MSCs on lungs compared to controls. We wanted to make sure that MSCs are supplied continuously so that they do not get cleared quickly from the system

before having an effect on the irradiated lungs while still not causing harm (such as pulmonary embolism). Cultured MSCs were detached with trypsin-EDTA centrifuged and resuspended in saline for injections. The cells were injected via different administration routes, either endotracheal (ET) (200000 cells) or intravascular (IV) (1 million cells).

Rat GM-CSF drug (Cedarlane, Canada) was administered following irradiation and for the next 7 days via intraperitoneal injection with a dose of $10\mu g/Kg$.

5.6.3 CT imaging

CT imaging was performed for treatment planning prior to irradiation and every two weeks for 24 weeks post-irradiation. CT imaging was performed on a Philips Brilliance Big Bore computed tomography (CT) simulation scanner (Philips Medical Systems, Bothell, WA, USA) using an optimized rat imaging protocol: 120 kVp X-ray tube voltage, 175 mA tube current, 0.37 mm in-plane resolution, 0.4 mm axial resolution.

5.6.4 Lung CT image analysis

Definition of lung region-of-interest (ROI)

Lung was originally contoured for treatment planning on the baseline CT by CT number thresholding (-1000, -300 HU) and the trachea was excluded. First, a 3-dimensional lung ROI on a baseline CT image was created by isotropically eroding (kernel size: 1 mm) the volume within the lung contour drawn for treatment planning. The erosion was performed to minimize the amount of necessary manual correction on the ROI due to registration error. Then, deformable registration was performed between a post-radiation CT images and the corresponding baseline image. The resulting deformation vector field was applied to the baseline lung ROI to create a corresponding lung ROI for the follow-up CT. The image processing procedures were conducted under the MevisLab platform version 2.3.1 (MeVis Medical Solution, Bremen, Germany).

Characterization of CT density changes after irradiation

To characterize global anatomical changes in lung, we computed the average lung density and we obtained histogram of CT density in Hounsfield Units (HU) of the voxels within the follow-up lung ROI.

Histogram analysis

Lung density values were extracted for each rat ROI at each time point and we generated histograms. We built a cumulative histogram at week 24 and quantified the 75% intercept for each rat.

5.6.5 Lung tissue histopathology and fibrosis staining

After 24 weeks the rats were euthanized and the lungs were harvested, divided into upper, middle and lower lobes, fixed in formaldehyde and sectioned, transversally, for histopathology. Lung sections were then stained for fibrosis (collagen) with Masson's trichrome.

5.6.6 Histopathology staining quantification

Stained lung sections were scanned using a whole slide scanning technique (Aperio ™, Leica Biosystems, USA) at 20X magnification. Fibrosis (collagen) regions appear blue with Masson's trichrome staining, therefore, we quantified the number of blue pixels. To avoid subjectivity in the quantification of histopathology, we used an automatic thresholding method using ImageScope (Leica Biosystems, USA). Each whole-slide image was contoured and large blood vessels and bronchioles were manually removed from the analysis. Then, the color blue was isolated by adjusting the hue values and thresholded to obtain the number of blue pixels. The values represented here are percentages of positivity: number of positive blue pixels over the total number of pixels (representing tissue regions and excluding blank spaces).

Statistical analysis

Differences between groups were assessed with One-Way ANOVA and correction for multiple comparisons. Correlation between CT and histopathology was performed using Spearman rank correlation.

Significance of p value is represented as follows: $p > 0.05$: ns, $p \leq 0.05 : *$, $p \leq 0.01 : **$, $p \leq 0.001 : ***$ and $p \leq 0.0001 : ****$.

5.7 Acknowledgements

This work is partly supported by the Canadian Institutes of Health Research (CIHR) grants MOP-114910 and MOP-136774. Partial support to J.P. and S.L. for this work came from the Natural Sciences and Engineering Research Council (NSERC) Medical Physics Research Training Network CREATE grant # 432290.

5.8 Author contributions statement

J.P., S.L., O.M. and I.E.N. conceived the experiment(s), J.P., S.L, N.Y., O.M., M.S., K.J. and L.M.W. conducted the experiment(s), J.P., S.L., and J.S. analyzed the results. All authors reviewed the manuscript.

Chapter 6

Image-Guided Fluorescence Endomicroscopy: From Macro- to Micro-Imaging of Radiation-Induced Pulmonary Fibrosis

Jessica R. Perez, Norma Ybarra, Frederic Chagnon, Monica Serban, Gabriel Pare, Olivier Lesur, Jan Seuntjens and Issam El Naqa

Article submitted to: *Scientific Reports*

6.1 Preface

In chapter 5, we monitored the effect of MSCs on RILI with longitudinal CT imaging as an end-point. However, CT imaging is limited to visualizing anatomical and macroscopic tissue changes. The first objective of this chapter was to develop a molecular imaging method to assess RILI at the microscopic level. We developed and validated the use of a collagen targeted fluorescent probe to image RIPF with FE imaging. However, the use of FE imaging is hindered by the lack of a localization component, preventing us from locating the position of the endoscope at the time of imaging and knowing from where in the lung the FE images came from. Therefore, the second objective of this chapter was to use image guidance in order to detect the endoscope position at the time of FE imaging. This position was then mapped back

to the corresponding CT image to obtain a 3-dimensional location of the endoscope. With this method, we were able to image RIPF both macro- and microscopically at the anatomical and molecular level.

6.2 Abstract

Radiation-induced pulmonary fibrosis (RIPF) is a debilitating side effect of radiation therapy (RT) of lung and breast cancers. Current methods to assess and monitor RIPF involves diagnostic computed tomography (CT) imaging, which is restricted to anatomical macroscopic changes. Fluorescence endomicroscopy (FE) in combination with a fibrosis-targeted fluorescent probe allows to visualize RIPF at the microscopic level. However, a major limitation of FE imaging is the lack of anatomical localization of the endoscope within the lung. In this work, we proposed and validated the use of x-ray fluoroscopy-guidance in a rat model of RIPF to pinpoint the location of the endoscope during FE imaging and map it back to its anatomical location in the corresponding CT image. For varying endoscope positions, we observed a positive correlation between CT and FE imaging as reflected in the significant association between increased lung density on CT and the presence of fluorescent fiber structures with FE in RT cases compared to Control. Combining multimodality imaging allows visualization and quantification of molecular processes at specific locations within the injured lung. The proposed image-guided FE method can be extended to other disease models and is amenable to clinical translation for assessing and monitoring fibrotic damage.

6.3 Introduction

Radiation-induced pulmonary fibrosis (RIPF) is a common side effect of thoracic irradiations for lung and breast cancer treatments [3]. Radiation therapy (RT) aims to treat the tumor and spare surrounding healthy tissue. However, despite great progress in RT delivery, some normal tissue around the tumor will be exposed to irradiation. RT results in cell kill and loss of function of the affected region. It is then followed by a reversible inflammatory phase with accumulation of fluid and recruitment of inflammatory cells to the site of injury. In some cases, when the inflammatory phase is not regulated properly, it persists and there is accumulation of extra-cellular matrix and subsequent formation of scar tissue [5, 7]. This late phase which is thus far irreversible is called RIPF. Currently, limited treatment options are available for RIPF and mainly involve supplementary oxygen and steroids to reduce inflammation [23]. RIPF is

closely related to idiopathic pulmonary fibrosis and the methodology presented here could be applied to this disease and similar fibrotic diseases as well.

The exact underlying molecular mechanisms behind RIPF remain unknown and is an area of active research. Currently, to assess the extent of RIPF clinically, a chest x-ray (2-dimensional) or its 3D equivalent computed tomography (CT) scan is performed [15]. Both methods detect differences in tissue density as a basis of image contrast. As RIPF develops, the accumulation of extra-cellular matrix components (such as collagen) within the lung creates an increased lung density that can become visible with x-ray and CT imaging [80, 91].

A known landmark of fibrosis is collagen deposition and its accumulation relates to the extent of damage present in the tissue [84]. CT imaging is restricted to anatomical information and a complementary imaging technique capable of detecting RIPF at the subcellular and molecular levels would be of great interest to better understand how RIPF develops and could be used to monitor disease progression and therapeutic efficacy when testing new drugs.

Advanced molecular imaging techniques have the potential to help answer such open biologically relevant questions. In particular, fluorescence endomicroscopy (FE) is a new promising minimally invasive imaging technique, which consists of a confocal fluorescent microscope at the tip of an endoscope [18]. FE is able to image accessible organs such as the lung through bronchoscopy, and provide "optical biopsies" of disease regions *in vivo* and in real time. FE is already used clinically with autofluorescence or in combination with fluorescent probes for bronchoscopy to study the progression of different lung diseases [47]. However, it has not been applied in clinical RIPF assessment yet. Here, we present a fluorescent collagen probe in combination with FE imaging to enable visualization of RIPF at the cellular level *in vivo* in a rat model.

One of the major limitations of FE imaging for clinical and pre-clinical practice is the lack of ability to localize the endoscope inside the organ of interest at the time of imaging. If the region of the lung in which the FE images are taken can be macroscopically identified, they can be related to a specific location or a disease region of interest within the lung. Fluoroscopy-guidance is used regularly for image-guided radiotherapy, surgical procedures or bronchoscopy, providing 2D x-ray images of the subject in real time [92].

In this study, we present and evaluate macroscopic fluoroscopy-guidance to localize the tip of the endoscope during FE imaging in a rat model of RIPF. This allows to relate FE microscopic information at a certain specific location within the lung, to its corresponding macroscopic 3D CT image for disease assessment and monitoring.

6.4 Results

6.4.1 Fluorescent collagen probe validation for FE imaging

In order to visualize fibrosis at the microscopic level with FE imaging, a green fluorescent collagen probe was synthesized based on the design of a collagen binding MRI probe for fibrosis imaging [39]. Prior to *in vivo* imaging, we evaluated the collagen probe binding affinity *in vitro* using a plate binding assay, where the collagen probe is added to wells of a plate that were coated (experimental) or not (control) with collagen. The measured fluorescence intensity from each well is then proportional to the collagen probe binding (Figure 6.1a). An increase in fluorescence intensity in the presence of collagen coating and an increase in fluorescence with increasing collagen probe concentration was observed (Figure 6.1b). A significant discrepancy in fluorescence intensity between collagen coating and no collagen coating started at 1 μM and increased even more at 10 μM (Figure 6.1b, purple) ($p = 0.0022$).

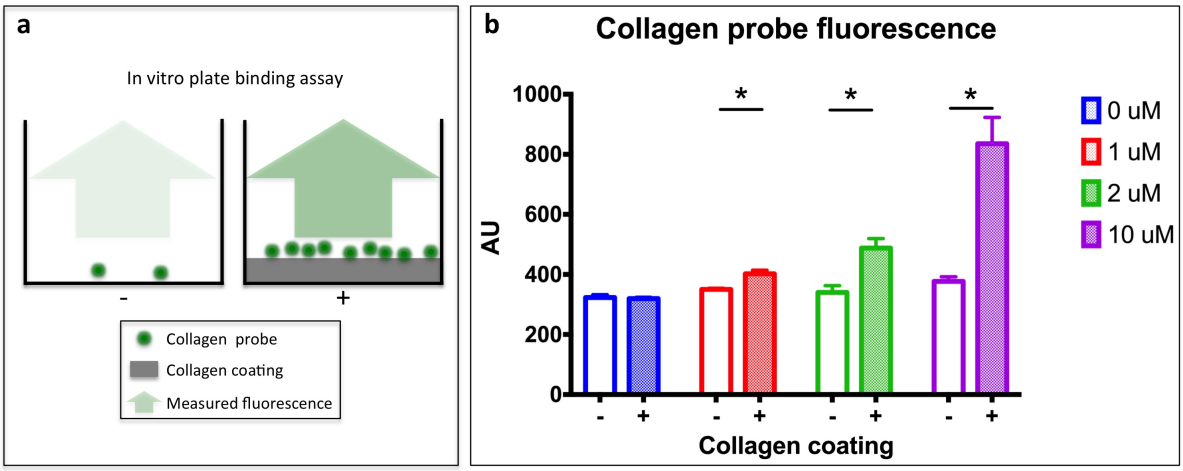

Figure 6.1 *In vitro* collagen plate binding assay. (a) Schematic of well plate without collagen coating (left) and with collagen coating (right). The collagen probe (green circles) binds to the collagen coating and the resulting fluorescence is measured (green arrows). (b) Fluorescence in arbitrary units (AU) at increasing collagen probe concentrations (from 0 μM to 10 μM) with or without collagen coating (+ or -).

Following *in vitro* validation, we tested the collagen probe *in vivo* in a bleomycin-induced lung fibrosis rat model imaged with FE. The probe injection was well tolerated and images showed an increased fluorescence in the fibrosis model compared to the control with the distinct presence of fluorescent fiber structures (data not shown).

6.4.2 CT, fluoroscopy and FE imaging experimental scheme

Sprague-Dawley rats (n = 16) were divided into two groups: Control (n = 8) or receiving radiation therapy (RT) (n = 8). The RT group were treated with 18 *Gy* to the right lung (hemithorax) in order to induce pulmonary fibrosis following our previous work [20]. All rats underwent a CT scan 24 weeks following irradiation. The next day, rats were injected with the fluorescent collagen probe and imaged with FE and fluoroscopy (coronal and sagittal views) at different endoscope locations. The experimental setup is described in Figure 6.2.

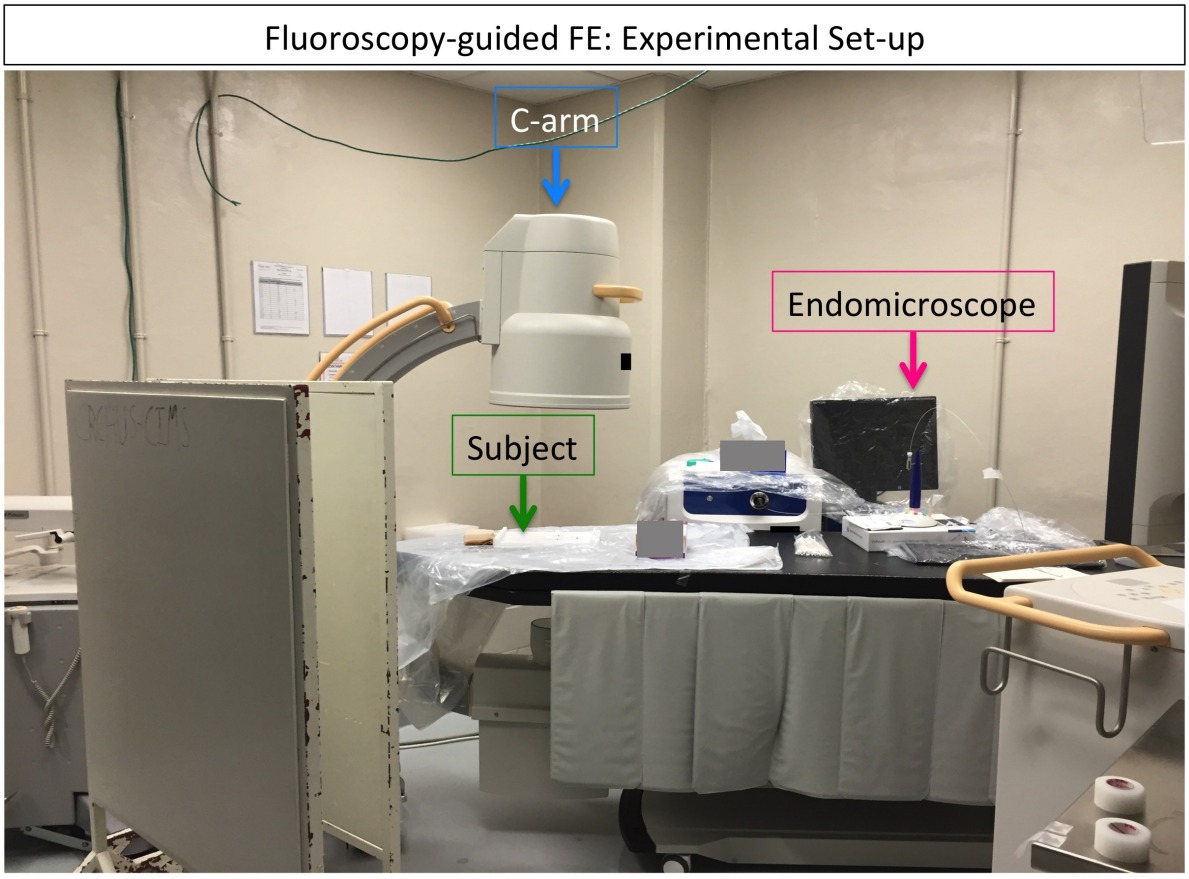

Figure 6.2 Experimental set-up. The rat is placed on the couch table (green arrow) in supine position. Then, the endoscope is inserted through a tracheotomy to a certain position in the lungs (pink arrow) and an FE video is acquired. With the endoscope in place an x-ray fluoroscopy image is acquired with the C-arm (blue arrow) in coronal view. Then, the C-arm is rotated by 90 degrees and a sagittal view image is acquired. The endoscope is moved to another location in the lung and the same process is repeated for every endoscope position.

6.4.3 FE images of collagen fibers

Previous pilot studies relying on autofluorescence imaging of RIPF showed the presence of faint autofluorescent fibers. In order to highlight those fiber structures a molecular fluorescent probe was used. FE images in combination with the fluorescent collagen probe showed the presence of fiber structures of increase fluorescence intensity as well as a noisy background of fluorescent dots. The relevant signal of interest became the detection of such fiber structures. Therefore, FE images were quantified by visual scoring for the presence (score of 1), faint appearance (score of 0.5) or absence (score of 0) of fibers for each endoscope location (Figure 6.3). Two independent observers scored FE video sequences for the presence of fluorescent fibers. The two observers' scores were in good agreement with a concordance correlation coefficient $(CCC) = 0.92$, 1 being perfect agreement. The FE fiber score used subsequently for FE image quantification is the average score of the two observers.

6.4.4 Image registration and endoscope localization

In order to localize the endoscope within the lung in 3D, a pair of 2D fluoroscopy images with the endoscope in place (coronal and sagittal view) were registered to the CT volume. Registration of each fluoroscopy image (2D) to the corresponding CT image (3D) was performed using a point-matching method [93]. Tags were placed on the same anatomical landmarks (vertebrae, ribs and sternum) on both fluoroscopy and CT images (Figure 6.4). Based on those matching points, an affine transform with 3 translations, 3 rotations and 1 scaling was computed.

Once the images were registered, using the pair of fluoroscopy images for each endoscope location, the location of the endoscope tip was pinpointed and the coordinates were mapped into the 3D CT volume (Figure 6.5a-c and d-e). The coordinates of the location of the endoscope obtained between the coronal and sagittal views matched well with an average standard deviation of 0.67 *mm*. Using this registration method, each FE image (Figure 6.5f) could be matched to each endoscope position on the CT (Figure 6.5a-c). It is therefore possible to compare each CT image at each location (macro-imaging) to the corresponding FE image (micro-imaging).

6.4.5 Comparison between Control and RT using CT and FE imaging

The extent of RIPF in control and irradiated rats was evaluated and quantified with both CT and FE imaging.

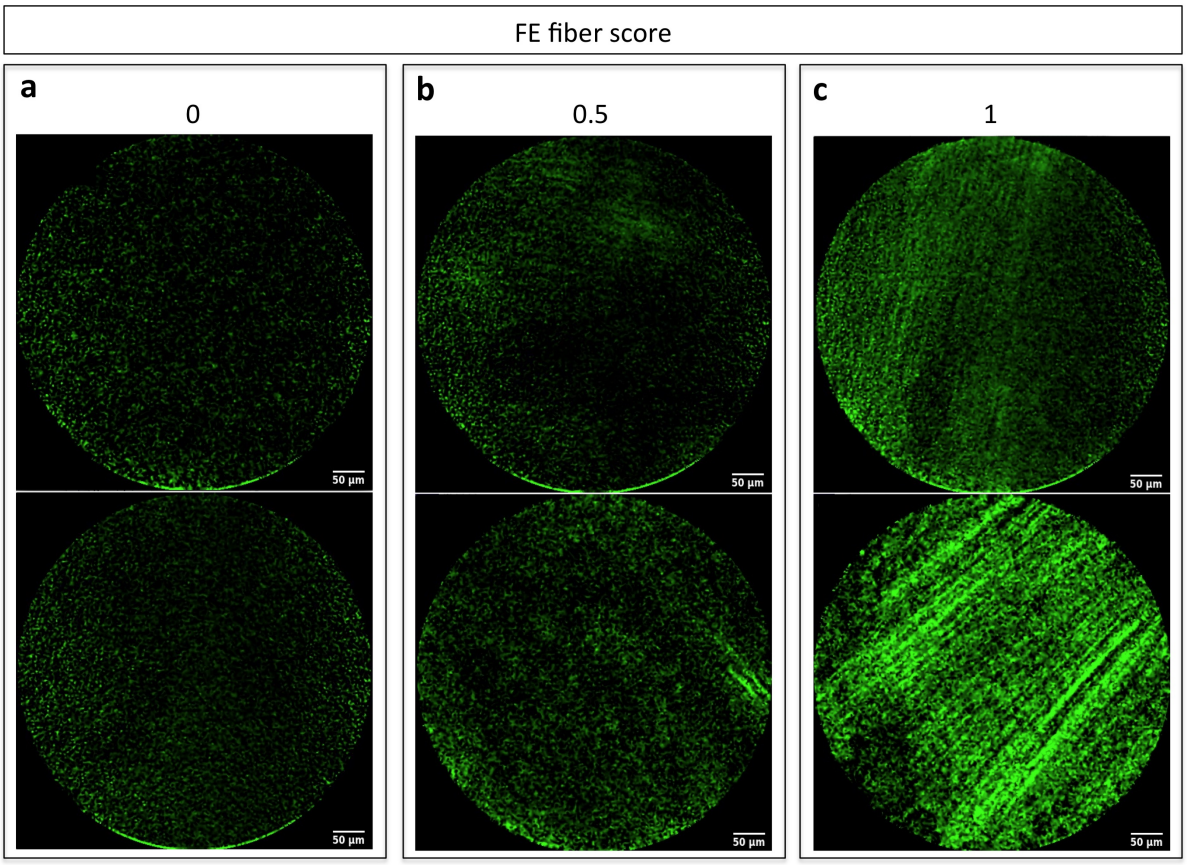

Figure 6.3 Representative FE images with collagen-targeted fluorescent probe showing fiber structures. FE video sequences were visually scored for the presence of fluorescent fibers from (a) 0: no fibers, (b) 0.5: faint appearance of fibers, to (c) 1: presence of fibers.

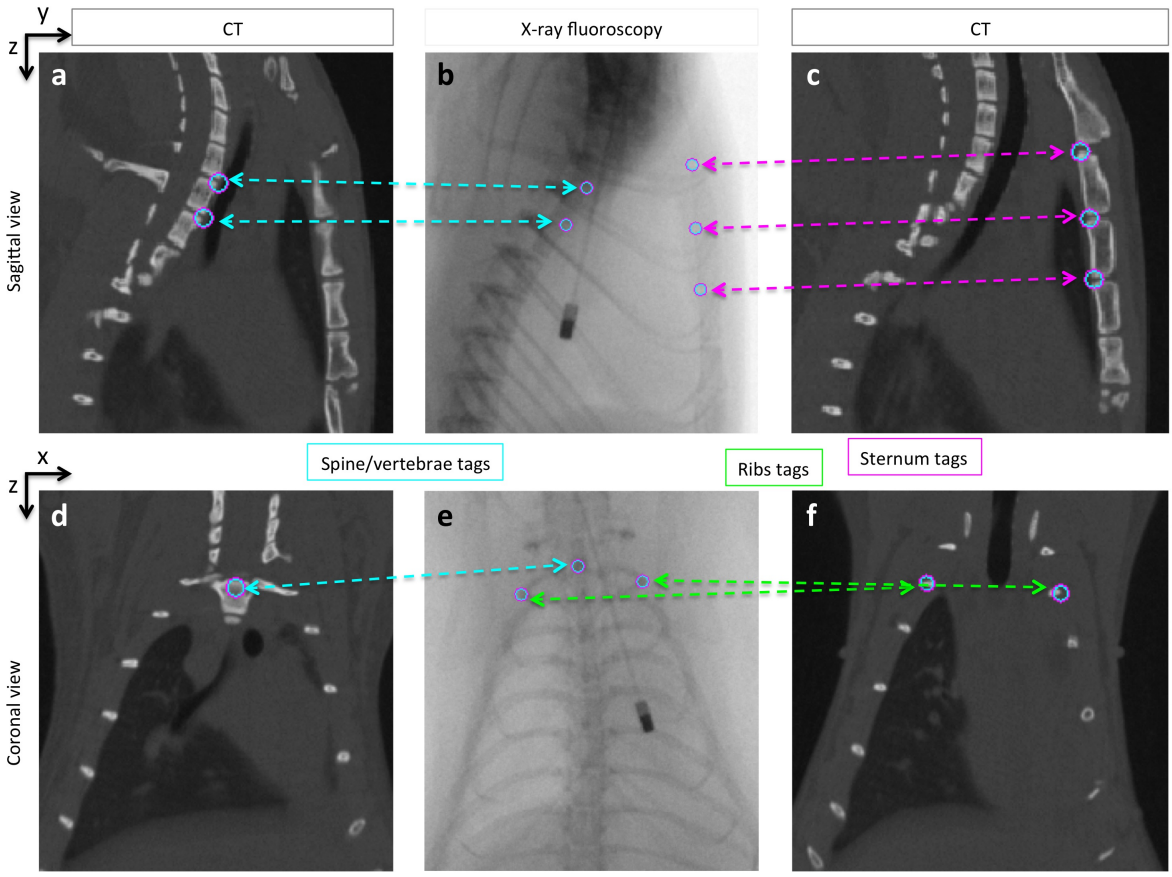

Figure 6.4 X-ray fluoroscopy to CT registration with point-matching method. Sagittal view (a,b and c) and coronal view (d, e and f) showing matching tags (circles) placed on anatomical landmarks appearing on both CT (a, c, d and f) and fluoroscopy (b and e). Tags are placed on visible structures such as the spine or vertebrae (cyan arrows), the ribs (green arrows) or the sternum (magenta arrows). The sagittal view provides the y and z coordinates and the coronal view provides the x and z coordinates.

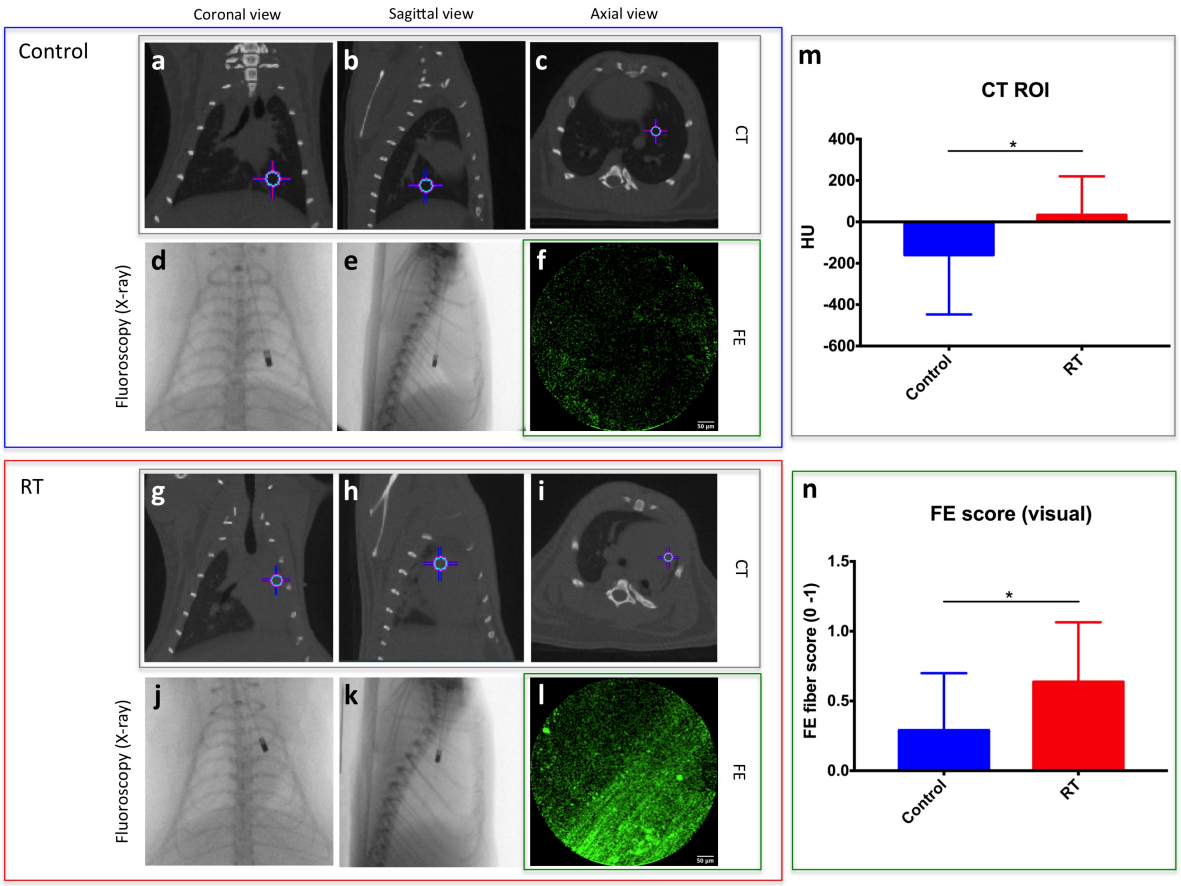

Figure 6.5 Representative CT (a-c and g-i, gray box) and FE (f and l, green box) images of control (a-f, blue box) and RT (g-l, red box) at the corresponding endoscope position determined with the fluoroscopy images (d-e and j-k, respectively). Crosshair indicates the position of the endoscope tip. (m) CT image quantification: The mean CT number (HU) for ROIs of each endoscope position for control (blue) and RT (red). (n) FE image quantification: Fiber score from 0 (no fiber) to 1 (fibers). for each endoscope position for control (blue) and RT (red).

CT macro-imaging shows an increased lung density due to RIPF in RT (Figure 6.5g-i) compared to control (Figure 6.5a-c). The right lung appears dark in the normal control lung (less dense, air-like) but is gray (denser, tissue-like) in RT. This increase in density on CT images was quantified by computing the mean CT value (in Hounsfield units [HU]) of a spherical region-of-interest (ROI) of 3 *mm* in diameter around each endoscope position (Figure 6.6a). Since the ROI is a small volume, the mean HU was used in this study. Figure 6.5m shows a significant increase in CT numbers (lung density) in RT compared to control with a median of 111.3 HU and -184.8 HU, respectively ($p = 0.0061$).

FE images with the fluorescent collagen probe show increase fluorescence intensity and the presence of fiber structures in RT (Figure 6.5l) compared to control (Figure 6.5f). Figure 6.5n shows that there are significantly more fibers present on FE images of RT cases compared to control with a median of 1 and 0, respectively ($p = 0.0025$).

6.4.6 Correlation between CT and FE imaging

Both CT and FE imaging were able to detect significant differences in lung fibrosis status between control and RT. To investigate this further, the correlation between CT and FE images at any given endoscope location was tested. Figure 6.6j shows significant correlation between CT values and FE scores for all the investigated endoscope locations yielding Spearman rank correlation $r = 0.3423$ ($p = 0.015$) and linear regression coefficient of determination $R^2 = 0.1114$.

However, some of the endoscope positions were considered to be more ambiguous and were classified into 3 categories: (1) proximal: trachea; (2) intermediate: heart; and (3) distal: diaphragm with examples shown in Figure 6.6 (b and f), (c and g) and (e and i), respectively. (1) When the endoscope is located close to the trachea in the proximal airways, CT values might not accurately match the location on the fluoroscopy since the endoscope passes through the intubation and tracheotomy for FE imaging. As indicated on Figure 6.6f the CT ROI at this location would comprise of a low density region (trachea) and a higher density region surrounding it, therefore giving a wide range of CT values. With respect to FE imaging in that proximal region, almost no fibers were observed (Figure 6.6j, magenta). (2) Some positions show that the endoscope appears to be located in the heart region on CT images (Figure 6.6g). Those events happened predominantly in the RT group (orange squares in Figure 6.6j), as the fibrotic right lung tends to collapse, which shifts the mediastinum towards it, resulting in increased lung density in that region, that blends in with the heart region (Figure 6.6g). (3)

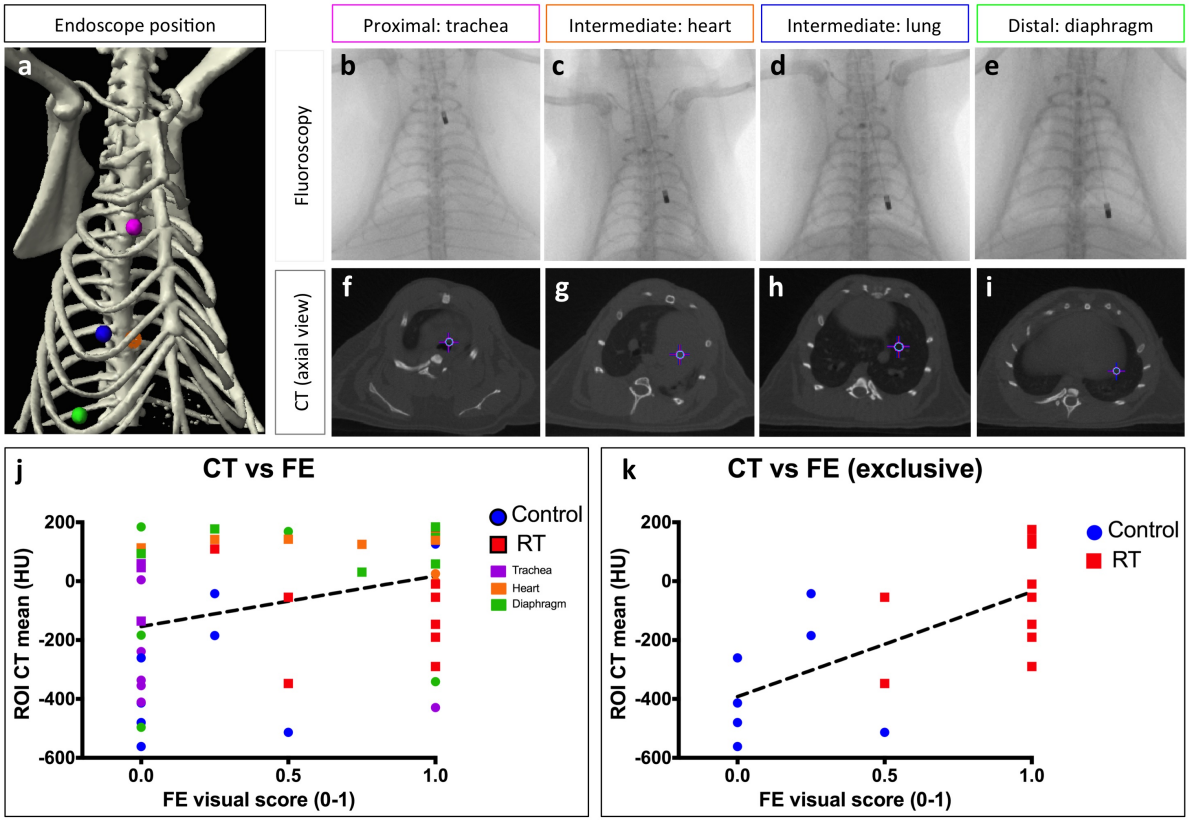

Figure 6.6 Correlation between CT and FE imaging at different endoscope positions. (a) 3D rendering of a rats' ribcage from CT image showing 4 endoscope locations indicated by color-coded spherical ROIs. Proximal: trachea location is indicated in magenta with the endoscope location on fluoroscopy and CT image (b and f) respectively; Intermediate: heart location in orange (c and g); Intermediate: normal lung location in blue (d and h); and Distal: diaphragm location in green (e and i). (j and k) Correlation between CT value and FE score for each corresponding endoscope location. (k) Correlation excluding trachea, heart or diaphragm locations (only lung locations). Control: blue circles and RT: red squares. Dashed black line indicates linear regression.

When the endoscope appears to be very distal and located in the diaphragm region (Figure 6.6i), the CT values extracted from those locations are higher as the CT ROI encompasses tissue more than lung (Figure 6.6j, green). Since the endoscope did not actually pierce the lung or touch the diaphragm, FE images show varying scores.

The correlation between CT and FE was also computed when excluding those ambiguous positions and keeping only the positions where the endoscope was located fully in the lung (Figure 6.6h). Figure 6.6k shows the exclusive highly significant correlation between CT and FE at restricted endoscope locations with improved Spearman $r = 0.643$ ($p = 0.0069$) and improved $R^2 = 0.4447$. Control (blue circles) exhibit both lower CT values and FE scores than RT (red squares).

6.4.7 Comparison of collagen probe and immunofluorescence on *ex vivo* lung tissue sections

In order to validate the collagen probe further, it was tested on *ex vivo* lung tissue sections and compared to immunofluorescence using a collagen targeted antibody.

Following *in vivo* imaging, lungs were harvested, frozen and sectioned for subsequent *ex vivo* microscopy analysis. Lung sections were stained with DAPI to highlight cell nuclei, with the collagen probe used previously *in vivo* and compared with immunofluorescence (antibody) of collagen (Figure 6.7).

While the Control exhibit normal regular alveolar structures (Figure 6.7d, white arrows), RT show a disrupted architecture with large empty regions and regions of dense fibrotic tissue (Figure 6.7h, white arrows).

Furthermore, collagen immunofluorescence show a significantly higher red fluorescence intensity (more collagen) in RT compared to Control (Figure 6.7g and c, respectively), quantified in Figure 6.7j ($p = 0.03$). However, this was not the case with the collagen probe (Figure 6.7b, f and i) ($p = 0.3823$).

While the collagen probe might be lacking in sensitivity compared to the collagen antibody immunofluorescence, it appears that both co-localize well in the same regions of the lungs (Figure 6.7f, g and h, yellow arrows) with an overall co-localization Pearson's coefficient $R = 0.35$. No significant co-localization difference was observed between Control and RT (Figure 6.7k) ($p = 0.2319$).

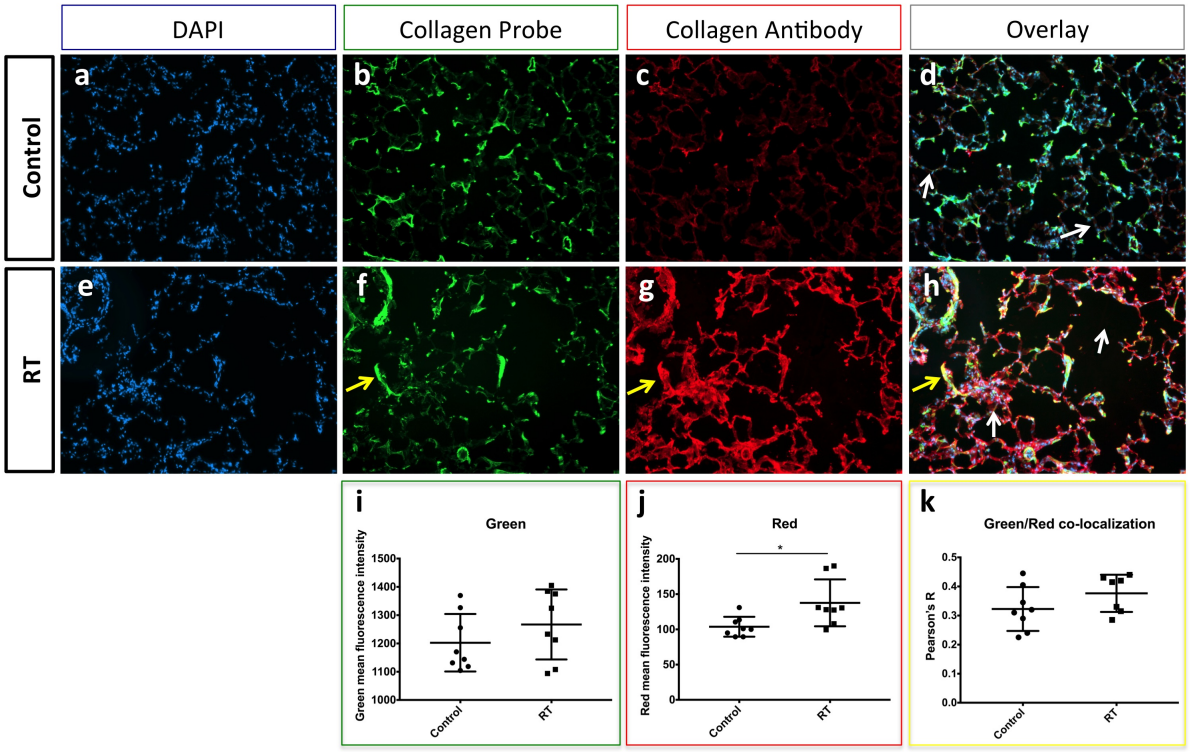

Figure 6.7 Microscopy images of DAPI (a and e, blue), collagen probe (b and f, green), immunofluorescence (c and g, red) and overlay (d and h) in *ex vivo* lung tissue sections comparing control (a-d) and RT (e-h). White arrows indicate normal alveolar structures in (d) and abnormal fibrotic regions with disturbed alveolar architecture in (h). (i and j) fluorescence intensity for the green or red channel, respectively, comparing Control (circles) and RT (squares). (k) Green and red co-localization Pearson's R for Control and RT. Yellow arrows indicates a region of green (f) and red (g) co-localization that appears in yellow in the overlay image (h).

6.5 Discussion

RIPF remains a major side effect of radiation therapy (RT) of lung and breast cancers. By combining prior CT imaging with fluoroscopy-guided fibrosis-targeted FE imaging, we were able to couple macro- to micro-imaging of RIPF in small animals. Thus, providing us with valuable location-specific information for clinical translation regarding the status of RIPF relating collagen fibrosis content to increased lung density.

We synthesized and validated a fluorescent collagen probe for FE imaging. It showed affinity to collagen and therefore fibrosis, both *in vitro* in a plate binding assay and *ex vivo* on lung tissue sections. The collagen probe did co-localize to the same regions as the antibody on *ex vivo* lung sections. However, the collagen probe was not as sensitive as the collagen binding antibody in immunofluorescence as it did not show a significant increase in fluorescence intensity in RT compared to Control. We were also able to observe fiber structures of increased fluorescence with *in vivo* FE imaging, that correlated with RIPF. We chose to use this fluorescent collagen probe for RIPF FE imaging, but other collagen or fibrosis specific probes could be used instead. We also investigated the possibility of using a commercially available collagen probe: Col-F [94]. However, our *in vivo* FE imaging attempt using Col-F did not show fluorescent fiber structures in injured lungs. In any case, newly developed probes have to be validated *in vitro* and *in vivo* before usage with FE imaging.

We visualized RIPF in a rat model with multimodal imaging requiring a micro-CT scanner, a C-arm and an endomicroscopy system. Performing fluoroscopy-guided FE imaging required that both the C-arm and the endomicroscopy system be in the same room with proper shielding for the x-rays and in close proximity to a surgery table to perform the required tracheotomy and probe injection. The CT scan could be acquired a day earlier and we were still able to position the rats in a similar manner to perform image registration between CT and fluoroscopy images. Access to all the equipment in the same location remains a challenge and requires prior planning and pilot studies to optimize the work-flow when imaging multiple subjects.

In this study, we used a manual point matching method with an affine transform to register CT and fluoroscopy images based on anatomical landmarks. We were able to obtain good agreement for endoscope localization with a standard deviation of 0.67 *mm* in the z-direction, keeping in mind that the diameter of the endoscope probe itself is 1.5 *mm*. This method could be streamlined using automatic nonlinear registration methods [95]. Using fiducial markers visible on both CT and fluoroscopy images would make automatic registration easier and faster. Even though relying on anatomical landmarks might also be a source of error in the registration, these

landmarks help quantify registration errors as they match directly with the specific anatomy of each individual rat.

Some endoscope positions were ambiguous as the endoscope tip appeared to be located in the trachea, the heart or the diaphragm. The endoscope remained in the airways but different factors might have influenced its location on CT images. Firstly, proximal locations appearing in the trachea were affected by the intubation and tracheotomy. Matching those locations back to the CT, where the rats were not intubated, could therefore be problematic as the anatomy of the proximal airways was disturbed. Secondly, the collapse of the irradiated lung, the shift of the mediastinum towards it and the increased lung density due to RIPF affected the CT contrast and the mapped location of the endoscope appearing to be located in the heart. Lastly, in some cases the endoscope was placed in a distal position and appearing to be located in the diaphragm when mapped onto the CT image. Again, the endoscope remained in the airways at all times and we did not observe piercing of the lung with the endoscope. However, respiratory motion of the diaphragm in distal regions of the lung is most probably the cause of these ambiguous locations. Image correlation between CT and FE was problematic at those endoscope locations and we obtained improved correlation when these were excluded from the analysis. Based on our experience in this study, we therefore recommend to keep the endoscope in intermediate locations to avoid the diaphragm by going too far or the trachea by remaining to close to the intubation.

We observed a correlation between lung density on CT images (macro-) and collagen fiber structures on FE images (micro-imaging) at any given corresponding endoscope location. The correlation improved when excluding ambiguous endoscope locations. Both imaging methods showed a significant increase in fibrosis in RT compared to Control. It is therefore possible to relate microscopic to macroscopic changes in lung tissue architecture.

In this study, we used fluoroscopy images to map the location of the endoscope back to the CT image. But, one could imagine going from an ROI on the CT, to placing the endoscope for FE imaging in that specific region with fluoroscopy guidance. This would require online and automatic image registration similar to image-guided surgery and would allow for live "optical biopsies" of targeted lung regions.

We developed and validated image-guided FE imaging for RIPF in small animals. This methodology can also be used for imaging other disease models such as idiopathic pulmonary fibrosis or any relevant model, provided one has a fluorescent probe for molecular imaging. One can then obtain both macro- and microscopic valuable information, providing a better understanding of the underlying molecular mechanisms of the disease *in vivo*.

6.6 Methods

6.6.1 Collagen probe and *in vitro* binding assay

The design of the collagen probe was based upon an MRI probe by Caravan *et. al.* [39] to image fibrosis *in vivo* in a mouse model [40]. The original MRI probe has a peptide structure identified by phage display with a demonstrated affinity for collagen. In order to use this probe design for fluorescence imaging, Gd-DTPA was replaced by fluorescein isothiocyanate (FITC) and since fluorescence is more sensitive than MRI, only one FITC molecule was incorporated. The collagen probe used in this study is as follows: Ac-Lys(Ac)-Trp-His-[*Cys-Thr-Thr-K(FITC)-Phe-Pro-His-His-Tyr-Cys]-Leu-Tyr-Bip-Amide.

We used an *in vitro* plate binding assay to test the affinity of the collagen probe to collagen (Figure 6.1a). The wells of a 96-well plate were coated with rat tail collagen (RatCol® Rat Tail Type I Collagen, Advanced BioMatrix, USA). Collagen was diluted to a concentration of 1000 $\mu g/ml$ in 0.1% acetic acid as described by the manufacturer and added to the wells (100 μl per well). Following an incubation of 1 hour at room temperature, the coated wells were washed with PBS. To avoid unspecific binding wells were blocked with 2% milk in PBS. The collagen probe was diluted in PBS to the desired concentrations (0, 1, 2 and 10 μM). Concentrations were verified by measuring the absorbance of the solution and calculating the concentration with optical density. The collagen probe was then added to the wells containing collagen or not (control) in 6 repeats wells and incubated for 30 minutes. The probe was then washed thoroughly with PBS. Following the binding assay, plate fluorescence was measured at 488 *nm* on a plate reader and the average fluorescence of 6 wells was computed for each concentration, with and without collagen coating.

6.6.2 RIPF rat model

All experiments were approved by the Animal Care Committee at the Research Institute of the McGill University Health Centre and in accordance with the ethical guidelines of the Canadian Council on Animal Care.

RIPF was induced in rats as previously described [20]. Briefly, Sprague-Dawley female rats were placed in a prone position and imaged on a computed tomography (CT) simulation scanner under isoflurane anesthesia (Philips Brilliance Big Bore, Philips Medical Systems, Bothell, WA, USA) using an optimized small animal protocol (120 kVp X-ray tube voltage, 175 mA tube current, 0.37 *mm* in-plane resolution, 0.4 *mm* axial resolution). A hemithorax parallel-opposed

3D conformal treatment plan was designed (EclipseTMV 11.0, Varian Medical Systems, Palo Alto, California, USA) for each animal based on pre-treatment CT image. Animal positioning was verified with cone-beam CT prior to irradiation. A single dose of 18 *Gy* was delivered to the right lung with a 6 *MV* photon beam on a clinical Truebeam linear accelerator (Varian Medical Systems, Palo Alto, California, USA). Subsequently, fibrosis developed in the right lung for 24 weeks.

6.6.3 CT imaging

Rats were imaged 24 weeks post-RT in supine position (on a Styrofoam holder for positioning reproducibility) under isoflurane anesthesia on a small animal CT scanner (X-RAD SmART, PXi, USA). Scanning protocol was optimized for rat lung imaging (100 *KVP*, X-Ray tube current: 1 *mA*, in-plane resolution: 0.2 *by* 0.2 *mm* and slice thickness: 0.2 *mm*).

6.6.4 Fluoroscopy-guided FE imaging

Rats were anesthetized with intramuscular injection of ketamine/xylazine. A tracheotomy was performed for FE imaging as previously described [20]. Briefly, in supine position a midline cervical skin incision was done, and the cervical trachea was exposed by vertical separation of the muscles. A small incision between the tracheal rings was performed to pass a 14G catheter through and allow the endoscope probe to pass.

The collagen probe was injected intravenously via canulation of the jugular vein at a concentration of 10 $\mu mol/kg$ in 1 *ml* of saline. 15 to 30 minutes following collagen probe injection, the rat was placed in supine position (as close as possible to the CT position on the Styrofoam holder) on the table of the C-arm. The tip of the endoscope was inserted in the lung through the tracheotomy tube and placed at a certain location (proximal, intermediate or distal). FE images were acquired with a small animal endomicroscopy system (Cellvizio Dual band Lab, Mauna Kea Technologies, France) in the green channel (488 *nm*) for 10 seconds videos (at 9 frames per second). Immediately after FE imaging, two fluoroscopy x-ray images were acquired with a C-arm (BV Pulsera, Philips Medical Systems, USA) in coronal (from the top) and sagittal view (rotated 90 degrees). Then, the endoscope probe was moved to another location in the lung, FE images were acquired and another pair of x-ray images were taken. This was repeated for 4 to 5 locations (endoscope positions) per animal (Figure 6.2).

6.6.5 CT/fluoroscopy image registration

In order to obtain the endoscope location in 3-dimensions, each pair of 2D fluoroscopy images (coronal and sagittal view) were registered to the 3D CT image of the corresponding rat using the MINC Register software (http://www.bic.mni.mcgill.ca) [93]. Tags were placed on anatomical landmarks visible on both CT and fluoroscopy images such as sternum, vertebrae or ribs (Figure 6.4). For sagittal view images, an average of 13 tags were used on the posterior region of each sternum bone junction (Figure 6.4b and c) and on the anterior region of vertebrae junctions (Figure 6.4a and b). Regarding coronal view images, tags were placed on the vertebrae at the point were ribs start to branch off (Figure 6.4d and e) and on the most external region of the ribcage for each rib as it curves back (Figure 6.4e and f). In most cases, 20 tags were used to register the coronal view images with points on each vertebrae and ribs, but in some cases, too many tags lead to big discrepancies in registration, therefore a limited number of tags (4 to 7) was used instead. This is most likely due to more uncertainty in tag placement on the ribs (with breathing motion), leading to mismatches between CT and fluoroscopy images. As the tags are placed and matched on both CT and fluoroscopy images, the corresponding transform was computed (3 translations, 3 rotations and 1 scaling) based on point-by-point matching of the tags.

The coronal view gave the x and z coordinates and the sagittal view gave the y and z coordinates (Figure 6.4). Both z coordinates were matched with an average standard deviation of 0.67 *mm*. The average between the two zs was used as the z-coordinate. Once the 2D fluoroscopy images were registered to the 3D CT image (by applying the transform), the location of the endoscope was identified on the fluoroscopy image and its coordinates (x, y, z) were mapped back to its corresponding location on the CT image.

Positions that ended up outside the CT image were excluded from subsequent analysis.

6.6.6 CT/FE image quantification at endoscope position

CT

Each endoscope position on the CT image was located and a spherical region of interest (ROI) with a 3 *mm* diameter was drawn (Eclipse V13, Varian Medical Systems, USA). Then, we computed the mean CT value in Hounsfield units (HU) for each ROI corresponding to each endoscope location.

FE

The fluorescent collagen probe highlights fibrosis, which appears as fiber structures on FE images. Each FE video was visually quantified for the presence (1), faint appearance (0.5) or absence (0) of fiber structures (Figure 6.3). Scoring was performed by two independent observers and the average score was used.

6.6.7 Collagen immunofluorescence and microscopy

Following FE imaging, rats were euthanized, the lungs were harvested and frozen in OCT. Lung tissue was then sectioned (10 μm thickness) on microscope slides for *ex vivo* evaluation. Slices were fixed in 4% formaldehyde for 15 minutes and washed in PBS three times. Blocking solution (10% goat serum, 0.3% Triton in PBS) was added to the slides for 1 hour and removed. Then, the primary antibody: rabbit anti-rat collagen type I (Cedarlane, Canada) was added (1:40 dilution in antibody dilution buffer: 5% goat serum, 0.3% Triton in PBS), incubated for 1 hour at 4 degrees and washed three times in PBS. The secondary antibody (dilution: 10 $\mu g/ml$): Alexa Fluor 647 goat anti-rabbit IgG (ThermoFisher, USA) was then incubated for 1 hour at room temperature and washed three times in PBS. Following the immunofluorescence procedure, the collagen probe (concentration: 10 μM) was added and incubated for 15 minutes then washed in PBS three times. DAPI (4',6-Diamidino-2-Phenylindole, Dihydrochloride ThermoFisher Scientific, USA) was added (dilution: 1:1000) and washed for nuclei staining. Lung slices were then mounted and sealed with a coverslip. Slides were allowed to curate over night.

Microscopy images were acquired on a fluorescence microscope (AxioVert A1, Zeiss, Germany) using 10X magnification with DAPI, GFP (collagen probe) and mPlum (collagen antibody) filters. Two images per slides were obtained and fluorescence intensity was computed for both the green and red channels. Co-localization for green and red was performed with the Zen software (Zeiss, Germany) and the Pearson's coefficient (r) was computed for each image.

6.6.8 Statistical analysis

Statistical analysis was carried out using GraphPad Prism software. Non-parametric Mann-Whitney test was used to compare two conditions (control vs RT) and Spearman rank correlation was used to correlate two imaging acquisition methods (CT and FE). Differences and correlations were deemed significant when $p < 0.05$ and indicated with a star (*) on graphs.

6.7 Acknowledgements

This work is partly supported by the Canadian Institutes of Health Research (CIHR) grants MOP-114910 and MOP-136774. Partial support to J.P. for this work came from the Natural Sciences and Engineering Research Council (NSERC) Medical Physics Research Training Network CREATE grant #432290. The authors would like to thank Dr. Louis Collins for assistance in image registration, Dr. Rejean Lebel for his contribution to the collagen probe validation and coordination of experiments with the C-arm and Dr. Marc-Andre Bonin for the collagen probe synthesis.

6.8 Author contributions statement

J.P., O.L., J.S and I.E.N. conceived the experiment(s), J.P., N.Y., F.C., M.S., G.P. and O.L. conducted the experiment(s), J.P. analysed the results. All authors reviewed the manuscript.

Chapter 7

Conclusion

7.1 Summary

About 50% of cancer patients will undergo radiation therapy (RT) for curative or palliative purposes at some point during the course of treatment. Radiation-induced lung injury (RILI) occurs in up to 30% of thoracic irradiations for lung or breast cancer and remains a major limiting factor to dose escalation and more efficient treatments. RILI can be divided into two phases: an early, inflammatory phase: radiation pneumonitis; and a late fibrotic phase: pulmonary fibrosis (RIPF), leading to symptoms of respiratory distress. The underlying molecular mechanisms of RILI development remain an area of active research and limited treatment options are available to mitigate this debilitating side effect.

Stem cell therapy has been proposed to help repair injured organs and has shown some promise in multiple organs including the lung. In particular mesenchymal stem cells (MSCs) have been shown to exhibit immunomodulatory properties, making them ideal candidates for potential RILI treatment. The use of stem cell therapy has been hindered by our lack of understanding regarding their behavior once administered in the body.

Medical and molecular imaging allow to visualize biological processes non-invasively and *in vivo* and are therefore valuable tools for the study of RILI and stem cell therapy. Computed tomography (CT) imaging gives anatomical images based on tissue densities and thus provides a good 3-dimensional view of RILI at every stage. Fluorescence endomicroscopy (FE) imaging is a new minimally invasive method placing a fluorescence microscope at the tip of an endoscope to probe and perform optical biopsies in accessible organs such as the lung. Coupled with

fluorescent probes to label the biological process of interest, FE imaging provides molecular level information in the study of RILI and stem cell therapy.

In this work, we first demonstrated the feasibility of tracking fluorescently labeled-MSCs in the lung with FE imaging in a rat model of RILI. This was coupled with the development of an automated cell counting algorithm to quantify the number of detected cells. We showed a significant increase in the number of detected MSCs when cells were injected directly in the trachea as opposed to intravenously. Moreover, we detected more MSCs in the RT group compared to control.

Next, following successful MSCs tracking, we used longitudinal CT imaging to monitor the evolution of RILI and assess MSCs' potential in mitigating it. CT results were compared to histopathology for fibrosis quantification 6 months post-RT. We observed a significant increase in fibrosis on both CT and histopathology for all RT groups compared to control with a minor improvement in RIPF when MSCs were administered intra-tracheally.

Finally, since CT imaging is restricted to anatomical macroscopic imaging, we developed a fibrosis targeted fluorescent probe coupled with FE imaging to detect RIPF at the molecular level *in vivo*. In order to relate microscopic FE images to their location in the lung, we used x-ray fluoroscopy guidance to detect the position of the endoscope at the time of imaging and mapped it back to the corresponding location on the CT image. We were able to detect RIPF on both CT and FE images for specific corresponding endoscope positions and we found a positive correlation between increased lung density on CT and the presence of fluorescent fibers on FE images in the RT group compared to controls.

In this thesis, we proposed, developed and validated a pre-clinical imaging platform to image and quantify the evolution of RILI and study MSCs behavior in a rat model of RILI.

7.2 Limitations of the current work

In the presented work, we used a rat model of RILI to develop our imaging tools. However, this model suffers from some limitations in terms of the translational potential of the methods. First of all, the obvious differences between a rat model and a human, including size, physiology and environmental factors, all of which play a big role in the actual clinical development of RILI. Second, RILI occurs in normal lung tissue surrounding the tumor volume, but, in our case, there was no tumor present in the lung, as the entire right lung (hemithorax) was irradiated. This might influence our results as the way RILI develops in the presence of tumor cells could vary and more importantly the tumor micro-environment could affect MSCs interactions and their

potential beneficial effects. Finally, RT is usually delivered in fractions, every day over a few weeks depending on the treatment scheme prescribed. In our RILI model, we delivered all the dose in one single fractions. This could have an impact on the radiobiological response of lung tissue and affect the onset of RILI. Nevertheless, we were able to recapitulate the onset of RILI with an acceptable time frame following current literature and observe RILI with our newly developed imaging tools and histology.

In chapter 4 and 6, we used a pre-clinical FE imaging system with an endoscope probe of diameter 1.5 mm, which required a tracheotomy to access the lung, making this method quite invasive and a terminal procedure. It limits our ability to use FE imaging longitudinally to monitor the same animals over time. Smaller endoscope probes that are compatible with the system, are available and should be considered for future longitudinal imaging. Although, it should be noted that they are more rigid, which might cause problems of tissue perforation. Other endoscope probes with varying optical properties would have to be tested and validated extensively prior to their use in such a big study.

Since FE imaging was implemented as a terminal procedure, we were only able to track MSCs the day of injection. This prevented us from potentially detecting cells during their homing process in the lung. Having a longitudinal FE imaging system would allow us to monitor MSCs fate over time. We were able to do so in a pilot study where the rats were kept alive with the tracheotomy tube in place. We detected labeled MSCs in the lung 7 days following injection. However, the rats were not in good health conditions and it was not possible to keep them in this situation for days. For ethical reasons, FE imaging remained a terminal procedure in the context of this work.

Another concern that arises in the context of longitudinal studies is the labeling of MSCs (chapter 4). We used a direct labeling method simply with a membrane dye, as a proof of principle that we could detect MSCs in the lung with FE. However, for longitudinal studies a more stable labeling, possibly involving a reporter gene system stably expressing a fluorescent protein, would be a better choice. It would allow to make sure the dye did not leak out of the cells and the fluorescence would be confined to cells that are alive and expressing it, therefore providing survivability of MSCs over time.

In chapter 5, we described a longitudinal study to monitor RILI onset with CT imaging. CT imaging being non-invasive, it was possible to image the rats every two weeks over a period of six months where we could visualize both inflammatory and fibrotic phases of RILI. This was compared to histopathology for the last time point. Histopathology remains the gold standard in assessing the extent of fibrosis, but it is limited to one location in the lung that cannot be related

to the CT image and it requires the animals to be sacrificed at that point making longitudinal studies impossible. In chapter 6, we proposed an FE imaging, providing optical biopsies, as a potential imaging method to bridge the gap between macroscopic, anatomical, 3-dimensional CT imaging and microscopic, 2-dimensional, fixed histopathology. Thanks to fluoroscopy guidance, we were able to relate FE images of collagen fibers to increased lung density on CT images at varying locations of the endoscope probe. Again, due to FE imaging being a terminal procedure, we were not able to monitor the development of RILI over time but only captured a snapshot at six months following RT.

In chapter 6, we quantified FE images by visual scoring of fluorescent fibers. We are currently investigating the possibility of developing an automated algorithm for fiber detection based on the Radon-like transform to quantify the frequency of fibers in an image. This would streamline the process making image quantification faster and more objective.

Another current limitation of image-guided FE imaging is that image registration was performed retrospectively after all images were already acquired. This limits our ability to do targeted FE images of a location of interest in the lung based on prior macroscopic information. We were still able to relate FE images to CT locations in RILI. However, a lot of endoscope positions were ambiguous as we were unable to place the tip of the endoscope to a specific location of interest. Ideally, image registration would be done in real time and we could target and place the endoscope probe where needed for FE imaging.

In this work, we did not combine MSCs therapy with collagen-targeted RIPF FE imaging (chapters 4 and 6). Two injections of MSCs (the day following RT and one week later) were performed in half of the control (n = 4) and RT (n = 4) groups of rats that underwent image-guided FE imaging (chapter 6). MSCs injections are very problematic to perform and put rats at risk. We did not pursue MSCs injections further but kept monitoring rats and we did not observe any differences between the rats that received MSCs and the ones that did not. It would be interesting to test if MSCs treatment could be visualized with collagen-targeted FE imaging. As per chapter 5, MSCs treatment, even when followed through for the scheduled 6 weeks post-RT, did not show a dramatic improvement of RIPF as their effect was minimal in all RT groups. Since MSCs effects on RIPF were not clear on the gold standard of histopathology, we can assume that the effect of MSCs were modest rather than CT or FE imaging not being sensitive enough to detect those changes. A positive control, i.e., a treatment with a definite known effect on RILI, would allow us to establish the sensitivity of our imaging methods in evaluating the extent of RIPF and the effect of MSCs therapy.

Due to a time frame discrepancy, MSCs treatment with FE tracking (chapter 4) was performed early in RILI development and RIPF FE imaging (chapter 6) was done in the later fibrotic phase. It was not possible to combine both methods in one imaging study because the two processes are in different time frames with MSCs imaging 3 weeks and RIPF imaging 6 months post-RT.

7.3 Clinical Prospects, Challenges and Future Research Directions

The molecular imaging tools developed here for RILI could be applied to other related pulmonary diseases such as idiopathic pulmonary fibrosis. Chemically induced fibrosis models (bleomycin injury) as opposed to RT-based damages exist and can be used in combination with MSCs therapy. This would expand the reach of the imaging methods to other diseases and therefore, provide more stable tools for quantification of different mitigation strategies.

In chapter 4, we demonstrated as a proof-of-principle that MSCs can be tracked with FE imaging in the lung. This imaging method can be expanded further as MSCs can be labeled with a variety of fluorescent dyes or more stably modified to express fluorescent reporter proteins. This would allow to track MSCs' viability since only live cells would be fluorescent. Therefore, it would provide key information to optimize stem cell injection timing and achieve constant immunomodulation via the presence of MSCs at the site of injury. Since the FE imaging system is equipped with two colors or channels (green and red), it is also possible to imagine more complex cell labeling methods triggering a color switch upon interaction with tissue or upon stem cell differentiation. This was investigate in the context of this PhD work to provide a molecular switch to detect stem cell differentiation. The cells would be modified to express green fluorescent protein in the stem cell state and switch based on a lung promoter to expressing red fluorescent protein upon cell differentiation. Since MSCs differentiation into lung functional cells was not established and still controversial, we did not have a stable system to benchmark and validate our probe construct on. Even so, *in vivo* differentiation being extremely rare, it would be close to impossible to capture it with FE imaging. This was not pursued further in this thesis work as we focused on imaging RILI itself and therefore the potential downstream effects of MSCs therapy on RILI rather than MSCs differentiation.

Other cell types such as cancer cells in other accessible organs such as the colon can also be tracked with FE imaging. As long as the cells are fluorescently labeled in the available channels and sufficiently bright, it will be possible to detect and quantify them with FE imaging.

As discussed in the limitations of this work, FE imaging was restricted to a terminal procedure. But with the use of smaller endoscope probe it would be possible to perform FE imaging repeatedly by using intubation rather than a tracheotomy. This would make FE imaging less invasive with longitudinal imaging potential. With a smaller endoscope probe, it would be possible to follow each animal over time with any type of fluorescent probe of interest. This would allow to monitor stem cells behavior and assess homing to the injury site. It would also be possible to monitor the onset of diseases over months.

One of the major limitations of using FE imaging is the fact that we cannot localize the endoscope and thus, we are unable to know from which location in the lung FE images came from. This was addressed in chapter 6 where we describe the use of image-guided FE imaging in order to localize the endoscope tip and combine the images acquired with FE with their location within the lung. This same methodology can be used in combination with stem cell tracking as described in chapter 4. Using image guidance would allow us to localize detected stem cells and gain information as to their homing capabilities. We would be able to determine where stem cells tend to localize and it would provide a useful understanding of their interaction with lung tissue. One could imagine cell labeling to work for both macroscopic imaging with a bioluminescence (BLI) or PET reporter system and a microscopic fluorescent label. It would therefore be possible to detect the cells with external imaging, register to anatomical imaging and then target FE imaging to locations of interest. It should be noted that in order to perform external cell tracking, a sufficient number of cells need to localize in the same place in order to produce a sufficient signal for detection. This was investigated for bioluminescence imaging in the context of this PhD research and was not pursued further because we were not able to detect MSCs externally in our rat model. It remains an interesting line of research to pursue for future studies on multimodality imaging.

Image-guided FE imaging was established to relate macroscopic images with FE microscopic images in chapter 6. However, image registration was performed after images were acquired, therefore making it impossible to truly target the acquisition of FE images at a specific lung location. Automating the registration process by making it real time would allow to visualize a target location on CT and direct the endoscope probe placement towards it for FE imaging. This process is not trivial and would require more research and development in order to achieve online real time image guidance similar to what is available in image-guided surgery.

Clinical translation is the ultimate of every pre-clinical imaging research development. Regarding stem cell therapy's clinical implementation, a lot of unanswered questions still remain to be addressed in order to provide safe and efficient treatment. It is crucial to gain more understanding and determine optimized therapy strategies in pre-clinical studies before bringing stem cell therapy to the clinic. Imaging tools like the ones developed in this work can help assess such biological questions in a pre-clinical setting and can also be adapted for clinical implementation by using a clinical FE imaging system for point-of-care medicine [96]. If stem cell therapy is tested on patients in the future, our proposed imaging methods to monitor the therapy would be incredibly useful tools to provide the needed information about safety and efficiency of treatment.

The imaging methods developed here are amenable to clinical translation as both CT and image-guided FE imaging in humans is already available clinically. The critical issues lie with the use of untested imaging fluorescent probes for use in humans, namely the cell labeling dye and the collagen targeted fluorescent probe. Non-specific FE contrast agents that are currently approved by the FDA such as Fluorescein are commonly used for topical or intravenous administration for the detection of abnormal epithelium for example. Targeted molecular probes like peptides or antibodies have recently been developed as well and tested mostly in animal models and on *ex vivo* human samples [97]. Imaging probes have to undergo rigorous testing in order to gain approval for use in clinical trials similarly to new drug development, where both safety and efficacy have to be proven.

7.4 Outlook

In conclusion, we believe that the development, validation and clinical implementation of new molecular imaging techniques like we initiated in this work, will provide a necessary platform to test and evaluate disease progression as well as monitor and assess the potential of newly proposed therapies such as promising stem cell therapeutic in mitigating radiation-induced lung injury and allow more aggressive targeting of cancer at reduced risks.

Bibliography

[1] Jacques Ferlay, Isabelle Soerjomataram, Rajesh Dikshit, Sultan Eser, Colin Mathers, Marise Rebelo, Donald Maxwell Parkin, David Forman, and Freddie Bray. Cancer incidence and mortality worldwide: sources, methods and major patterns in GLOBOCAN 2012. *International journal of cancer*, 136(5):E359–86, March 2015.

[2] Canadian Cancer Society. Canadian Cancer Society's Advisory Committee on Cancer Statistics. Canadian Cancer Statistics 2017. pages 1–142, June 2017.

[3] L B Marks, X Yu, Z Vujaskovic, and W Small. Radiation-induced lung injury. *Seminars in radiation oncology*, 13(3):333–345, 2003.

[4] I El Naqa, J Bradley, A I Blanco, P E Lindsay, M Vicic, A Hope, and J O Deasy. Multivariable modeling of radiotherapy outcomes, including dose–volume and clinical factors. *International Journal of Radiation Oncology* Biology* Physics*, 64(4):1275–1286, 2006.

[5] Feng-Ming Kong, Randall Ten Haken, Avraham Eisbruch, and Theodore S Lawrence. Non-Small Cell Lung Cancer Therapy-Related Pulmonary Toxicity: An Update on Radiation Pneumonitis and Fibrosis. *Seminars in oncology*, 32:42–54, April 2005.

[6] T D Crabtree, C E Denlinger, B F Meyers, I El Naqa, J Zoole, A S Krupnick, D Kreisel, G A Patterson, and J D Bradley. Stereotactic body radiation therapy versus surgical resection for stage I non–small cell lung cancer. *The Journal of Thoracic and Cardiovascular Surgery*, 140(2):377–386, 2010.

[7] S M Bentzen. Preventing or reducing late side effects of radiation therapy: radiobiology meets molecular pathology. *Nature Reviews Cancer*, 6(9):702–713, 2006.

[8] M O'Reilly and B Thebaud. Cell-Based Strategies to Reconstitute Lung Function in Infants with Severe Bronchopulmonary Dysplasia. *Clinics in Perinatology*, 39(3):703—-, September 2012.

[9] S C Abreu, M A Antunes, P Pelosi, M M Morales, and P R M Rocco. Mechanisms of cellular therapy in respiratory diseases. *Intensive Care Medicine*, 37(9):1421–1431, September 2011.

[10] V Sueblinvong and D J Weiss. Cell therapy approaches for lung diseases: current status. *Current Opinion in Pharmacology*, 9(3):268–273, June 2009.

[11] D.J. Prockop. Repair of tissues by adult stem/progenitor cells (MSCs): controversies, myths, and changing paradigms. *Molecular Therapy*, 17(6):939–946, 2009.

[12] D.G. Phinney and D.J. Prockop. Concise review: mesenchymal stem/multipotent stromal cells: the state of transdifferentiation and modes of tissue repair—current views. *Stem cells*, 25(11):2896–2902, 2007.

[13] Ola M Maria and Simon D Tran. Human Mesenchymal Stem Cells Cultured with Salivary Gland Biopsies Adopt an Epithelial Phenotype. *Stem Cells and Development*, 20(6), 2010.

[14] X. Yan, Y. Liu, Q. Han, M. Jia, L. Liao, M. Qi, and R.C. Zhao. Injured microenvironment directly guides the differentiation of engrafted Flk-1+ mesenchymal stem cell in lung. *Experimental hematology*, 35(9):1466–1475, 2007.

[15] Mike E Robbins, Judy K Brunso-Bechtold, Ann M Peiffer, Christina I Tsien, Janet E Bailey, and Lawrence B Marks. Imaging radiation-induced normal tissue injury. *Radiation research*, 177(4):449–466, April 2012.

[16] Michelle L James and Sanjiv S Gambhir. A molecular imaging primer: modalities, imaging agents, and applications. *Physiological reviews*, 92(2):897–965, April 2012.

[17] L Thiberville, M Salaün, S Lachkar, S Dominique, S Moreno-Swirc, C Vever-Bizet, and G Bourg-Heckly. Confocal fluorescence endomicroscopy of the human airways. In *Proceedings of the American Thoracic Society*, pages 444–449, 2009.

[18] G Paré, R Lebel, J Perez, F Chagnon, M A Bonin, C Bibeau, I El Naqa, E Marsault, Martin Lepage, and Olivier Lesur. Emerging applications of intra-vital smart micro-imaging: from bench-to- bedside . *Microscopy and imaging science: practical approaches to applied research and education*, February 2017.

[19] D Lewandowski and V Barroca. In vivo cellular imaging pinpoints the role of reactive oxygen species in the early steps of adult hematopoietic reconstitution. *Blood*, 115:443–452, 2010.

[20] Jessica R Perez, Norma Ybarra, Frederic Chagnon, Monica Serban, Sangkyu Lee, Jan Seuntjens, Olivier Lesur, and Issam El Naqa. Tracking of Mesenchymal Stem Cells with Fluorescence Endomicroscopy Imaging in Radiotherapy-Induced Lung Injury. *Scientific reports*, 7:40748, January 2017.

[21] Jessica R Perez, Sangkyu Lee, Norma Ybarra, Ola Maria, Monica Serban, Krishinima Jeyaseelan, Li Ming Wang, Jan Seuntjens, and Issam El Naqa. A comparative analysis of longitudinal computed tomography and histopathology for evaluating the potential of mesenchymal stem cells in mitigating radiation-induced pulmonary fibrosis. *Scientific reports*, 7(1):9056, August 2017.

[22] Giles Santyr, Matthew Fox, Kundan Thind, Elaine Hegarty, Alexei Ouriadov, Michael Jensen, Timothy J Scholl, Jacob Van Dyk, and Eugene Wong. Anatomical, functional and metabolic imaging of radiation-induced lung injury using hyperpolarized MRI. *NMR in biomedicine*, 27(12):1515–1524, August 2014.

[23] P.R. Graves, F. Siddiqui, M.S. Anscher, and B. Movsas. Radiation pulmonary toxicity: from mechanisms to management. *Seminars in radiation oncology*, 20(3):201–207, 2010.

[24] Sara Szabo, Swarajit N Ghosh, Brian L Fish, Sreedhar Bodiga, Rade Tomic, Gagan Kumar, Natalya V Morrow, John E Moulder, Elizabeth R Jacobs, and Meetha Medhora. Cellular inflammatory infiltrate in pneumonitis induced by a single moderate dose of thoracic x radiation in rats. *Radiation research*, 173(4):545–556, April 2010.

[25] Carl J Johnston, Jacqueline P Williams, Alison Elder, Eric Hernady, and Jacob N Finkelstein. Inflammatory cell recruitment following thoracic irradiation. *Experimental lung research*, 30(5):369–382, July 2004.

[26] C J A van Echteld and N Beckmann. A View on Imaging in Drug Research and Development for Respiratory Diseases. *Journal of Pharmacology and Experimental Therapeutics*, 337(2):335–349, April 2011.

[27] S Dharmarajan and D P Schuster. Molecular imaging of the lungs. *Academic Radiology*, 12(11):1394–1405, November 2005.

[28] Joanna E Kusmirek, Maria Daniela Martin, and Jeffrey P Kanne. Imaging of Idiopathic Pulmonary Fibrosis. *Radiologic clinics of North America*, 54(6):997–1014, November 2016.

[29] Patrick V Granton, Ludwig Dubois, Wouter van Elmpt, Stefan J van Hoof, Natasja G Lieuwes, Dirk De Ruysscher, and Frank Verhaegen. A longitudinal evaluation of partial lung irradiation in mice by using a dedicated image-guided small animal irradiator. *International Journal of Radiation Oncology* Biology* Physics*, 90(3):696–704, November 2014.

[30] Thida Win, Tryphon Lambrou, Brian F Hutton, Irfan Kayani, Nicholas J Screaton, Joanna C Porter, Toby M Maher, Raymondo Endozo, Robert I Shortman, Pauline Lukey, and Ashley M Groves. 18F-Fluorodeoxyglucose positron emission tomography pulmonary imaging in idiopathic pulmonary fibrosis is reproducible: implications for future clinical trials. *European journal of nuclear medicine and molecular imaging*, 39(3):521–528, March 2012.

[31] S S Kaushik, S H Robertson, M S Freeman, M. He, K T Kelly, Roos J E, Rackley C R, Foster W M, McAdams H P, and Driehuys B. Single-Breath Clinical Imaging of Hyperpolarized 129Xe in the Airspaces, Barrier, and Red Blood Cells Using an Interleaved 3D Radial 1-Point Dixon Acquisition. *Magnetic Resonance in Medicine*, (75):1434–1443, 2016.

[32] Rob H Ireland, Omar S Din, James A Swinscoe, Neil Woodhouse, Edwin J R van Beek, Jim M Wild, and Matthew Q Hatton. Detection of radiation-induced lung injury in non-small cell lung cancer patients using hyperpolarized helium-3 magnetic resonance imaging. *Radiotherapy and oncology : journal of the European Society for Therapeutic Radiology and Oncology*, 97(2):244–248, November 2010.

[33] Matthew S Fox, Alexei Ouriadov, Kundan Thind, Elaine Hegarty, Eugene Wong, Andrew Hope, and Giles E Santyr. Detection of radiation induced lung injury in rats using dynamic hyperpolarized 129Xe magnetic resonance spectroscopy. *Medical physics*, 41(7):072302, June 2014.

[34] Haidong Li, Zhiying Zhang, Xiuchao Zhao, Xianping Sun, Chaohui Ye, and Xin Zhou. Quantitative evaluation of radiation-induced lung injury with hyperpolarized xenon magnetic resonance. *Magnetic Resonance in Medicine*, 76(2):408–416, August 2016.

[35] Giles Santyr, Matthew Fox, Kundan Thind, Elaine Hegarty, Alexei Ouriadov, Michael Jensen, Timothy J Scholl, Jacob Van Dyk, and Eugene Wong. Quantification of regional early stage gas exchange changes using hyperpolarized 129Xe MRI in a rat model of radiation-induced lung injury. *NMR in biomedicine*, 27(12):1515–1524, April 2016.

[36] K Thind, A Chen, L Friesen-Waldner, A Ouriadov, T J Scholl, M Fox, E Wong, J VanDyk, A Hope, and G Santyr. Detection of radiation-induced lung injury using hyperpolarized (13)C magnetic resonance spectroscopy and imaging. *Magnetic Resonance in Medicine*, 70(3):601–609, September 2013.

[37] Kundan Thind, Michael D Jensen, Elaine Hegarty, Albert P Chen, Heeseung Lim, Francisco Martinez-Santiesteban, Jake Van Dyk, Eugene Wong, Timothy J Scholl, and Giles E Santyr. Mapping metabolic changes associated with early Radiation Induced Lung Injury post conformal radiotherapy using hyperpolarized ^{13}C-pyruvate Magnetic Resonance Spectroscopic Imaging. *Radiotherapy and oncology : journal of the European Society for Therapeutic Radiology and Oncology*, 110(2):317–322, February 2014.

[38] X-Y Hu, X-M Fang, H-W Chen, X-J Yao, P-Y Qian, J-Y Zhou, J Guo, A Lerner, and C-H Hu. Early detection of acute radiation-induced lung injury with multi-section CT perfusion imaging: An initial experience. *Clinical radiology*, 69(8):853–860, August 2014.

[39] Peter Caravan, Biplab Das, Stéphane Dumas, Frederick H Epstein, Patrick A Helm, Vincent Jacques, Steffi Koerner, Andrew Kolodziej, Luhua Shen, Wei-Chuan Sun, and Zhaoda Zhang. Collagen-targeted MRI contrast agent for molecular imaging of fibrosis. *Angewandte Chemie International Edition*, 46(43):8171–8173, 2007.

[40] Peter Caravan, Yan Yang, Roshini Zachariah, Anthony Schmitt, Mari Mino-Kenudson, Howard H Chen, David E Sosnovik, Guangping Dai, Bryan C Fuchs, and Michael Lanuti. Molecular magnetic resonance imaging of pulmonary fibrosis in mice. *American journal of respiratory cell and molecular biology*, 49(6):1120–1126, December 2013.

[41] Nawal Tassali, Andrea Bianchi, François Lux, Gérard Raffard, Stéphane Sanchez, Olivier Tillement, and Yannick Crémillieux. MR imaging, targeting and characterization of pulmonary fibrosis using intra-tracheal administration of gadolinium-based nanoparticles. *Contrast Media & Molecular Imaging*, 11(5):396–404, 2016.

[42] Julien Muzard, Laure Sarda-Mantel, Stéphane Loyau, Alain Meulemans, Liliane Louedec, Claudie Bantsimba-Malanda, Florence Hervatin, Joëlle Marchal-Somme, Jean Baptiste

Michel, Dominique Le Guludec, Philippe Billiald, and Martine Jandrot-Perrus. Non-invasive molecular imaging of fibrosis using a collagen-targeted peptidomimetic of the platelet collagen receptor glycoprotein VI. *PloS one*, 4(5):e5585, 2009.

[43] Alison E John, Jeni C Luckett, Amanda L Tatler, Ramla O Awais, Ami Desai, Anthony Habgood, Steve Ludbrook, Andy D Blanchard, Alan C Perkins, R Gisli Jenkins, and John F Marshall. Preclinical SPECT/CT imaging of $\alpha v\beta 6$ integrins for molecular stratification of idiopathic pulmonary fibrosis. *Journal of nuclear medicine : official publication, Society of Nuclear Medicine*, 54(12):2146–2152, December 2013.

[44] M Medhora, S Haworth, Y. Liu, J Narayanan, F Gao, M Zhao, S Audi, E R Jacobs, B L Fish, and A V Clough. Biomarkers for Radiation Pneumonitis Using Noninvasive Molecular Imaging. *Journal of Nuclear Medicine*, 57(8):1296–1301, August 2016.

[45] Nimali P Withana, Xiaowei Ma, Helen M McGuire, Martijn Verdoes, Wouter A van der Linden, Leslie O Ofori, Ruiping Zhang, Hao Li, Laura E Sanman, Ke Wei, Shaobo Yao, Peilin Wu, Fang Li, Hui Huang, Zuojun Xu, Paul J Wolters, Glenn D Rosen, Harold R Collard, Zhaohui Zhu, Zhen Cheng, and Matthew Bogyo. Non-invasive Imaging of Idiopathic Pulmonary Fibrosis Using Cathepsin Protease Probes. *Scientific reports*, 6:19755, January 2016.

[46] Frederic Chagnon, Clement Fournier, Paul G Charette, Luc Moleski, Marcel D Payet, Leland G Dobbs, and Olivier Lesur. In vivo intravital endoscopic confocal fluorescence microscopy of normal and acutely injured rat lungs. *Laboratory investigation; a journal of technical methods and pathology*, 90(6):824–834, June 2010.

[47] L Thiberville, M Salaün, S Lachkar, S Dominique, S Moreno-Swirc, C Vever-Bizet, and G Bourg-Heckly. Human in vivo fluorescence microimaging of the alveolar ducts and sacs during bronchoscopy. *The European respiratory journal*, 33(5):974–985, May 2009.

[48] Frederic Chagnon, Alexandra Bourgouin, Réjean Lebel, Marc-André Bonin, Eric Marsault, Martin Lepage, and Olivier Lesur. Smart imaging of acute lung injury: exploration of myeloperoxidase activity using in vivo endoscopic confocal fluorescence microscopy. *American Journal of Physiology-Lung Cellular and Molecular Physiology*, 309(6):L543–51, September 2015.

[49] Xiyi Chen, Oleg Nadiarynkh, Sergey Plotnikov, and Paul J Campagnola. Second harmonic generation microscopy for quantitative analysis of collagen fibrillar structure. *Nature Protocols*, 7(4):654–669, April 2012.

[50] Donald A Peyrot, Claire Lefort, Marie Steffenhagen, Tigran Mansuryan, Guillaume Ducourthial, Darine Abi-Haidar, Nicolas Sandeau, Christine Vever-Bizet, Sergei G Kruglik, Luc Thiberville, Frédéric Louradour, and Geneviève Bourg-Heckly. Development of a nonlinear fiber-optic spectrometer for human lung tissue exploration. *Biomedical optics express*, 3(5):840–853, May 2012.

[51] Jaime Mata, Ke Sheng, Klaus Hagspiel, Kai Ruppert, Peter Sylvester, John Mugler, Carolina Fernandes, Steven Guan, James Larner, and Paul Read. Pulmonary toxicity

in a rabbit model of stereotactic lung radiation therapy: efficacy of a radioprotector. *Experimental lung research*, 40(6):308–316, August 2014.

[52] R H Ireland, B A Tahir, J M Wild, C E Lee, and M Q Hatton. Functional Image-guided Radiotherapy Planning for Normal Lung Avoidance. *Clinical oncology (Royal College of Radiologists (Great Britain))*, 28(11):695–707, November 2016.

[53] Douglas A Hoover, Robert H Reid, Eugene Wong, Larry Stitt, Eric Sabondjian, George B Rodrigues, Jasbir K Jaswal, and Brian P Yaremko. SPECT-based functional lung imaging for the prediction of radiation pneumonitis: A clinical and dosimetric correlation. *Journal of Medical Imaging and Radiation Oncology*, 58(2):214–222, 2014.

[54] Tomoki Kimura, Yoshiko Doi, Takeo Nakashima, Nobuki Imano, Hideo Kawabata, Ikuno Nishibuchi, Tomoyuki Okabe, Masahiro Kenjo, Shuichi Ozawa, Yuji Murakami, and Yasushi Nagata. Combined Ventilation and Perfusion Imaging Correlates With the Dosimetric Parameters of Radiation Pneumonitis in Radiation Therapy Planning for Lung Cancer. *International Journal of Radiation Oncology* Biology* Physics*, 93(4):778–787, November 2015.

[55] A Tzouvelekis, A Antoniadis, and D Bouros. Stem cell therapy in pulmonary fibrosis. *Current Opinion in Pulmonary Medicine*, 17(5):368–373, September 2011.

[56] Patricia K Nguyen, Johannes Riegler, and Joseph C Wu. Stem cell imaging: from bench to bedside. *Cell Stem Cell*, 14(4):431–444, April 2014.

[57] M Modo. Noninvasive imaging of transplanted cells. *Current Opinion in Organ Transplantation*, 13(6):654–658, December 2008.

[58] M Rodriguez-Porcel, Joseph C Wu, and Sanjiv S Gambhir. Molecular imaging of stem cells. *StemBook*, 2009.

[59] Amit K Srivastava and Jeff W M Bulte. Seeing stem cells at work in vivo. *Stem cell reviews*, 10(1):127–144, February 2014.

[60] Inna Serganova, Vladimir Ponomarev, and Ronald Blasberg. Human reporter genes: potential use in clinical studies. *Nuclear medicine and biology*, 34(7):791–807, October 2007.

[61] U Himmelreich and T Dresselaers. Cell labeling and tracking for experimental models using Magnetic Resonance Imaging. *Methods*, 48(2):112–124, June 2009.

[62] Patricia E de Almeida, Juliaan R M van Rappard, and Joseph C Wu. In vivo bioluminescence for tracking cell fate and function. *American Journal of Physiology-Heart and Circulatory Physiology*, 301(3):H663–H671, September 2011.

[63] Molly E Kupfer and Brenda M Ogle. Advanced imaging approaches for regenerative medicine: Emerging technologies for monitoring stem cell fate in vitro and in vivo. *Biotechnology journal*, 10(10):1515–1528, October 2015.

[64] T. Schroeder. Imaging stem-cell-driven regeneration in mammals. *Nature*, 453, 2008.

[65] Samara Brown and Valentina Greco. Stem cells in the wild: understanding the World of stem cells through intravital imaging. *Cell Stem Cell*, 15(6):683–686, December 2014.

[66] Cristina Lo Celso, Charles P Lin, and David T Scadden. In vivo imaging of transplanted hematopoietic stem and progenitor cells in mouse calvarium bone marrow. *Nature Protocols*, 6(1):1–14, January 2011.

[67] Luke J Mortensen, Oren Levy, Joseph P Phillips, Tara Stratton, Brian Triana, Juan P Ruiz, Fangqi Gu, Jeffrey M Karp, and Charles P Lin. Quantification of Mesenchymal Stem Cell (MSC) Delivery to a Target Site Using In Vivo Confocal Microscopy. *PloS one*, 8(10):e78145, 2013.

[68] Dario Furlani, Murat Ugurlucan, LeeLee Ong, Karen Bieback, Erik Pittermann, Ingeborg Westien, Weiwei Wang, Can Yerebakan, Wenzhong Li, Ralf Gaebel, Ren-ke Li, Brigitte Vollmar, Gustav Steinhoff, and Nan Ma. Is the intravascular administration of mesenchymal stem cells safe? *Microvascular Research*, 77(3):370–376, May 2009.

[69] Ming Li, Yi-Xin Zhang, Zhen Zhang, Xiao-Yan Zhou, Xiu-Li Zuo, Yingzi Cong, and Yan-Qing Li. Endomicroscopy Will Track Injected Mesenchymal Stem Cells in Rat Colitis Models. *Inflammatory bowel diseases*, 21(9):2068–2077, September 2015.

[70] Cristina Mantovani, Giorgio Terenghi, and Susan G Shawcross. Isolation of adult stem cells and their differentiation to Schwann cells. *Methods Mol. Biol*, 916:47–57, 2012.

[71] T. Schroeder. Long-term single-cell imaging of mammalian stem cells. *Nature methods*, 8(4s):S30–S35, April 2011.

[72] Fränze Progatzky, Margaret J Dallman, and Cristina Lo Celso. From seeing to believing: labelling strategies for in vivo cell-tracking experiments. *Interface focus*, 3(3):20130001, June 2013.

[73] Mônica Cecília Bochetti Manna, Edna Frasson de Souza Montero, Jovelino Quintino De Souza Leão, and Neil Ferreira Novo. Microsurgical tracheotomy: a pediatric model in growing rats. *Microsurgery*, 23(5):530–534, 2003.

[74] Li-Hua Dong, Yi-Yao Jiang, Yong-Jun Liu, Shuang Cui, Cheng-Cheng Xia, Chao Qu, Xin Jiang, Ya-Qin Qu, Peng-Yu Chang, and Feng Liu. The anti-fibrotic effects of mesenchymal stem cells on irradiated lungs via stimulating endogenous secretion of HGF and PGE2. *Scientific reports*, 5:8713, March 2015.

[75] Manoj Reddy, Lyle Fonseca, Shashank Gowda, Basavraj Chougule, Aarya Hari, and Satish Totey. Human Adipose-derived Mesenchymal Stem Cells Attenuate Early Stage of Bleomycin Induced Pulmonary Fibrosis: Comparison with Pirfenidone. *International journal of stem cells*, 9(2):192–206, November 2016.

[76] B B Moore, M J Coffey, P Christensen, S Sitterding, R Ngan, C A Wilke, R McDonald, S M Phare, M Peters-Golden, R Paine, and G B Toews. GM-CSF regulates bleomycin-induced pulmonary fibrosis via a prostaglandin-dependent mechanism. *Journal of Immunology*, 165(7):4032–4039, October 2000.

[77] E El-Khatib, J Sharplin, and J Battista. The density of mouse lung in vivo following X irradiation. *International Journal of Radiation Oncology* Biology* Physics*, 9(6):853–858, June 1983.

[78] Christian Plathow, Minglun Li, Ping Gong, Heike Zieher, Fabian Kiessling, Peter Peschke, Hans-Ulrich Kauczor, Amir Abdollahi, and Peter E Huber. Computed Tomography Monitoring of Radiation-Induced Lung Fibrosis in Mice. *Investigative Radiology*, 39(10):600, October 2004.

[79] K Mah and J Van Dyk. Quantitative measurement of changes in human lung density following irradiation. *Radiotherapy and oncology : journal of the European Society for Therapeutic Radiology and Oncology*, 11(2):169–179, February 1988.

[80] J Van Dyk and R P Hill. Post-irradiation lung density changes measured by computerized tomography. *International Journal of Radiation Oncology* Biology* Physics*, 9(6):847–852, June 1983.

[81] Gabriela Stroian, Chandra Martens, Luis Souhami, D. Louis Collins, and Jan Seuntjens. Local correlation between monte-carlo dose and radiation-induced fibrosis in lung cancer patients. *International Journal of Radiation Oncology*Biology*Physics*, 70(3):921 – 930, 2008.

[82] S Lehnert and E El-Khatib. The use of CT densitometry in the assessment of radiation-induced damage to the rat lung: a comparison with other endpoints. *International Journal of Radiation Oncology* Biology* Physics*, 16(1):117–124, January 1989.

[83] Ralf-Harto Hübner, Wolfram Gitter, Nour Eddine El Mokhtari, Micaela Mathiak, Marcus Both, Hendrik Bolte, Sandra Freitag-Wolf, and Burkhard Bewig. Standardized quantification of pulmonary fibrosis in histological samples. *BioTechniques*, 44(4):507–11– 514–7, April 2008.

[84] Nevins W Todd, Irina G Luzina, and Sergei P Atamas. Molecular and cellular mechanisms of pulmonary fibrosis. *Fibrogenesis & tissue repair*, 5(1):11, July 2012.

[85] P Gao, Y Zhou, L Xian, C Li, T Xu, B Plunkett, S K Huang, M Wan, and X Cao. Functional Effects of TGF- 1 on Mesenchymal Stem Cell Mobilization in Cockroach Allergen-Induced Asthma. *The Journal of Immunology*, 192(10):4560–4570, May 2014.

[86] Shanti Gurung, Jerome A Werkmeister, and Caroline E Gargett. Inhibition of Transforming Growth Factor-β Receptor signaling promotes culture expansion of undifferentiated human Endometrial Mesenchymal Stem/stromal Cells. *Scientific reports*, 5:15042, October 2015.

[87] Andrea Augello, Roberta Tasso, Simone Maria Negrini, Andrea Amateis, Francesco Indiveri, Ranieri Cancedda, and Giuseppina Pennesi. Bone marrow mesenchymal progenitor cells inhibit lymphocyte proliferation by activation of the programmed death 1 pathway. *European journal of immunology*, 35(5):1482–1490, May 2005.

[88] Ola M Maria, Ahmed M Maria, Norma Ybarra, Krishinima Jeyaseelan, Sangkyu Lee, Jessica Perez, Mostafa Y Shalaby, Shirley Lehnert, Sergio Faria, Monica Serban, Jan Seuntjens, and Issam El Naqa. Mesenchymal Stem Cells Adopt Lung Cell Phenotype in Normal and Radiation-induced Lung Injury Conditions. *Applied immunohistochemistry & molecular morphology : AIMM*, 24(4):283–295, April 2016.

[89] Corrine R Kliment, Judson M Englert, Lauren P Crum, and Tim D Oury. A novel method for accurate collagen and biochemical assessment of pulmonary tissue utilizing one animal. *International journal of clinical and experimental pathology*, 4(4):349–355, April 2011.

[90] Yoshinori Sumita, Younan Liu, Saeed Khalili, Ola M Maria, Dengsheng Xia, Sharon Key, Ana P Cotrim, Eva Mezey, and Simon D Tran. Bone marrow-derived cells rescue salivary gland function in mice with head and neck irradiation. *The International Journal of Biochemistry & Cell Biology*, 43(1):80–87, January 2011.

[91] Gabriela Stroian, Chandra Martens, Luis Souhami, D Louis Collins, and Jan Seuntjens. Local correlation between monte-carlo dose and radiation-induced fibrosis in lung cancer patients. *International Journal of Radiation Oncology* Biology* Physics*, 70(3):921–930, March 2008.

[92] Yuichi Nagai and Yuzuru Kouno. The Role of X-Ray Fluoroscopy in Bronchoscopy. In *Respiratory Endoscopy*, pages 3–8. Springer Singapore, Singapore, November 2016.

[93] Wikibooks. Minc/visualtools/register — wikibooks, the free textbook project, 2011.

[94] Ewa Biela, Jerzy Galas, Brian Lee, Gary L Johnson, Zbigniew Darzynkiewicz, and Jurek W Dobrucki. Col-F, a fluorescent probe for ex vivo confocal imaging of collagen and elastin in animal tissues. *Cytometry. Part A : the journal of the International Society for Analytical Cytology*, 83(6):533–539, June 2013.

[95] P Markelj, D Tomaževič, B Likar, and F Pernuš. A review of 3D/2D registration methods for image-guided interventions. *Medical image analysis*, 16(3):642–661, April 2012.

[96] Jonathan T C Liu, Nathan O Loewke, Michael J Mandella, Richard M Levenson, James M Crawford, and Christopher H Contag. Point-of-care pathology with miniature microscopes. *Analytical cellular pathology (Amsterdam)*, 34(3):81–98, 2011.

[97] Joey M Jabbour, Meagan A Saldua, Joel N Bixler, and Kristen C Maitland. Confocal endomicroscopy: instrumentation and medical applications. *Annals of biomedical engineering*, 40(2):378–397, February 2012.

Appendix A

Fluorescence Endomicroscopy Imaging of Mesenchymal Stem Cells in the Rat Lung

Jessica R. Perez, Norma Ybarra, Frederic Chagnon, Olivier Lesur, Jan Seuntjens and Issam El Naqa

Invitation to submit this Protocol in: *Current Protocols in Stem Cell Biology*

A.1 Significance Statement

Despite its great promise, stem cell therapy remains an area of active research that is marred with controversy due to the lack of understanding of complex stem cell behavior and their fate once transplanted into the body. *In vivo* imaging has the potential to help answer key questions and contribute to bringing stem cell therapy a step closer to the clinic. In the context of lung damage repair with mesenchymal stem cells (MSCs) such as radiation-induced injury in cancer treatment, we developed a fluorescence endomicroscopy imaging method that allows us to track and quantify MSCs following their injection into a radiation-induced lung damage (RILD) rat model. This proof of principle provides a basis for future investigations into *in vivo* imaging for stem cell tracking and assessment, as it is a versatile technique that can be expanded to other relevant biological processes.

A.2 Abstract

Stem cell therapy has showed great promise for organ repair and regeneration. In the context of lung disease, such as radiation-induced lung damage (RILD) in cancer radiotherapy, mesenchymal stem cells (MSCs) have shown ability to reduce damage possibly due to their immunomodulatory properties and other unknown mechanisms. However, once MSCs are transplanted into the body, little is known as to their localization or their mechanisms of action. In this work, we proposed, implemented and validated a fluorescence endomicroscopy (FE) imaging technique that allows for the real-time detection and quantification of transplanted pre-labeled MSCs *in vivo* and tracking in a rat model. This protocol covers aspects related to MSCs extraction, labeling, FE imaging and image analysis developed on a RILD rat model but applicable to other biological systems.

A.3 Introduction

Mesenchymal Stem Cells (MSCs) have been proposed for their transplantation/immunomodulatory properties for the treatment of a variety of lung damage diseases, including inflammatory diseases and radiation-induced lung injury post-radiotherapy of cancer. Despite great promise, the exact mechanisms of action of stem cell therapy are still unknown and remain an area of active and controversial research [11]. Once MSCs are injected into the body, their location, viability or interactions with differentiated or progenitor lung cells is unknown. *in vivo* imaging has the potential to track injected MSCs, assess their efficacy and contribute to answering many currently open questions. Unlike whole body diagnostic imaging, fluorescence endomicroscopy (FE) allows the detection of individual cells at cellular resolution.

In this protocol description, we cover the technical aspects MSC-imaging *in vivo* in a RILD rat model with fluorescence endomicroscopy. This includes MSC extraction and culture, cell labeling with fluorescence membrane dye DiD, surgical procedures, imaging with FE and image analysis.

We demonstrate the proof of principle that one can image MSCs *in vivo* in the RILD rat model and monitor their fate. These protocols are meant to serve as a template to further our knowledge of stem cell behavior in lung damage and also applicable to other, related, biological systems. We used a simple membrane dye as labeling method but one can label cells with a reporter fluorescent protein and obtain more complex information. Since the endoscope is equipped with 2 fluorescence channels/colors (green and red), we can add another component

such as a structural probe (Figure A.1) or a disease-detecting probe in addition to the cell-labeling probe or even label two cell populations with different colors. One can also use other stem cell types or even cancer cells. There are many possibilities where this *in vivo* imaging method could be beneficial and help answer relevant biological questions of stem cell behavior.

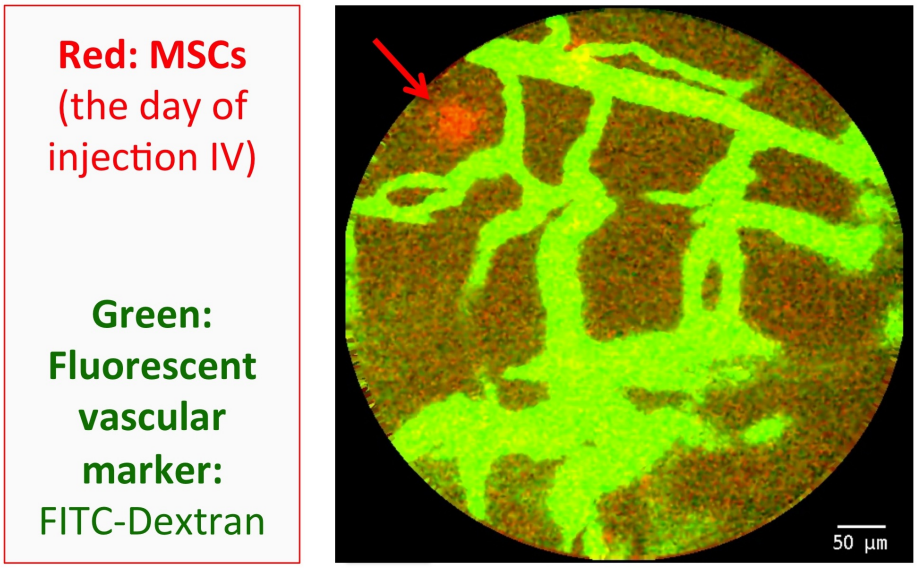

Figure A.1 **Labeled MSCs imaging coupled to vasculature imaging.** Since FE imaging allows two channel simultaneous imaging, in addition to DiD-MSCs (red), we also injected a fluorescent vascular marker (green) to highlight lung vasculature as an anatomical landmark.

A.4 Basic Protocol 1

A.4.1 MSCs extraction, culture and labeling

This protocol describes the steps involving the extraction of bone marrow-derived MSC from the rat and cell culture procedure. Once MSCs are in culture, we describe how to fluorescently label them for endomicroscopy imaging (illustrated in Figure A.2).

Materials

- Healthy Sprague Dawley rats (7-8 weeks old) 200-250 g (female)

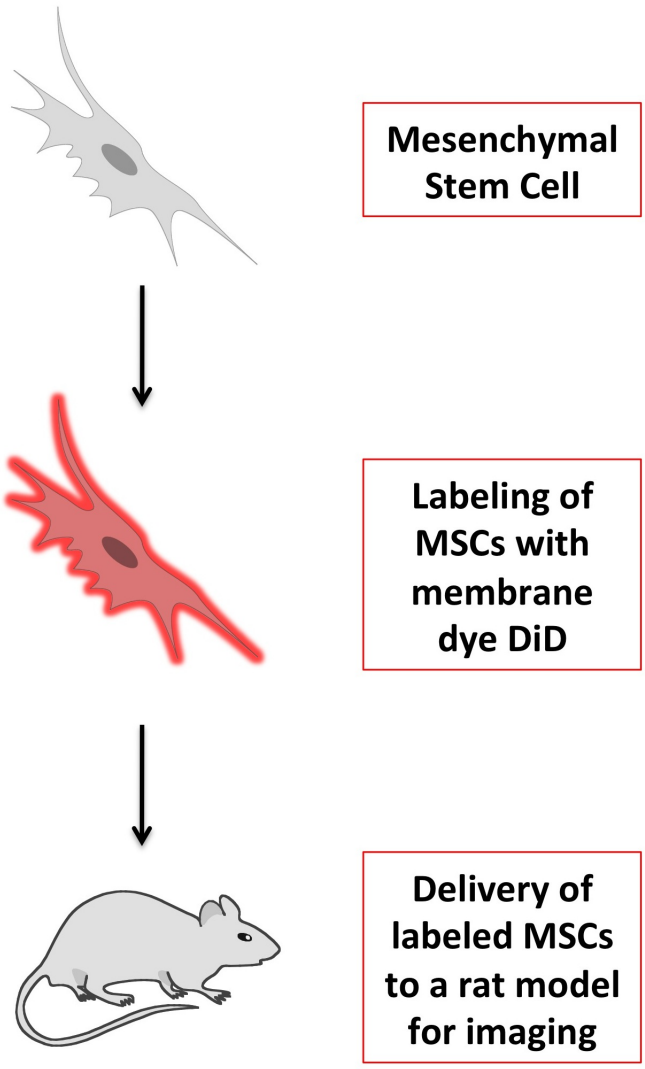

Figure A.2 **Illustration of MSCs labeling for imaging.** Once MSCs are in culture, DiD is added to the media to fluorescently label MSC. Following labeling, DiD-MSC are injected into the rat model for imaging.

Reagents and Solutions:

- DPBS (Thermo Fisher Scientific Cat. No. 14190144)
- Media for MSC MSCGM BulletKit (Lonza, distributed by Cedarlane, Cat. No. PT-3001 contains PT-3238 & PT-4105)
- Antibiotic & antimycotic (Thermo Fisher Scientific, Cat No. 15240-096)
- Trypsin-EDTA (0.25%) (Thermo Fisher Scientific, Cat No. 25200-056)
- Vybrant DiD Cell-labeling Solution (Thermo Fisher Scientific, Cat No. V22887)

Equipment:

- Sterilized surgical instruments: scissors, bone nibblers, forceps
- 50 ml sterile conical tubes
- Biosafety cabinet
- 10 ml syringes
- 21-gauge needles
- Cell strainer 70 μm Nylon (BD Falcon REF 352350)
- Centrifuge
- 10 ml serological pipettes
- T-75 flasks, canted neck, vented cap (Sarstedt Cat. No. 83.3911.302)
- Cell culture Incubator 5% CO2, temperature 37C

Protocol Steps

MSC extraction [70] and culture

1. Euthanize rat with CO2 asphyxiation under isoflurane anesthesia
2. Extract femoral bones by dislocating the hip and knee joint

3. Place intact femurs in DPBS in 50 ml sterile conical tube
4. Under biosafety cabinet for the following steps
5. Fill a 10 ml syringe with 21-gauge needle with 5 ml MSCGM media (MSCGM media is supplemented with antibiotic & antimycotic for all steps)
6. Cut the bone at both ends with the bone nibblers
7. Insert the needle at one end and flush the bone marrow and collect in a 50 ml tube on ice
8. Triturate the cell suspension twice by aspirating and flushing the mixture through the 21-gauge needle
9. Using a clean 50 ml tube, pass the cell suspension through a 70 μm Nylon cell strainer
10. Centrifuge cell suspension at 400 x g for 5 min
11. Discard the supernatant and resuspend the pellet with 8 ml MSCGM media
12. Prepare 4 T-75 flasks with 8 ml MSCGM media
13. Distribute the cell suspension: 2 ml in each of the 4 flasks to seed the cells
14. Place the cells in an incubator for 24 hours
15. The next day, aspirate media containing non-adherent cells
16. Wash with DPBS
17. Add 10 ml fresh MSCGM media
18. Over the next 2-3 days, monitor the cells. On the third day of culture adherent cells appear isolated when viewed under a phase-contrast microscope (Figure A.3, left). These cells are spindle-shaped and will form colonies (passage 0).
19. At about 80% confluence, subculture the cells. Remove MSCGM media, wash flask with 10 ml DPBS, and then add 5 ml of 0.25% Trypsin-EDTA, incubate at 37C for 5 min, after this add 5 ml of media (to neutralize trypsin), aspirate the cell suspension and place it into a 15 ml sterile conical tube, centrifuge at 400 x g for 5 minutes, re-suspend in fresh media, seed the cells in new flasks (passage 1)

20. Keep changing MSCGM media twice a week and passaging the cells as needed for expansion. (Do not exceed passage 4 for *in vivo* administration)

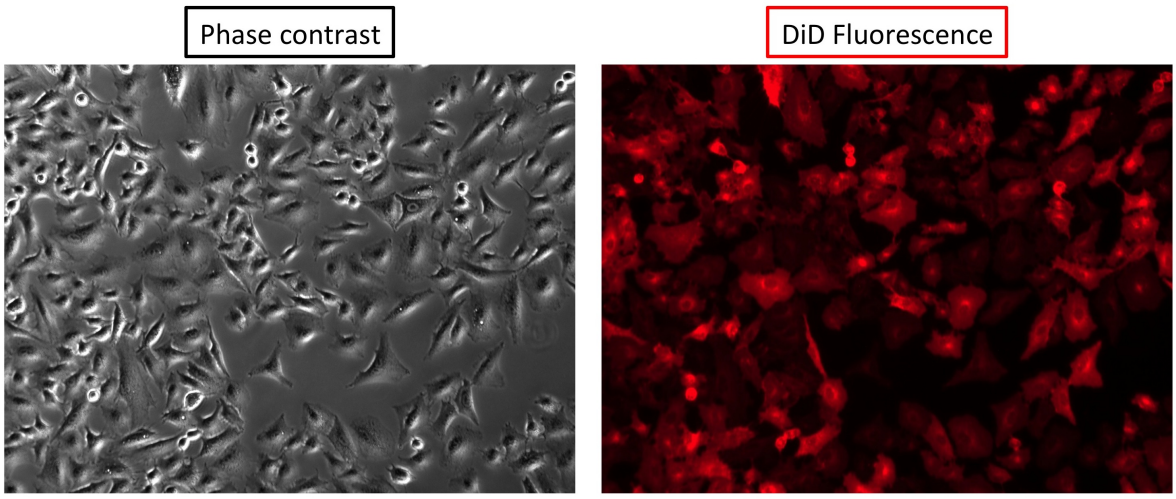

Figure A.3 **Microscope images of MSCs.** Left: spindle-shaped MSCs in culture (phase contrast), Right: Fluorescent DiD-labeled MSCs (10X magnification; fluorescence: mPlum filter)

MSC Labeling

1. Dilute DiD in 5 ml MSCGM media to a concentration of 10 μM in a 15 ml conical tube
2. Remove MSCGM media from flask and replace it with DiD MSCGM media
3. Incubate for 30 minutes at 37C.
4. Remove MSCGM media with DiD and wash with DPBS twice.
5. Add fresh MSCGM media
6. The next day, verify labeling with microscopy (Figure A.3, right) or fluorescence imaging (Figure A.4) (DiD excitation: 650 nm and emission: 670 nm)

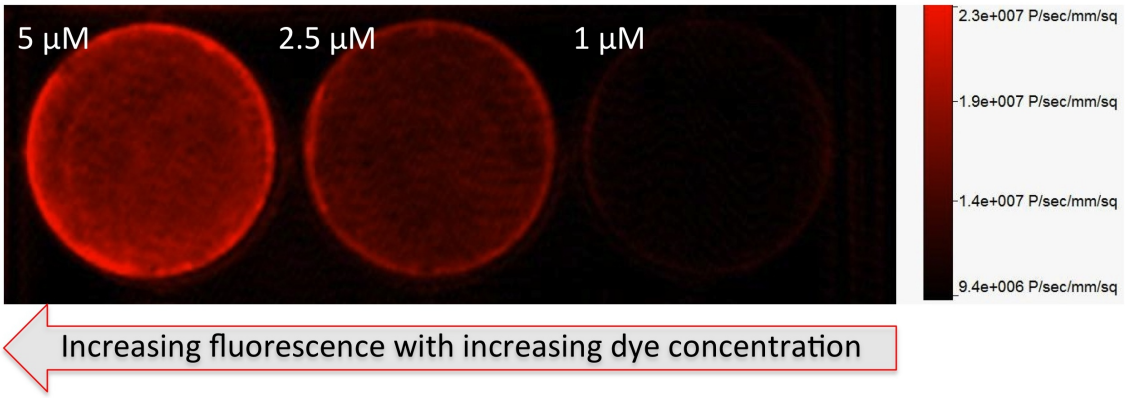

Figure A.4 **DiD labeling verification at varying dye concentrations.** MSCs were labeling in culture in a 6 well plate at different DiD concentrations; left: 5 μM, middle: 2.5 μM and right: 1 μM. Image was acquired on a small animal imaging system with fluorescence filters: excitation: 650 nm and emission: 670 nm. We observe an increased fluorescence signal with increasing dye concentration (arrow).

A.5 Basic Protocol 2

A.5.1 Surgical Procedures

This protocol describes the surgeries necessary for *in vivo* imaging of MSC with fluorescence endomicroscopy. It includes the surgical procedure for rat tracheotomy (required for endoscopy) and the jugular vein cannulation (required for intravenous injection of MSC). The tracheotomy procedure is required since the endoscope probe available measures 1.5 mm in diameter, which is too large to safely pass through the trachea and maintain air communication. One could potentially use a smaller endoscope probe and a simpler intubation procedure to avoid surgery. This would also allow for serial, longitudinal imaging capabilities. However, the protocol would have to be tested and validated with a different endoscope probe.

Materials

- Ketamine (e.g., Narketan 100 mg/ml; CDMV, cat. no. 440894)
- Xylazine (e.g., Xylamax 100 mg/ml; CDMV, cat. no. 3942)
- 1 ml syringes (Becton Dickenson, cat. no. 309659)

- 23G x 1 needles (Becton Dickenson, cat. no. 305145)
- Clipper (Braintree Scientific, cat. no. CLP-64 800)
- Scissors (e.g., Fine scissors - sharp; Fine Science Tools, cat. no. 14060-09)
- Forceps (e.g., Delicate suture tying forceps; Fine Science Tools, cat. no. 11063-07)
- 3-0 silk threads (e.g., Sofsilk size 3-0 black reel; Covidien, cat. no. LS639)
- 14 gauge Angiocath IV Catheter; 2.1 x 48 mm (Becton Dickenson, cat. no. 381167)
- Microscissors (e.g., Vannas spring scissors – 2 mm cutting edge; Fine Science Tools, cat. no. 15000-03)
- Intramedic polyethylene tubing PE50 (Becton Dickenson, cat. no. 427411)
- 0.9% saline (Baxter, cat. no. JF7634)

Protocol Steps

Rat tracheostomy [73]

1. Anesthetize the rat by a quadriceps intramuscular injection of ketamine (87 mg/kg) / xylazine (13 mg/kg).
2. Shave the ventral neck using a clipper.
3. Open the neck with a 1.5 cm ventral midline incision using scissors.
4. Expose the trachea using two forceps.
5. Pass a 10 cm silk thread under the trachea beneath the larynx.
6. Half cut the trachea just beneath the larynx using scissors.
7. Insert a 14-gauge Angiocath cannula into the trachea.
8. Fix the cannula with a ligature of the silk thread.

Rat jugular vein cannulation

1. Open the neck with a 2 cm ventral left incision above the pectoral muscle using scissors.
2. Isolate the jugular vein using two forceps.
3. Pass two 10 cm silk threads under the jugular vein at both extremities.
4. Ligate the thread near the head on the jugular vein.
5. Half cut the jugular vein between the two threads using microscissors.
6. Connect a 15 cm PE50 cannula to a 1 ml syringe with a 23G needle and filled with saline.
7. Insert 1 cm of the PE50 cannula into the jugular vein.
8. Verify Blood return by pulling the syringe piston connected to the cannula.
9. Fix the cannula with a ligature of the thread near the pectoral muscle.
10. Secure the cannula with a ligature of the thread near the head.

A.6 Basic Protocol 3

A.6.1 Fluorescence Endomicroscopy Imaging: MSC administration and endomicroscopy

This protocol describes the steps for *in vivo* imaging of MSC with fluorescence endomicroscopy. It includes the procedure for MSC preparation and injections as well as how to operate the endoscope.

Materials

- Trypsin-EDTA (0.25%) (Thermo Fisher Scientific, Cat No. 25200-056)
- Media for MSC MSCGM BulletKit (Lonza, distributed by Cedarlane, Cat. No. PT-3001 contains PT-3238 & PT-4105)
- DPBS (Thermo Fisher Scientific Cat. No. 14190144)

- Cell culture Incubator 5% CO2, temperature 37C
- Biosafety cabinet
- 50 ml sterile conical tubes
- 10 ml serological pipettes
- 1 ml syringe
- Centrifuge
- Cell counter (Countess Automated cell counter, Invitrogen Cat. No. C10227) + corresponding counting chamber slides + corresponding trypan blue
- Fluorescence endomicroscope Cellvizio Dual Band with S1500 confocal microprobe (Mauna Kea Technologies)
- Rat holder (can be homemade): inclined plane with elastic to keep the rat straight during imaging (Figure A.5)

Protocol Steps

1. Once cells are properly labeled in the flask, detach the cells using 5 ml of 0.25% trypsin-EDTA as previously described, incubated 5 min at 37 C
2. Neutralize trypsin cell suspension with 5 ml media in 50 ml tube
3. Centrifuge at 400 x g for 5 min
4. Aspirate the supernatant and re-suspend in sterile DPBS (The cell pellet appears blue due to DiD labeling)
5. Count cells: in a 1 ml tube, add 10 μl cell suspension to 10 μl trypan blue, use 10 μl to fill a counting chamber slide, insert slide in cell counter
6. Calculate and re-suspend cells in sterile DPBS or saline to the appropriate concentration:
   (a) For intravascular (IV) injection: 1 million cells in 500 μl
   (b) For intratracheal (IT) injection: 200,000 cells in 200 μl

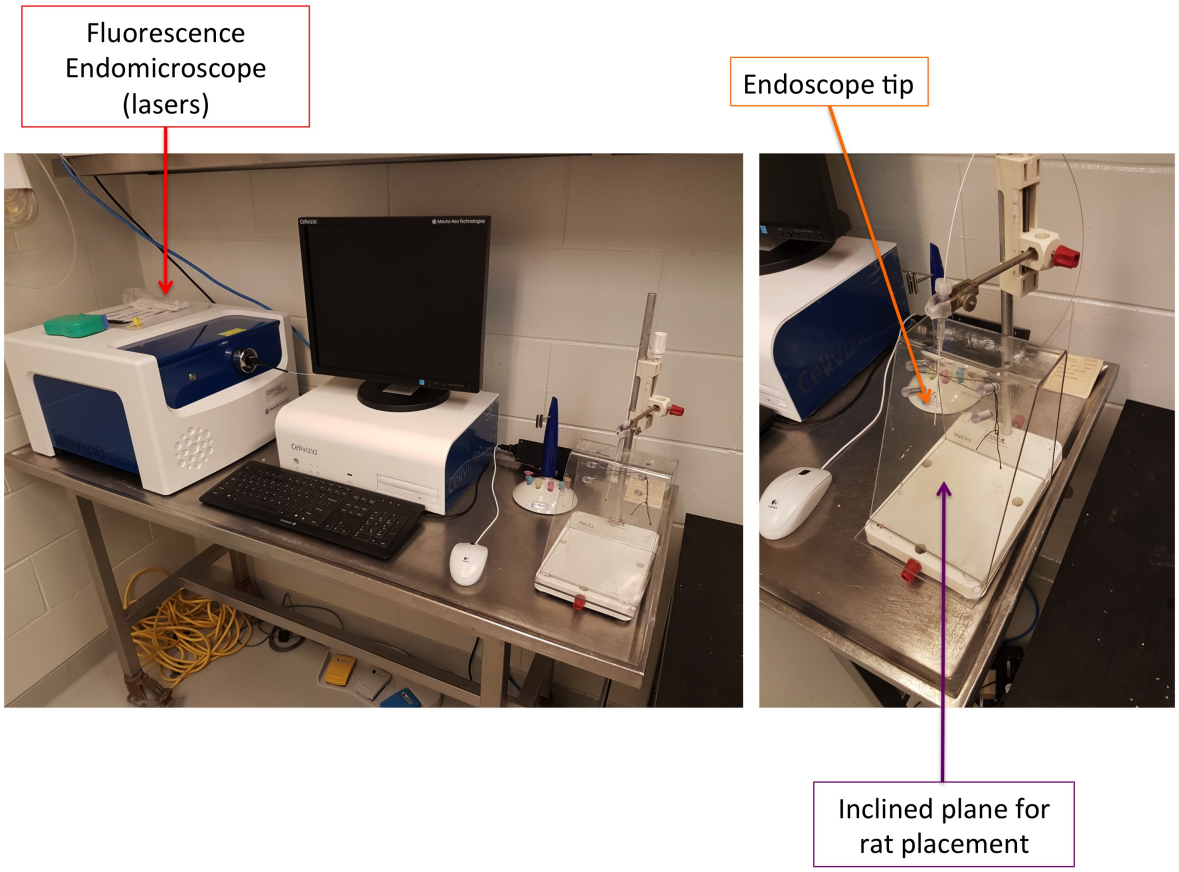

Figure A.5 **Set up of fluorescence endomicroscope.** Left: endoscope laser box (red arrow), right: inclined plane where the rat is placed for imaging (purple arrow). The rat hangs with the elastic holding it up through its front teeth. The tip of the endoscope (orange arrow) is then inserted in the tracheotomy and images are acquired.

7. Make sure the cells are well re-suspended to prepare the injection in a 1 ml syringe (no air bubbles)

8. Inject the cells:

   (a) For IV: through the cannulation of the jugular vein. Inject very slowly to avoid pulmonary embolisms

   (b) For IT: through the tracheotomy tube. IT delivery of MSC can temporarily impair normal breathing and rats could die.

9. Monitor rats to make sure the cell injection was successful and the animal is still breathing fine, ventilate if required.

10. Place the anesthetized rat with the tracheostomy tube in place on an inclined plane holder with an elastic holding the front teeth

11. After performing the endoscope's required calibrations, insert the tip of the endoscope in the tracheostomy (Figure A.5)

12. Acquire video sequences in the red channel (660 nm compatible with DiD fluorescence) as the endoscope moves within the lung

A.7 Support Protocol 1

A.7.1 Imaging analysis and quantification

This protocol describes the automated cell counting algorithm developed for fluorescence endomicroscopy imaging of MSC. A description of the algorithm can be found in Perez et al., 2017 [20] (Figure 2, Chapter...). Briefly, each video frame is treated as a stand-alone image. First, the contrast is enhanced. Then, we apply a granulometry algorithm followed by image opening. The image is then thresholded and objects (cells) are extracted. Each cell is counted using connected component analysis. This algorithm was optimized for our images but can be modified according to one's needs by adjusting the contrast/threshold or the roundness criteria of objects for example.

The Matlab code (SegCount.m called in CellCounting.m) can be found here:
https://github.com/JessicaRika/Automated-cell-counting-algorithm

A.8 Commentary

A.8.1 Background Information

Fluorescence endomicroscopy, also referred to as confocal laser endomicroscopy, is an intra-vital microscopy technique that allows real time *in vivo* imaging in a minimally invasive manner. It is the equivalent of a confocal fluorescence microscope at the tip of an endoscope. Principally, a scanning laser unit is coupled to a bundle of optical fibers that make up the endoscope tip and is in contact with the tissue sample to be imaged. The optical fibers relay the excitation light and collect the fluorescence from the sample to form an image. It can therefore provide images at cellular resolution in accessible organs such as the lung. FE can be used in conjunction with fluorescent probes to assess the state of disease or monitor biological processes [18].

in vivo FE imaging of transplanted stem cells has previously been demonstrated in mouse bone marrow [66] and MSC in a rat colitis model [69]. Our group demonstrated the use of FE imaging of transplanted MSC in a rat model of radiation-induced lung injury [20].

A.8.2 Critical Parameters & Troubleshooting

MSCs extraction is critical and extra care should be spent into making sure the MSCs do not get contaminated. Work with sterile instruments; disinfect the surfaces when doing the necropsy. Place the femur bone in a sterile tube as soon as it is extracted and open it only under the biosafety cabinet (class II for tissue culture).

Flushing the bone marrow might have to be repeated twice to make sure all bone marrow is expunged. It is possible that the needle moved or the bone broke at some point, so make sure to really flush as much as possible with an up and down needle motion.

It can happen that MSCs do not form spindles right away or do not form colonies in some flasks. The reasons are unknown but it is probably due to the fact that the cell density is sub-optimal for them to form colonies. It should not happen for every flask so discard the ones that do not seem to grow after the first week. If the problem persists, one might have to repeat the cell extraction.

We found that DiD labeling at a concentration of 10 μM was optimal in giving high fluorescence as well as maintaining a low cell toxicity. One might want to try varying DiD concentrations to achieve the desired result (Figure A.4). In our experience, DiD labeling is straightforward.

Regarding surgical procedures, they can be tricky to perform for a novice, so make sure to practice the procedures well in advance.

MSCs administration is key and can lead to death of the rat, if one is not careful. For intravenous injection, make sure the cells are re-suspended enough right before use, i.e., no pellet forming. The key is to inject very slowly (about 30 seconds) to make sure MSCs do not clot and cause pulmonary embolisms. Always monitor the animal and pause the injection if necessary. For endotracheal injection, the issue is drowning so make sure to re-suspend the cells in as little liquid as possible. Inject slowly to make sure the liquid gets absorbed progressively. It is possible that the rat will cough out some of the MSCs. Also monitor the animal and use thoracic massage and ventilation, if the rat stops breathing.

Concerning fluorescence endomicroscopy, the endoscope probe needs to be handled with caution, and it is important to monitor how deep in the lung one goes to avoid perforations and other complications. Make sure to acquire videos in a consistent manner across the animals to have comparable results.

A.8.3 Understanding Results

Labeling with DiD should lead to fluorescent MSCs. As showed in figure A.4 increasing DiD concentration increases the fluorescence of the cells.

On fluorescence endomicroscopy images, DiD-MSCs appear as bright spots (Figure A.6). It is apparent from the videos that there is significant motion due to breathing and heartbeat as well as the movement of the endoscope itself. DiD-MSCs are much brighter when injected directly into the trachea (Figure A.6, left). The number of detected cells can vary depending on the experimental condition. In our case, we observe a slight increase in the number of detected cells in a rat model of lung irradiation damage compared to controls [20].

A.8.4 Time Considerations

MSCs extraction takes about 2-3 hours and depends on the number of rats used. One should plan for a half day to obtain MSCs in culture. Media should be changed the following day to remove floating cells and select for the plastic adherent MSCs. Within the next week, MSCs should start forming colonies of spindle shaped cells. In order to have enough cells to inject *in vivo*, one should count backwards from the number of rats needed for imaging using an approximation of about 1 million cells per flask. This takes about 2-3 weeks. Do not exceed passage 4 for cell injections, as MSC get larger and might loose their properties. Cell labeling

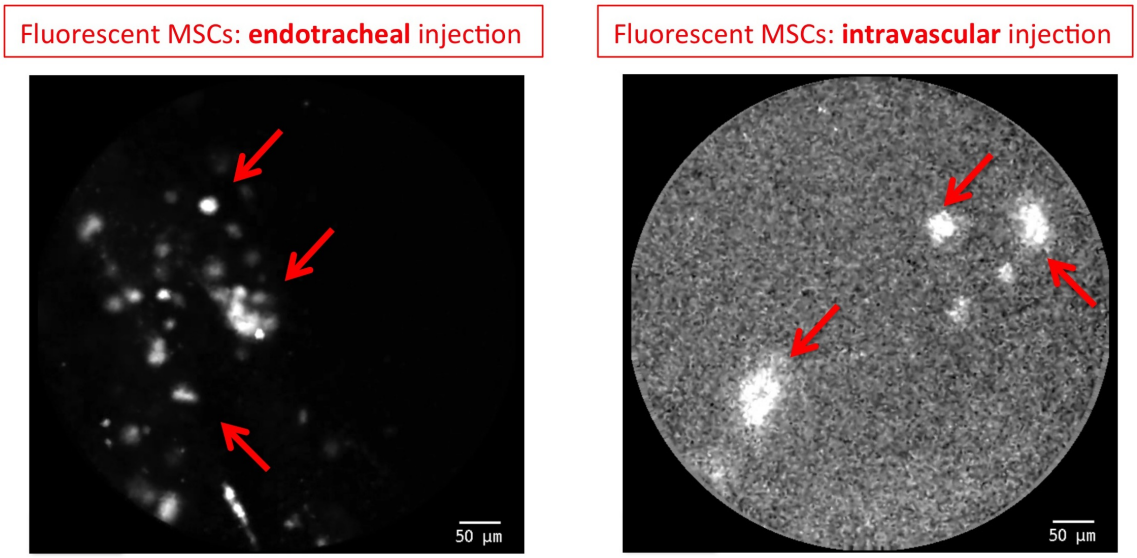

Figure A.6 **Fluorescence endomicroscopy imaged of DiD-MSCs *in vivo*.** Left: endotracheal MSCs injection, Right: intravascular MSCs injection. DiD-labeled MSCs appear as bright spots on the image (red arrows) and appear brighter when injected endotracheally compared to intravenously.

with DiD is straightforward and should take about 1 hour. It is then possible to verify proper labeling the next day and use the cells for injection.

With experience, surgical procedures (tracheostomy and jugular vein cannulation) take about 30 minutes per rat. Wait 5-15 minutes following MSC injection to start imaging. FE imaging takes a few minutes, in our case we acquired two 1 minute long video for each rat and explored different regions of the lung.

Image analysis and quantification depend on what is required. If using the automated cell counting algorithm provided with the protocol, one should count about 2 minutes per video to have an accurate cell count.

A.9 Acknowledgement

This work is partly supported by the Canadian Institutes of Health Research (CIHR) grants MOP-114910, MOP-136774 and FND-333254. Partial support to J.P. for this work came from the Natural Sciences and Engineering Research Council (NSERC) Medical Physics Research Training Network CREATE grant 432290.

A.10 Key Reference

Article published by our group, which prompted the writing of this protocol:
Perez, J. R., Ybarra, N., Chagnon, F., Serban, M., Lee, S., Seuntjens, J., Olivier Lesur & Issam El Naqa (2017). Tracking of Mesenchymal Stem Cells with Fluorescence Endomicroscopy Imaging in Radiotherapy-Induced Lung Injury. Scientific Reports, 7, 40748. [20]